Deciphering neuronal circuits of non-image forming vision

Inauguraldissertation
zur
Erlangung der Würde eines Doktors der Philosophie
vorgelegt der
Philosophisch-Naturwissenschaftlichen Fakultät
der Universität Basel
von

Kamill Imre Balint

aus **Ungarn**

Basel, 2018

Genehmigt von der Philosophisch-Naturwissenschaftlichen Fakultät
auf Antrag von

Prof. Dr. Silvia Arber

Prof. Dr. Botond Roska

Prof. Dr. Karl-Claus Conzelmann

Basel, 13.10.2015.

_____

Prof. Dr. Jörg Schibler
Dekan

Table of Contents

Introduction

The human brain consists of around 86 billion neurons which cooperate in millions of neuronal circuits through synaptic connections in order to perform the immense variety of brain functions (*1*). To fully understand the brain and its diseases we have to understand how neuronal circuits are built, and how they operate. The different functional circuits, assembled from different cell types, are often intermingled and, due to the lack of proper deciphering tools, their study was strongly limited in the past (*2*). In the last decade developments in trans-synaptic viral tracing, combined with modern imaging techniques, have enabled cell-type specific studies of neuronal circuits (*3*, *4*). In my thesis I present multiple projects addressing the development of trans-synaptic viral tools and their application in the study of neuronal circuits involved in subconscious vision.

Trans-synaptic viral tracing

Mapping connectivity in the nervous system was first achieved using neuroanatomical tracers such as horseradish peroxidase (*5*), Fluoro-Gold (*6*), cholera toxin b subunit (*7*), leucoagglutinin (*8*), wheat germ agglutinin (*7*), dextrans (*9*), latex beads (*10*). The common behavior of these agents is that they are taken up by the neurons and transported along the neurits in a retrograde (axon terminal to cell body) or anterograde (cell body to axon terminal) manner. Visualization of the tracers with the help of their enzymatic activity, immunohistochemistry or dye coupling, allows the identification of connected brain regions (macro-circuits). With these techniques, most of the macro-circuits were mapped in the last century. However, it was not possible to discriminate between parallel but functionally different channels between brain regions, or the micro-circuits within one region, using these techniques.

Neurotropic viruses such as alpha herpes viruses and rabies virus can infect neurons and spread to the connected cells through the synaptic cleft(*3*). Therefore, these viruses could be used for detecting the chains of neurons. However, their employment was limited by a number of

factors. Wild-type herpes simplex virus (HSV) and pseudorabies virus (PRV) both spread in anterograde and retrograde directions, which makes it difficult to discriminate between presynaptic and postsynaptic partners of the starter neurons. Furthermore, rapid development of symptoms, early death of the inoculated experimental animals, and the cytotoxic effect on the infected neurons reduced the scope of both anatomical and functional studies. In contrast, wild-type rabies virus (RV) only spread retrogradely and has fewer systemic and cytotoxic effects (*11*), but the near 100% fatality rate of rabies in humans relegated the RV tracer to a peripheral role. Gradually, these obstacles were reduced or eliminated by redesigning the viruses through genetic modifications, resulting in different trans-synaptic viral tools for different applications. Both monosynaptically restricted (*12*, *13*) and multisynaptic (*14–17*) retrograde tracing become possible at a moderate biosafety level. We can now initiate tracing from single cell-types(*18*), or even a single cell (*19*), while the genetically encoded activity sensors expressed by the viral tracer allow us to monitor the activity of the circuits in a high throughput manner (*15*, *20*).

The first genetically modified tracer viruses were based on the Bartha strain of pseudorabies virus (*21–24*). Unlike herpes simplex virus or rabies virus, PRV is not a human pathogen. PRV can infect all mammals except primates (*25*). The Bartha strain was isolated in 1961 by plaque morphology after random mutagenesis and used as a vaccine strain against the Aujeszky's disease which primarily affects pigs, dogs, and cats. While wild-type PRV can spread both retro- and anterograde, the Bartha strain can only spread retrogradely (*26*). It has lower virulence than wild-type PRV, as well as reduced cytotoxicity (*27*). Replacing non-essential genes with reporter genes in the Bartha genome resulted the first genetically modified viral tracers(*22–24*). After the genome of both the wild-type and the Bartha PRV had been sequenced it soon became clear that only a few of the multiple mutations in the Bartha genome resulted in the beneficial characteristics of the Bartha PRV. Since we found that the Bartha genome is less stable than the wild-type genome (meaning a more frequent loss of the transgenes during replication) we combined the benefits of the Bartha and wild-type PRV in a single virus by reintroducing the beneficial Bartha mutations in the genome of the wild type virus. To find the optimal PRV tracer, we generated a series of PRV viruses with different genetic modifications

and reporter gene expression. (see details in Chapter 1). The first time, we inserted a genetically encoded calcium indicator into the PRV genome and measured neuronal activity from transsynaptically labeled neurons. Subsequently we used PRV tracers to identify inhibitory neurons in the retinal INL circuits controlling the pupillary light reflex and circadian light entrainment (Chapter 2). These tracers proved very useful for tracing multisynaptic circuits and targeting multiple-order neurons from the periphery, but they lacked the rigor necessary for identification of the exact order between neurons. To do so, one has to restrict the viral spread from the initially infected starter neuron only to its direct contacts. This can be achieved by deleting an essential gene from the viral genome and inserting it exclusively into the starter neuron as a transgene. This defective virus can spread from the starter cell where all components are present to the first-order contacts, but it cannot spread further from these first-order neurons due the lack of this essential gene. If a retrograde trans-synaptic virus is modified in a monosynaptically restricted manner, it can be used to trace all the first-order presynaptic neurons of the starter neuron. The technique become available after monosynaptically restricted rabies virus was introduced in 2007 (*12*). The rabies virus has only 5 genes, all of which are essential for the trans-synaptic spread (*28*). One of these genes (G) encodes the rabies virus glycoprotein (RV-G) required for the virus to enter the host cell from the extracellular space, and also for cell-to-cell trans-synaptic spread. A G-deleted rabies virus can only spread from those cells when RV-G is expressed in an alternative way. The rabies G can be placed into neuronal cells using different gene delivery techniques, including plasmid electroporation, viral delivery, and transgenic technologies. In Chapters 3, 4 we used adeno-associated virus mediated gene delivery to express the RV-G in different types of retinal neurons in order to trace their first-order presynaptic partners with monosynaptically restricted, G-deleted rabies virus.

Non-image-forming vision

A large part of the human brain is dedicated to computing visual information. Visual input to the brain is through the optic nerve, which originates from retinal ganglion cells. Unlike other

sensory systems, visual input arrives in the brain after massive pre-processing by the retina (*29*). The retina is a multilayered neuronal tissue at the back of the eye whose function is not only to decode the light into a biological signal, but also to compress the data before transmitting to the brain. In mice, the image from the visual field is captured by 1 million photoreceptors, but their signal ends up on only 45,000 ganglion cells, whose axons form the optic (*30*). On the other hand, while there are only three types of photoreceptors in the mouse eye and they differ only in their sensitivity to wavelength and light levels, there are at least 30 types of ganglion cell, each responding in a unique way to the different static and dynamic components of the visual image (*31*). The computation from the pixel-wise representation of the photoreceptor layer to the feature extracting representation of the ganglion cell layer is performed by neuronal microcircuits between the photoreceptor layer and the ganglion cell layer. This layer is called the inner nuclear layer (INL) and it contains 40-80 cell types (*32*, *33*), including excitatory bipolar cells and inhibitory horizontal and amacrine cells. Therefore I call the presynaptic circuit of the retinal ganglion cells INL circuits, however amacrine cells are present in the ganglion cell layer as well. Drawing the INL circuits of each ganglion cell type is fundamental to understanding vision.

Vision, like all other sensory systems, can be divided into conscious, cortex-related functions and subcortical reflexes (*34*). The conscious part of vision is seeing, which we can also call image formation, while non-conscious vision includes the optokinetic reflexes, the pupillary light reflex (PLR), and circadian light entrainment. The contribution of retinal ganglion cell types to cortical and subcortical vision is only partially elucidated. In my work I was focusing on those ganglion cell channels which conduit to non-image-forming vision (*35*, *36*). There are two groups of ganglion cells – both include multiple cell types - which are known to provide input to subcortical vision. Direction-selective ganglion cells control the optokinetic reflexes (*37*), and intrinsically photosensitive ganglion cells control the PLR and circadian light entrainment(*38*).

Intrinsically photosensitive retinal ganglion cells (ipRGCs)

At least five retinal ganglion cell types express melanopsin, a light-sensitive protein (*39*). Melanopsin allows these neurons to detect light without cones and rods: they are therefore called intrinsically photosensitive retinal ganglion cells (ipRGCs) (*38*). Just like other ganglion

cells, these neurons receive inputs from the photoreceptor layer through presynaptic circuits. It has been shown that ablation of these neurons in mice leads to the complete elimination of the pupillary light reflex (PLR) and circadian light entrainment (CLE) and ipRGCs are therefore considered to be the principal ganglion cell channels of these subcortical visual functions (*35*). Melanopsin double knock-out mice revealed that the PLR requires the presence of melanopsin to reach maximum constriction of the pupil only at very high light intensities, while at lower light intensities cone and rod inputs were sufficient for the PLR (*35*). Thus INL circuits not only participate in the image-forming vision, but also in the non-image-forming vision. Furthermore, ipRGCs have five subtypes (M1-M5 ipRGCs) which have distinct morphological and physiological characteristics (*39*). In Chapters 2, I present our results on the identification of the presynaptic inhibitory cells of M1 and M2 ipRGCs. Most of the studies on ipRGCs were focusing on their role in non-image forming vision and their intrinsic photosensitivity but a number of findings indicated that ipRGCs can have a role in image forming vision as well (*39*–*41*). On the other hand due to the lack of genetic tools allowing the selective ablation of single ipRGC subtypes, it is not clear if all ipRGCs have a role in non-image forming vision, especially the latest discovered M4 and M5 subtypes. I am addressing these dilemmas in Chapter 5.

Direction-selective retinal ganglion cells

The other group of ganglion cells known to control non-image-forming visual functions are the direction-selective ganglion cells. These neurons respond to a moving object differently when it crosses their receptive field from different directions. The response is strongest when the object arrives from the preferred direction, and weakest when it approaches from the opposite, null direction. There are three types of DS cells in the mouse retina: ON DS cells (*42*) respond to the leading edge of the moving object, OFF DS cells (*43*) respond to the trailing edge, and ON-OFF DS cells (*44*) respond to both the leading and the trailing edges. Based on their preferred directions, ON DS cells have three subtypes (upward, downward, and lateral), and ON-OFF DS cells have four subtypes (upward, downward, temporal, and nasal), while OFF DS cells are all tuned to upward-moving stimuli. They also differ in their morphology and central projections. It is known that the asymmetric input of starburst amacrine cells in the presynaptic INL circuit of

DS cells has a primary role in the formation of the direction selectivity in the ganglion cells (*45*). However, the precise wiring diagram and the development of the symmetry is unknown. These questions are addressed in Chapters 3 and 4.

Chapter 1 - Genetically timed, activity-sensor and rainbow transsynaptic viral tools

***Balint K**, Boldogkoi Z, ,Awatramani GB, Balya D, Busskamp V, Viney TJ, Lagali PS, Duebel J, Pásti E, Tombácz D, Tóth JS, Takács IF, Scherf BG, Roska B.*

Summary

We developed retrograde, transsynaptic pseudorabies viruses (PRVs) with genetically encoded activity sensors that optically report the activity of connected neurons among spatially intermingled neurons in the brain. Next we engineered PRVs to express two differentially colored fluorescent proteins in a time-shifted manner to define a time period early after infection to investigate neural activity. Finally we used multiple-colored PRVs to differentiate and dissect the complex architecture of brain regions.

Introduction

A major challenge in understanding the structure and function of different neural circuits is that they are usually intermingled and perform parallel computations. A wide variety of electrophysiological and optical methods exist to assay neural activity from single or groups of neurons in specific brain regions, but efficient tools to monitor the activity of multiple neurons in an identified circuit are not available. Transsynaptic rabies (RV) (*46*) and pseudorabies (*14*, *24*, *47*, *48*) (PRV) viruses expressing GFP or RFP are effective for labeling neurons in the same functional circuit within a complex mesh of local neural circuits in vivo or in vitro(*12*, *16*) , but these tools cannot report neuronal activity. Instead, electrophysiological techniques (*12*, *47*)

which are not well suited for studying activity from multiple fluorescently marked neurons, have been used (*12*, *16*, *47*).

Results and discussion

To develop PRVs that report the activity of infected neurons (activity sensor PRVs), we inserted a gene encoding a ratiometric (CFP and Citrine) Ca^{2+} indicator, TN-L15 (*49*), into PRV genomes and named the resulting constructs As1-PRVs. We constructed 7 different PRV strains expressing TN-L15 under the regulatory control of the major IE1 promoter of human cytomegalovirus (CMV promoter). The recombinant PRVs were either derivatives of the Bartha strain, which is a retrograde tracer, or the wild-type Kaplan strain (*50*) that had been engineered to be retrograde by deleting the gI and gE genes of the virus (*51*).

We screened all generated PRVs for expression and stability of the inserted expression cassette, and measured their cytotoxicity and infectivity. Stability was an important criterion as we found that some TN-L15–expressing strains lost either one or both components of TN-L15 (CFP and Citrine), during replication in cell culture. Among the stable As1-PRVs, the As1-PRV08 strain had the highest expression (**Figure 1-1 A**) and we therefore used this strain for subsequent experiments. As1-PRV08 had the same retrograde spreading properties in mice as the well characterized GFP-expressing retrograde PRV152 strain (*16*, *17*, *47*) (**Figure 1-1 D,E**). TN-L15 expression in mouse retinal ganglion cells from As1-PRV08 was significantly higher ($P < 0.01$) than the expression in transgenic mice using the Thy1 (also known as Thy1.2) promoter(*52*) (**Figure 1-1 B**). At this high expression level, fine morphological details can be analyzed in live tissue.

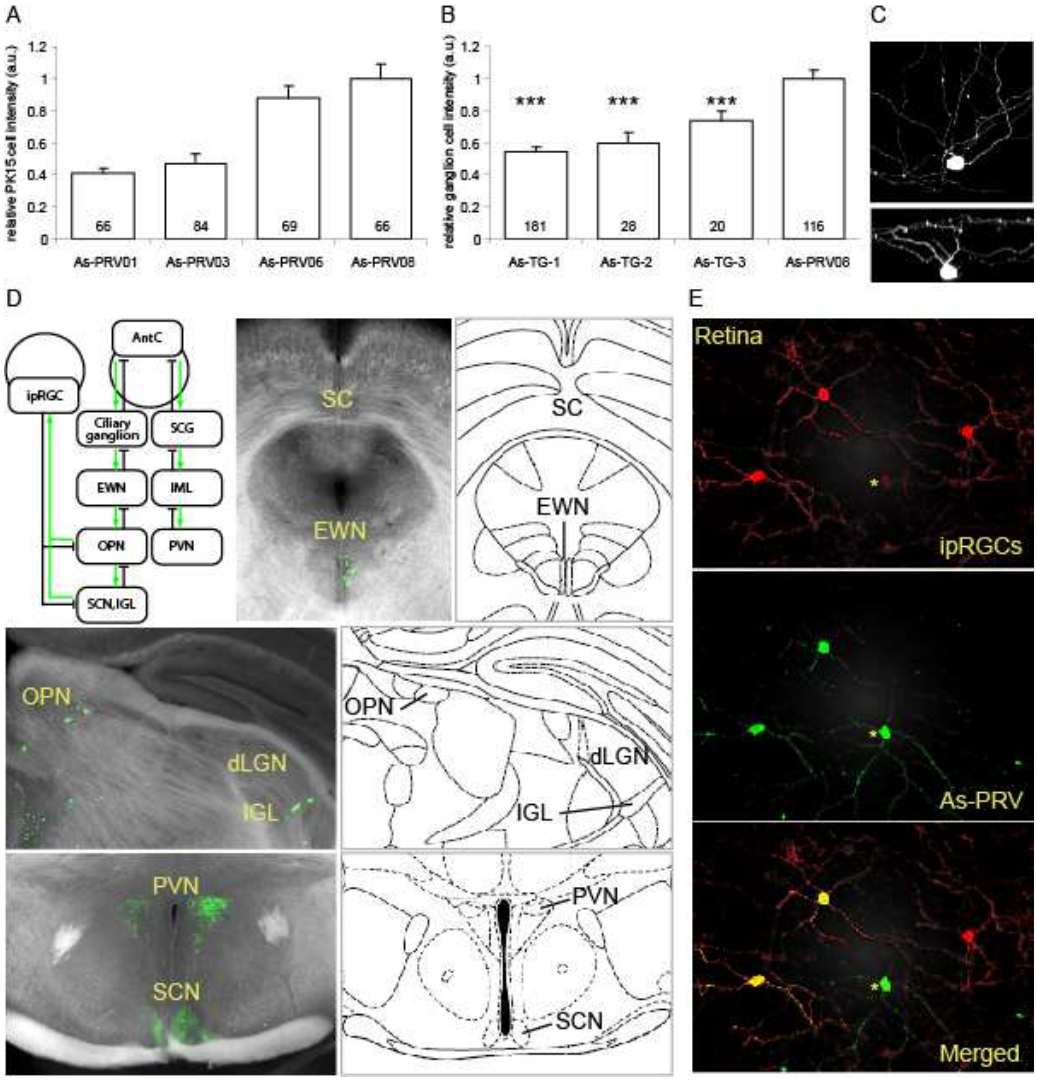

Figure 1-1. *As1-PRVs spread retrogradely and express high levels of Ca indicators.*

(A) *TN-L15 expression level in cultured fibroblast cells (PK15) infected by different As1-PRV strains (As1-PRV01, 03, 06 and 08.* ***(B)*** *Comparison of TN-L15 expression level between retinal ganglion cells in three different transgenic mouse strains, under the Thy1.2 promoter, and in As1-PRV08-infected animals.* ***(C)*** *Two-photon image of an As1-PRV08-labeled retinal ganglion cell in whole mount superfused retina. Top (up) and side (down) view of a 3D image stack.* ***(D)*** *Schematic diagram of the pupillary reflex pathway. Green arrows indicate a retrograde route along the reflex pathway (top, left, SCG: superior cervical ganglion, IML: intermediolateral nucleus of the thoracic spinal cord, PVN: paraventricular nucleus). Labeled brain areas after As1-PRV08 injection into the AntC of the right eye..* ***(E)*** *Melanopsin antibody staining of the left retina 4 days after As1-PRV08 injection into the right AntC. Anti-melanopsin in red (upper panel), anti-GFP in green (middle panel). Lower panel is the merge of the two stainings. Yellow star indicates an M2 type ipRGC, which has lower melanopsin expression and consequently faint anti-melanopsin labeling. Error bars represent s.e.m. Numbers in bars indicate number of samples.*

We tested whether As1-PRV08 would be a suitable tool for monitoring Ca^{2+} concentration changes evoked by pharmacological or physiological stimulation in neurons located several synapses away from the initial inoculation site. We injected As1-PRV08 into either the anterior chamber of the right eye or into the primary visual cortex (V1) of mice and tested putative retrogradely labeled retinal ganglion cells for TN-L15 expression in the contralateral eye. To reach these ganglion cells, the virus would need to travel retrogradely through at least one (from V1 through the lateral geniculate nucleus) or at least three (from the anterior chamber via the pupillary reflex pathway) synapses.

When TN-L15 is illuminated with a two-photon laser at B850 nm, a rise in Ca2+ concentration leads to an increase in Citrine fluorescence and a decrease of CFP fluorescence owing to fluorescence resonance energy transfer (FRET) (*49*). We isolated the retina and measured Citrine and CFP fluorescence by two-photon laser microscopy. First, we activated labeled ganglion cells pharmacologically by puff application of glutamate in the vicinity of V1 back-labeled ganglion cells. This resulted in an increase (46.65 ± 4.16%, n = 16) in the Citrine:CFP fluorescence ratio (**Figure 1-2 A**), suggesting that glutamate induced an increase of the Ca^{2+} con-centration in these cells. Next we used physiological light stimuli to activate anterior-chamber back-labeled, As1-PRV08–infected cells, which are intrinsically photosensitive ganglion cells (ipRGCs; **Figure 1-2 B**). Light stimulation (500 ms, 3 $x10^{14}$ photons cm^{-2} s^{-1}) produced a strong (13.28 ± 1.23%, n = 27) increase in the Citrine:CFP fluorescence ratio in the labeled ipRGCs. We chose ipRGCs for this test because the light response of ipRGCs is slow and therefore a brief photostimulation did not interfere with collection of fluorescent light. Notably, all cells that produced large Ca2+ transients (>10%) had dendrites in the distal part of the inner plexiform layer, suggesting that strongly responding cells are M1 subtypes of ipRGCs(*16*, *53*–*55*). These results suggest that neural activity can be recorded optically from As1-PRV08–infected cells located several synapses away from the injection site (**Figure 1-2 C**).

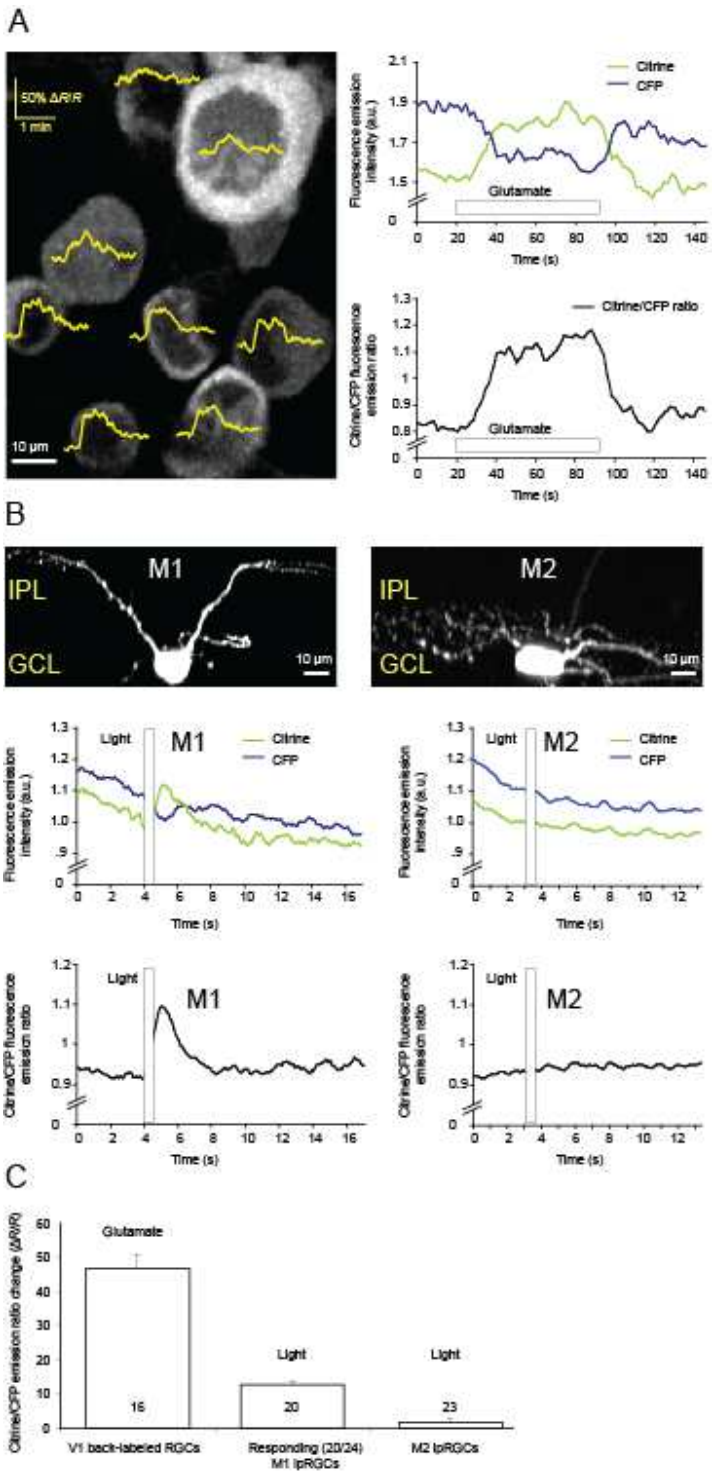

Figure 1-2. *As1-PRV08 reports neural activity. (**A**) Different retinal ganglion cells back-traced with As1-PRV08 from V1 (left). Glutamate-induced increase of Citrine:CFP fluorescence ratio is plotted on each labeled ganglion cell body (R is the ratio before stimulation and DR is the change in the ratio evoked by stimulation). An example of the change in emission intensity of Citrine and CFP (top right), and the change in the Citrine:CFP ratio (bottom right) during glutamate application (rectangle is shown). Scale bar, 10 mm. (**B**) Ca2+ imaging of light-evoked response of As1-PRV08 infected ipRGCs. Side projections of two-photon stacks of an M1 type of ipRGC (left) and of an M2 type of ipRGC (right). IPL, inner plexiform layer; GCL, ganglion cell layer. Graphs are plots of fluorescence before and after light stimulation (vertical bars) in the corresponding cells. Scale bars, 10 mm. (**C**) The strength of the responses during pharmacological (glutamate) and physiological (light) stimulations, based on the Citrine:CFP ratio. Error bars, s.e.m. RGC, retinal ganglion cell; a.u., arbitrary units. Twenty out of 24 cells responded to light (middle bar, **C**).*

Similar to all currently used transsynaptic viral tracers (PRV and RV), the activity sensor PRVs replicate in the infected cells, which ensures that the signal intensity does not decrease while the virus spreads within a neural pathway. However, replication-competent viruses are also toxic to cells at late stages of infection, and therefore it would be desirable to gain information about the phase of viral infection.

We therefore engineered PRV viruses, called timer PRVs (Ti-PRVs), that expressed two fluorescent proteins (GFP and DsRed2) with different kinetics and intracellular distribution (**Figure 1-3 A**): membrane-targeted green fluorescence appeared at the early stage of infection (primary fluorescent protein), while the soluble red reporter was detectable several hours later (secondary fluorescent protein). Membrane targeting of the primary fluorescent protein enhanced the morphological identification of the labeled neurons. Similar to As1-PRV08, these strains were retro-grade tracers (data not shown). Although both green and red fluorescent markers were under the control of the CMV promoter, expression of the red marker was delayed by 2–8 h in cell culture (Ti1-PRV07, 7.1 ± 0.09 h, n = 43; Ti2-PRV08, 7.9 ± 0.1 h, n = 47; and Ti3-PRV05, 1.93 ± 0.07, n = 39; **Figure 1-3 B**). Because of the longer time before expression in Ti1-PRV07 and Ti2-PRV08, we used these strains for subsequent analyses.

To test whether the delay between red and green reporter expression was preserved in vivo, we injected Ti1-PRV07 (expressing membrane bound GFP and DsRed2) into the anterior chamber of the right eye in mice and analyzed the brain nuclei of the pupillary reflex pathways 3.5 d after infection (**Figure 1-3 C**). In the Eddinger-Westphal nucleus (EWN), which is the first station of the viral spread in the brain, the expression of GFP and DsRed2 was similar (green:red ratio, 1.2 ± 0.046, n = 8). In contrast to the EWN, GFP levels were higher compared to DsRed2 in the olivary pretectal nucleus (OPN; green:red ratio, 7.5 ± 2, n = 8), inter-geniculate leaflet (IGL; green:red ratio, 14.896 ± 1.33, n = 8) and the suprachiasmatic nucleus (SCN; green:red ratio, 19.27 ± 3.4, n = 8), which are one or two steps further in the retrograde route of the virus. These results confirmed that GFP can be detected earlier than DsRed2 in vivo.

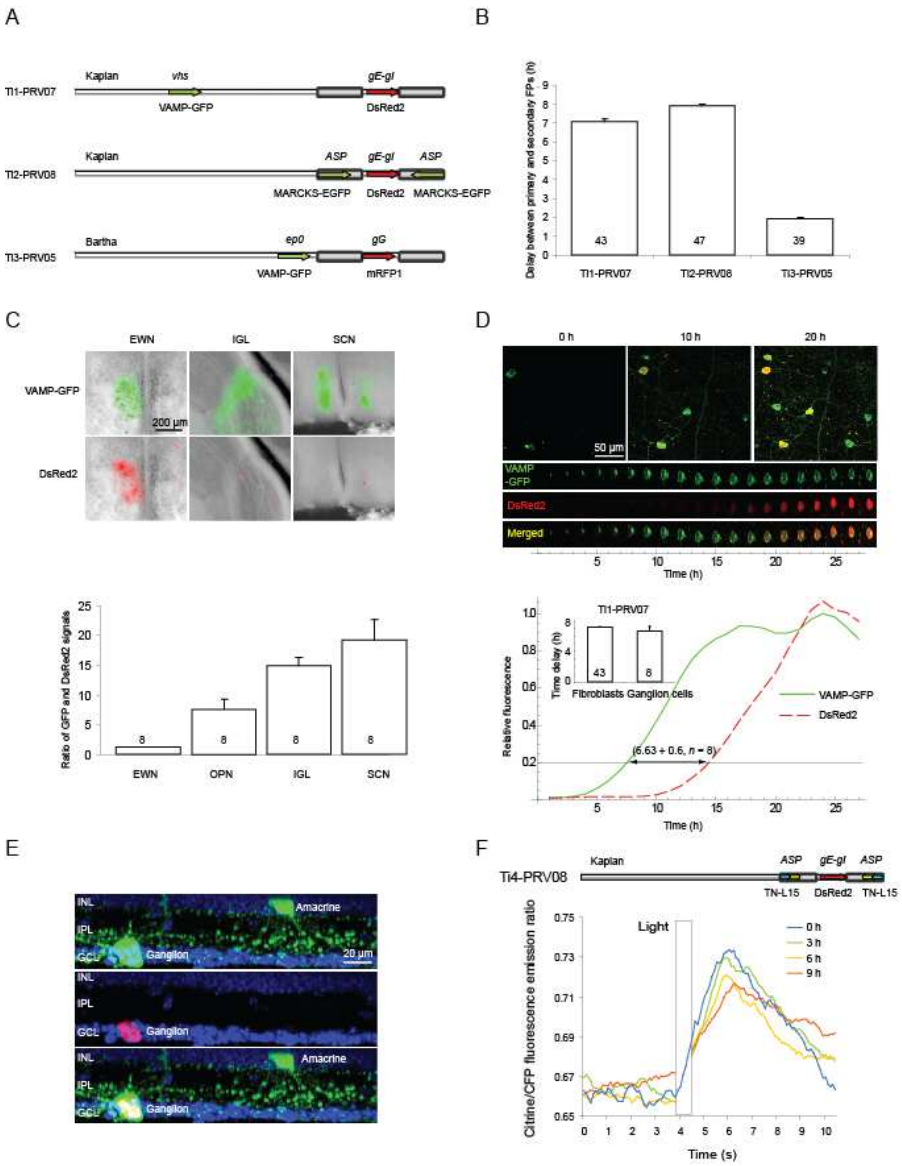

Figure 1-3. *Timer PRVs define a time window early after infection. (**A**) Ti-PRV genome variants used in this study. Labels above the schematic indicate viral regions into which markers are inserted; labels below indicate the inserted markers. vhs, virion host shut-off gene; gE-gI, glycoprotein E and I genes; ASP, putative antisense promoter; ep0, early protein 0; and gG, glycoprotein G. Kaplan and Bartha are PRV strains. (**B**) Time between the appearance of the green and red fluorescence in cultured fibroblast cells infected with the indicated Ti-PRVs. (**C**) Green:red fluorescence emission ratio in different brain regions 3.5 d after Ti1-PRV07 was injected into the anterior chamber of the mouse right eye. (**D**) Two-photon microscopy images of Ti1-PRV07 backlabeled retina collected at indicated times after dissection. The images below show the green and red signals from a single ganglion cell, and the curves depict the time course of the green and red fluorescence in single cells. Inset, time delay between appearance of green and red fluorescence in cultured fibroblast cells and in retinal ganglion cells. (**E**) Ti1-PRV07 infected retina stained with rabbit antibody to GFP (green), chicken antibody to RFP (red) and the nuclear label 4',6-diamidino-2-phenylindole (DAPI). A postsynaptic ganglion cell, which is both green and red, and a presynaptic amacrine cell, which is only green, are shown. (**F**) Genome of the Ti4-PRV08 and a plot of light-induced Ca2+ responses measured with Ti4-PRV08 from an ipRGC during 9 h after removing the retina from the left eye of the mouse. Labels in the schematic are as in (A). Error bars, s.e.m. Scale bars, 200 mm (C), 50 mm (D) and 20 mm (E).*

To estimate the time delay between the appearance of GFP and DsRed2 fluorescence in neural tissues, we isolated the contralateral retina 30 h after lateral geniculate nucleus infection and performed three-dimensional-tile, time-lapsed two-photon imaging of the green and red signals. At the beginning of the imaging session, only few ganglion cells were labeled. We only analyzed cells that became green and later red during the experiment and therefore were not fluorescent at the time when we isolated the retina. Similar to cultured cells, the expression of DsRed2 in retinal ganglion cells was delayed by 6.6 ± 0.6 h (n = 9, Ti1-PRV07; **Figure 1-3 D**). Moreover, at times when ganglion cells were red and green, presynaptic inhibitory amacrine cells that were only labeled green could be detected (**Figure 1-3 E**). These results suggest that Ti-PRV could be used as an internal clock to define a 7-h window early after infection. This feature of Ti-PRVs can be used for indication of (i) the health state of neurons and (ii) the synaptic order between neurons or brain centers.

To show that the physiological state of the infected cells did not substantially change during the 7 h, we engineered PRVs with both activity sensor and timer functions by inserting TN-L15 as primary fluorescent protein into the Ti2-PRV08 genome (Ti4-PRV08; **Figure 1-3 F**). Four days after Ti4-PRV08 injection into the anterior chamber, we removed the contralateral retina and monitored light-evoked Ca2+ changes from ipRGCs by FRET. We repeated the recordings every hour until the appearance of the red fluorescence. Light-evoked Ca2+ responses were similar before the onset of red fluorescence (**Figure 1-3 F**).

To quantify the health of the infected cells during the different phases of infection we whole-cell patch clamped green and red-green ganglion cells retrogradely infected with Ti1-PRV07 from V1 and from a control uninfected group (**Figure 1-4**). We targeted cells with similar soma size. The resting potential (Vm), capacitance (Cm), resistance (Rm) and action potential amplitude ratio at the beginning and end of a light pulse was statistically not different between the control and green cells. Similarly, in red-green cells Vm, Cm and Rm were similar to those in the control group, but the amplitude ratio was higher. These results suggest that Ti-PRVs could be used as internal clocks to define a time window for functional studies: the green signal can be interpreted as ‘start recording’ and the red signal as ‘stop recording’. Between the start and stop signals the state of the cell was not significantly altered (see P values in **Figure 1-4**). As

green fluorescence can be detected 3 h after infection (in cell culture) and the appearance of the red signal is delayed by 7 h, investigation of neural function with Ti1-PRV07 can be performed for at least 10 h after infection.

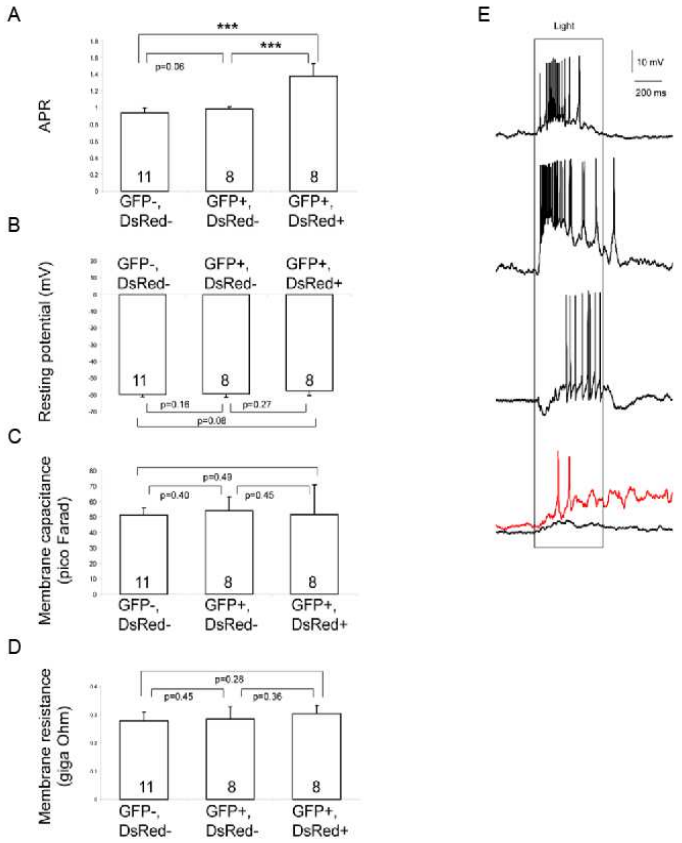

Figure 1-4. *Cellular parameters of Ti1-PRV07 labelled neurons in different stages of infection. (**A**) APR ; (**B**) resting potential; (**C**) membrane capacitance and (**D**) membrane resistance of unlabeled, GFP positive and GFP and DsRed positive cells. (**E**) Examples of whole cell patch recordings of membrane potentials from an unlabeled (top), two different GFP positive (middle) and a GFP and DsRed positive cell stimulated with a 500 ms white light at 10^{13} photons cm^{-2} s^{-1} (black curves) or 10^{16} photons cm^{-2} s^{-1} (red curve) intensities.(Note: Impairment of the light responses, shown by the lack of spiking at lower light intensities were observed only in a subset of the DsRed positive cells (3 of 8), but never in the DsRed negative cell populations). Error bars represent s.e.m. Numbers in bars indicate number of samples.*

To facilitate the tracing of several circuits in combination, we constructed 29 PRV strains expressing different fluorescent proteins (rainbow PRVs; **Figure 1-5 A**): cyan (emission maximum = 475 nm), teal (492 nm) green (507 nm), yellow (527 nm), orange (559 nm), red (582 nm) or cherry (610 nm). We made these PRVs both with the membrane-bound (11 PRVs) and soluble (18 PRVs) forms of the fluorescent proteins. The membrane-bound variants enhance the visualization of the morphology of fine neural processes whereas the soluble ones facilitate cell counting and enable a general assessment of the spatial arrangement of the labeled cells.

These viruses can be used in two different ways. First, owing to the intermingled arrangement of brain circuits, the separation of retrogradely marked circuits might be a challenge. Injecting a cocktail of rainbow PRVs could help to separate cells that belong to the same circuit. We injected a mixture of three differentially colored PRVs (cyan, green and cherry) to V1 and examined the retina 3 d later (**Figure 1-5 B**). The cyan, green and cherry circuits overlapped in the retina, and the colors could help to dissect locally the distinct ganglion cell circuits.

Second, when the different axonal target regions of distinct circuits embedded in a brain area are known, but the spatial organization of these circuits is not established, differentially colored PRVs could be injected to the target regions as described for two colors before(*56*). We injected red PRVs to the precomissural nucleus, green PRVs to the primary visual cortex and blue PRVs to the subthalamic nucleus. The locus ceruleus, a common nucleus of the infected pathways, was labeled with all three colors but with different spatial arrangements within the nucleus (**Figure 1-5 C**). These results suggest that combined rainbow PRVs may be useful for dissecting the local circuit organizations of brain nuclei.

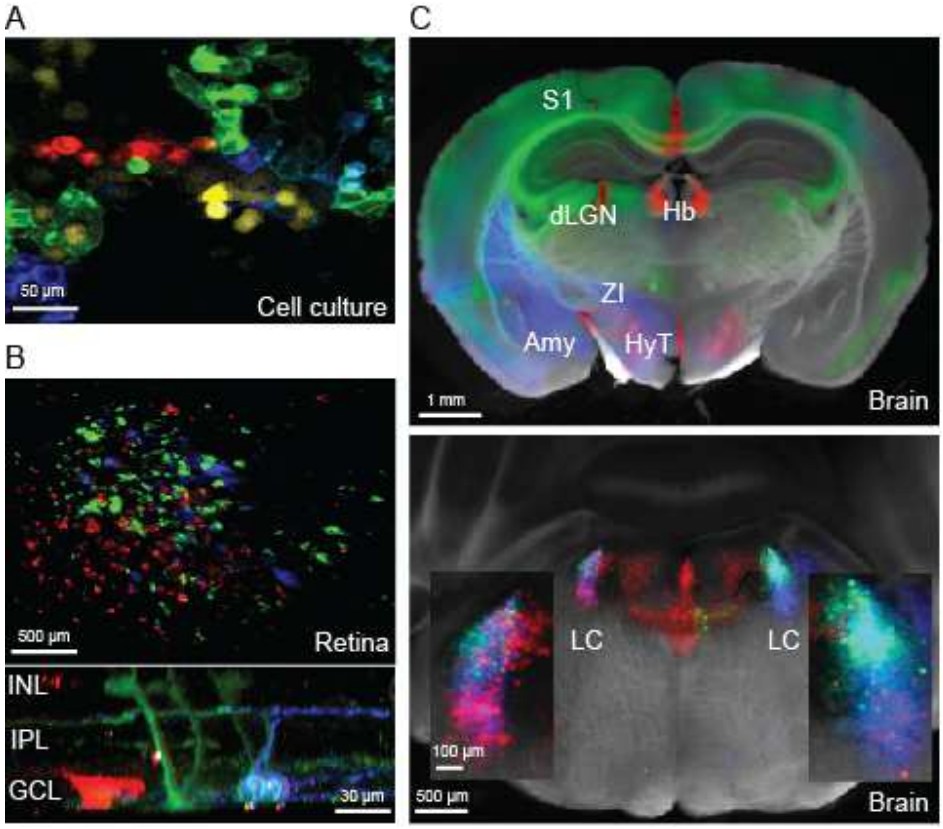

Figure 1-5. *Multiple, colored PRVs reveal spatial organization of parallel circuits. (**A**) memCerulean-PRV06 (blue), memGreen-PRV06 (green), yellowPRV06 (yellow), memCherry-PRV06 (red) in cultured PK15 cells. Colors were deconvolved using spectral unmixing. (**B**) Top view of the left retina 3 d after injection of a cocktail of blue, green and red PRVs into the contralateral V1 (top). Side projection of a two-photon z-dimension stack shows morphologically distinct retinal ganglion cells labeled with different Rainbow viruses. (**C**) Rainbow PRVs with different colors were injected into different brain nuclei (memCherry-PRV06 into precomissural nucleus, memGFP-PRV06 into V1 and memCerulean-PRV06 into subthalamic nucleus). Example of a brain section in which different regions are transsynaptically labeled with different colors (top). Amy, amygdala; ZI, zona increta; Hb, habenular nucleus; HyT, hypothalamus; dLGN, dorsal lateral geniculate nucleus; and S1, primary sensory cortex. The locus ceruleus (LC), a common nucleus of the infected pathways, labeled with all three colors. Scale bars, 50 mm (**A**), 500 mm (**B**, top), 30 mm (**B**, bottom), 1 mm (**C**, top) and 500 mm (**C**, bottom) 100 mm (**C**, bottom insets).*

Whereas PRV-based tracers are either retrograde or both retro-and anterograde, the H129 strain of the herpes simplex virus (HSV) has been reported to spread only in the anterograde direction (*57*). As the PRV and HSVs are closely related viruses, similar genetic modifications of

H129 could possibly lead to the development of anterograde viral tracers with similar properties to the ones reported here.

The low affinity of TN-L15 (dissociation constant, Kd = 1.2 mM) ensures that cellular calcium is not substantially buffered, but makes it difficult to detect small changes in Ca2+ concentration. New generations of genetically encoded probes can resolve small Ca2+ concentration fluctuations(*58*). Moreover, other genetic tools to activate or silence neurons could also be incorporated into trans-synaptic viruses, leading to insights about the computations performed by distinct neural circuits. As PRVs have a wide host range, the described viral tools can be used in many species, including mice, swine, hamsters, rabbits, rats, dogs, cats, goats, cattle, sheep and chickens (*59*).

Chapter 2 - Local Retinal Circuits of Melanopsin Containing Ganglion Cells Identified by Transsynaptic Viral Tracing

*Viney TJ, **Balint K**, Hillier D, Siegert S, Boldogkoi Z, Enquist LW, Meister M, Cepko CL, Roska B.*

Summary

Intrinsically photosensitive melanopsin-containing retinal ganglion cells (ipRGCs) control important physiological processes, including the circadian rhythm, the pupillary reflex, and the suppression of locomotor behavior (reviewed in (*60*)). ipRGCs are also activated by classical photoreceptors, the rods and cones, through local retinal circuits (*61*). ipRGCs can be transsynaptically labeled through the pupillary-reflex circuit with the derivatives of the Bartha strain of the alphaherpesvirus pseudorabies virus(PRV(*23*, *62*) that express GFP (*14*, *47*, *48*, *63*–*65*). Bartha-strain derivatives spread only in the retrograde direction (*17*). There is evidence that infected cells function normally for a while during GFP expression(*21*). Here we combine transsynaptic PRV labeling, two-photon laser microscopy, and electrophysiological techniques to trace the local circuit of different ipRGC subtypes in the mouse retina and record light-evoked activity from the transsynaptically labeled ganglion cells. First, we show that ipRGCs are connected by monostratified amacrine cells that provide strong inhibition from classical-photoreceptor-driven circuits. Second, we show evidence that dopaminergic interplexiform cells are synaptically connected to ipRGCs. The latter finding provides a circuitry link between light–dark adaptation and ipRGC function.

Results and Discussion

PRV152 Labels Morphologically Distinct Retinal-Ganglion-Cell Subtypes

To transneuronally label intrinsically photosensitive melanopsin-containing retinal ganglion cells (ipRGCs) via the autonomic circuits, we injected PRV152 into the anterior chamber (AntC) of the right eye of mice (**Figure 2-1 A**) (*17*). After 3.5–4.5 days, we isolated the retina from the left eye

(n = 36 retinas), where several ganglion cells were brightly labeled with GFP (**Figure 2-1 B**). Dendrites of mouse retinal ganglion cells of different morphological and physiological classes(*27*) ramify at different depths (strata) in the inner plexiform layer (IPL) (*33*). All of 170 analyzed GFP-expressing ganglion cells in the left retina were found to have dendrites in only two IPL strata at depths of 30% (64%) and 89% (66%). These dendritic strata were outside the two outer strata labeled by the calretinin antibody (**Figure 2-1 C and D**) and in the same strata specifically labeled by the melanopsin antibody (**Figure 2-1 C and D**). In the brain, similar retinorecipient nuclei were labeled bilaterally (**Figure 2-1 E**) as described in hamsters and rats (*17*, *66*), including the suprachiasmatic nucleus (SCN), the intergeniculate leaflet (IGL), and the olivary pretectal nucleus (OPN). The dorsal lateral geniculate nucleus (dLGN) and the superior colliculus (SC) were not labeled, even at 5 days after infection (**Figure 2-1 E**). Ganglion cells in other retinal strata can be labeled from the superior colliculus and the primary visual cortex(V1), ruling out the possibility that only certain subtypes of ganglion cells have receptors for pseudorabies virus (PRV). These experiments suggest that contralateral PRV152 infection into the AntC labels subclasses of mouse ganglion cells that project to the SCN, the IGL, and the OPN, which are known targets of melanopsin-expressing ganglion cells(*53*).

Three and a half to four days after virus infection, 99% (79/80 cells counted from two infected retinas) of the labeled cells were melanopsin positive, whereas the fraction among all ganglion cells is estimated at 1%–2%(*67*) suggesting that during the first wave of infection, almost all labeled ganglion cells are ipRGCs. However, around 5 days after virus infection, only 50% of the GFP- expressing ganglion cells were positive for melanopsin (*23*). One explanation is that these non-ipRGC types also project to the SCN, IGL, and OPN, because at 5 days, the dLGN and the SC are not labeled (**Figure 2-1 E**). An alternative explanation is that PRV spreads through gap junctions to other types of ganglion cells (*67*). The PRV-infected ipRGCs could be classified into three classes based on their depth of dendritic ramification. **Figure 2-1 F** shows examples of melanopsin and GFP double-stained ganglion types. Each type could be found at all eccentricities. M1 ipRGCs (n = 66) have dendrites close to the inner nuclear layer (INL), M2 ipRGCs (n = 69) have dendrites close to the ganglion-cell layer (GCL), and M3 ipRGCs (n = 35) are bistratified, having dendrites in the same strata as M1 and M2 cells (**Figure 2-1 F**).

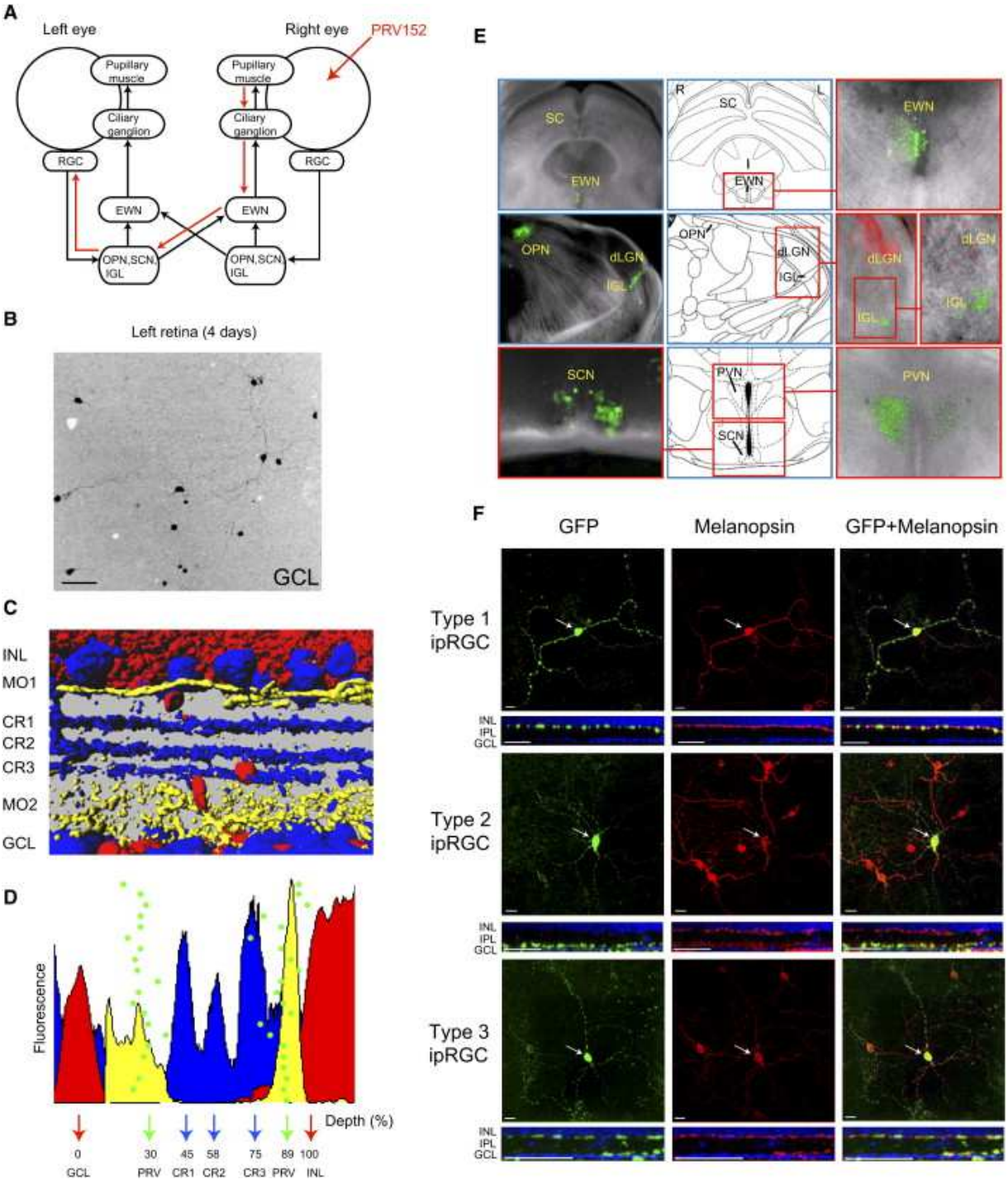

Figure 2-1. *PRV152 Retrogradely Spreads from the Right Eye to Subtypes of Ganglion Cells in the Left Retina* ***(A)*** *Simplified schematic of the PRV spread 7 and 13. Red arrows indicate the route of retrograde virus spread from the right eye to the contralateral retinal ganglion cells (RGCs).* ***(B)*** *Low-resolution (10×) confocal scan of the left retina 4 days after injection, showing several GFP-labeled ganglion cells. The scale bar represents 100 μm.* ***(C)*** *Confocal reconstruction from a 200-μm-thick vibratome section. Calretinin antibody (blue) labels three strata in the*

*IPL (CR1, CR2, and CR3). Cell nuclei are labeled with DAPI (red). Melanopsin antibody (yellow) labels two strata (MO1 and MO2). (**D**) The depths of dendritic ramification of PRV152-labeled ganglion cells are plotted as green dots. Monostratified cells are presented as one dot; bistratified ganglion cells are presented as two dots. The fluorescence as a function of depth is plotted for calretinin (blue), DAPI (red), and melanopsin (yellow). The x axis shows the relative depth in the IPL; the y axis shows normalized fluorescence. (**E**) Brain regions labeled 5 days after injection of PRV152 into the anterior chamber (AntC) of the right (R) eye and PRV614 (RFP-expressing variant) to the left (L) visual cortex. PRV152 (green) labels the EWN, OPN, IGL, SCN, and hypothalamic paraventricular nucleus (PVN) but not the SC or the dLGN. PRV614 (red) labels the dLGN. Diagrams are taken from [43]. (**F**) GFP-labeled ipRGC subtypes in the left retina 3.5–4 days after PRV152 injection into the AntC of the right eye. Colocalization with GFP (green) and melanopsin (red) antibodies is shown. Arrows indicate soma. Side views are shown below top views and indicate dendritic stratification in the IPL between the INL and the GCL (marked by DAPI, blue). Scale bars represent 20 μm.*

Common Properties of Local Circuits of PRV152-Labeled Ganglion Cells

The local circuits of the PRV152-infected ganglion cells can also be labeled. PRV152 was injected into the AntC of the right eye (n = 32 retinas) as before, but, in order to mark the cells in synaptic contact with the PRV152- infected ipRGCs, we waited 5 days before dissecting the left retina. At this time, a number of other cell types in the INL became intensely GFP positive (**Figure 2-2 A**). The newly infected melanopsin-negative ganglion cells were not yet surrounded by cells in the INL, suggesting that the passage of PRV from non-ipRGCs has not yet happened at this stage of infection. Most of the labeled cells in the INL were amacrine and Müller glia cells (**Figure 2-2 A**). Only occasionally have we seen labeled bipolar cells. Müller-cell labeling was consistently observed solely near the cell bodies of infected ganglion cells, whereas labeled amacrine cells were scattered concentrically around them (**Figure 2-2 A**). Müller cells are easily identified from confocal stacks because their processes span the entire width of the retina. Their presence was further confirmed by staining of the retina with an antibody against glutamine synthetase, a marker specific to Müller cells (**Figure 2-2 B**). Double labeling with melanopsin and GFP showed that Müller cells were indeed in close proximity to ipRGCs (**Figure 2-2 C**). Surprisingly, however, no Müller-cell labeling was seen in the retina when PRV152 was injected into the V1 (**Figure 2-2 D and E**). In the INL, only the amacrine cells were GFP positive. This was true even at 5 days after injection into the V1, at a time when large numbers of

ganglion and amacrine cells are labeled. These results suggest that Müller cells make specialized contacts with ipRGCs but not with ganglion cells that project to the dLGN and subsequently to the V1. Amacrine-cell labeling is unlikely to be caused by a release of PRV particles from Müller cells, because infection of amacrine and Müller cells is temporally and spatially independent. Further support for the idea that amacrine labeling is caused by transsynaptic release from ganglion cells comes from the finding that retinal strata juxtaposed to the GFP positive thin strata were not labeled. We find a clear difference between the number of infected amacrine and bipolar cells in the retina because very few bipolar cells become GFP-positive through PRV spread from the contralateral eye. To show that this observation in our experiments was not due to the fact that some of the labeled ganglion cells contain their own photopigments and, therefore, might lack bipolar input, we investigated retinas retrogradely labeled with PRV152 from the SC or the V1. Similar to results of tracing from the contralateral eye, very few bipolar cells were detected after SC or V1 injection (data not shown). Other studies have also shown that melanopsin expressing ganglion cells receive synaptic input from bipolar cells (*61*),(*68*). This suggests that PRV152 spreads across unconventional, bipolar-to-ganglion ribbon synapses with low efficiency. Interestingly, the bipolar and amacrine-cell GFP-expression levels were the same, suggesting that differential expression from the cytomegalovirus (CMV) promoter of PRV is not the cause of inefficient bipolar labeling.

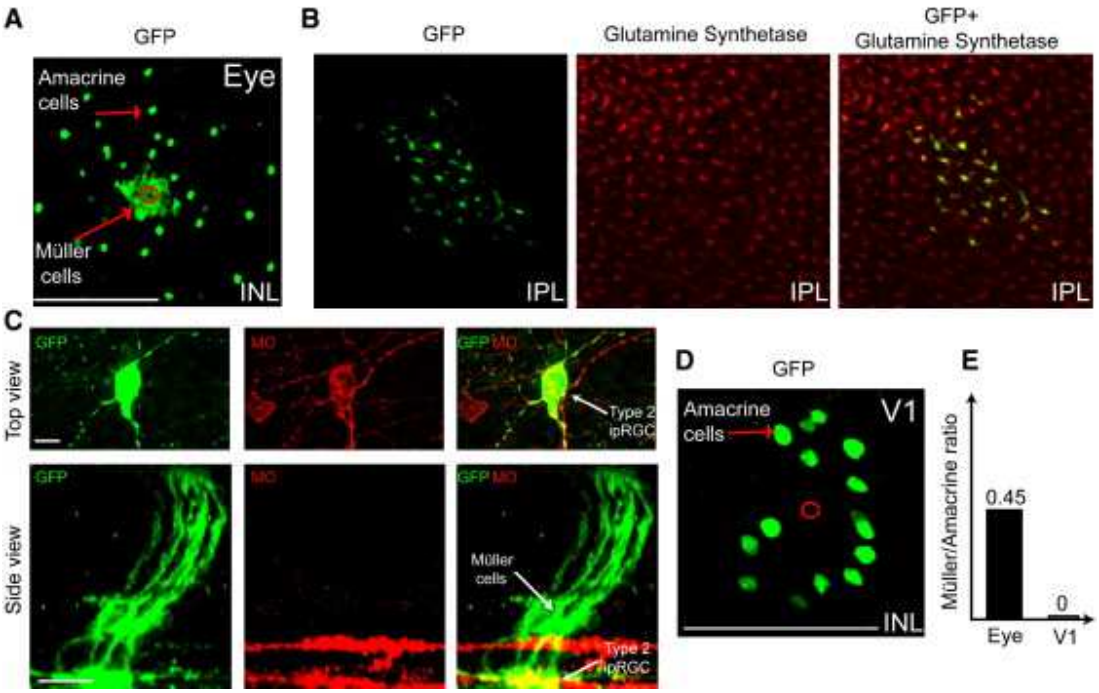

Figure 2-2. *GFP-Labeled Local Circuits 5 Days after PRV152 Injection into the AntC of the Right Eye or the Right V1 Cortical Region. (**A**) GFP-positive amacrine and Müller cells in the INL. The red circle indicates the position of the GFP-positive ganglion cell in the GCL. The scale bar represents 100 μm. (**B**) Colocalization of the Müller-cell marker glutamine synthetase (red) and GFP (green) for cells that are centrally GFP labeled near a GFP-positive ganglion cell. The depth of the scan is in the middle of the IPL. (**C**) Top views of a GFP-labeled M2 ipRGC with corresponding side views of labeled Müller cells. GFP (green) colocalizes with melanopsin (MO, red). The scale bar represents 15 μm. (**D**) A confocal scan in the INL near a labeled ganglion cell, 5 days after contralateral V1 injection, shows only GFP-labeled amacrine cells and no Müller cells. The position of the ganglion-cell body in the GCL is indicated by the red circle. The scale bar represents 100 μm. (**E**) Proportion of the number of Müller and amacrine cells in the INL after contralateral-eye and V1 injection at 5 days.*

Monostratified Amacrine Cells Provide Inhibitory Input to M2 ipRGCs

We investigated the structure and function of the local circuit of M2 ipRGCs. For this detailed circuit tracing, we used low-titer virus injections (103 plaque-forming units [PFUs]) that yielded sparse circuit labeling to avoid confusion of circuits belonging to neighboring ganglion cells. These ganglion cells have dendrites in the IPL close to the ganglion-cell layer at 30% (64%, n = 57) depth. We made 3D reconstructions of the processes of amacrines that surrounded M2 ipRGCs (**Figure 2-3 A-C**). For amacrine cells that were farther away from the labeled ganglion cells, we made a number of overlapping confocal stacks and stitched them together (**Figure 2-3**

D and E). All labeled amacrine cells studied this way (n = 20), independent of their distance from the ganglion-cell body, were monostratified in the same stratum as the M2 ipRGCs. Although the GFP labeling of bipolar cells was rare (*61*) in some cases (n = 3) we could reconstruct their morphology. As expected, these bipolar cells costratified with M2 ipRGC dendrites (**Figure 2-3 F**). The structure of a M2 ipRGC local circuit, based on the detailed confocal reconstructions, is summarized in a circuit drawing in **Figure 2-3 G**. The local circuit consists of three cell types: a M2 ipRGC, a type 8 bipolar cell (based on (*69*)), and a monostratified amacrine cell. In this detailed morphological study, we could not use melanopsin colabeling because the GFP-labeled fine amacrine dendrites were only visible with rabbit anti-GFP, which was from the same species as the melanopsin antibody. We relied on the finding that at 5 days, non-ipRGCs were newly infected (were not present at 4 days); therefore, the spread of the virus to amacrines most probably had not yet happened. This is supported by the finding that non-ipRGCs were not surrounded by amacrine cells at 5 days (see above). To show more direct evidence that the identified monostratified amacrine cells are indeed connected to ipRGCs, we isolated the retina at 3.5–4 days, at the time when 99% of the labeled ganglion cells are melanopsin positive. We determined the retinal coordinates of many labeled ganglion cells with two-photon microscopy and superfused the retina with oxygenated Ringers solution for an additional day. In these experiments, we used a new virus strain (see Experimental Procedures) that expressed a membrane-bound GFP that more clearly labeled the dendrites and axons. One day after isolation (5 days after infection), we fixed the retina and stained the circuit with rabbit anti-GFP antibodies and analyzed the circuits at the marked coordinates. The analyzed circuits are therefore, with 99% probability, local circuits of ipRGCs. The morphology of the labeled amacrine cells was identical to those described above (**Figure 2-3 H**). The labeled circuit gave very strong predictions about the direct, amacrine-cell-mediated inhibitory input to M2 ipRGCs. In most vertebrates (except zebrafish (*70*)) and in all mammalian species studied, the IPL is divided into two major regions. Strata close to the GCL (sublamina B) incorporate axon terminals of ON bipolar cells; strata close to the INL (sublamina A) embody axon terminals of OFF bipolar cells (*69*). Because amacrine cells receive excitation from bipolar cells, the reconstructed amacrines must receive excitation only at light ON. Most

amacrines are inhibitory cells. If the M2 ipRGCs receive inhibitory input only from the reconstructed amacrines, inhibition should arrive at light ON but not at light OFF. Inhibition at light OFF would suggest a multistratified or bistratified amacrine cell, because OFF activity should travel vertically in the IPL from sublamina A to sublamina B (*29*). To test these predictions, we recorded light-evoked inhibitory currents from PRV-infected, GFP-labeled, M2 ipRGCs with the whole-cell patch clamp method in the voltage clamp configuration after 4 days of infection. As mentioned before, at that time, only ipRGCs were labeled. The resting membrane voltage was 258 mV 6 4 mV (n = 8). Inhibition in M2 ganglion cells was only evoked at light ON (n = 10) when the retina was stimulated with a 1 mm diameter white spot (**Figure 2-3 I**), as predicted by the structure of the PRV-labeled local-circuit elements. This finding is in strong contrast with inhibitory currents evoked in most other ON ganglion cells in the mammalian retina (**Figure 2-3 J**); in the rabbit retina, only one type of ON ganglion cell receives inhibition only at light ON. These results suggest that M2 ipRGCs receive a strong, fast inhibitory input at light onset from a single morphological type of amacrine cell.

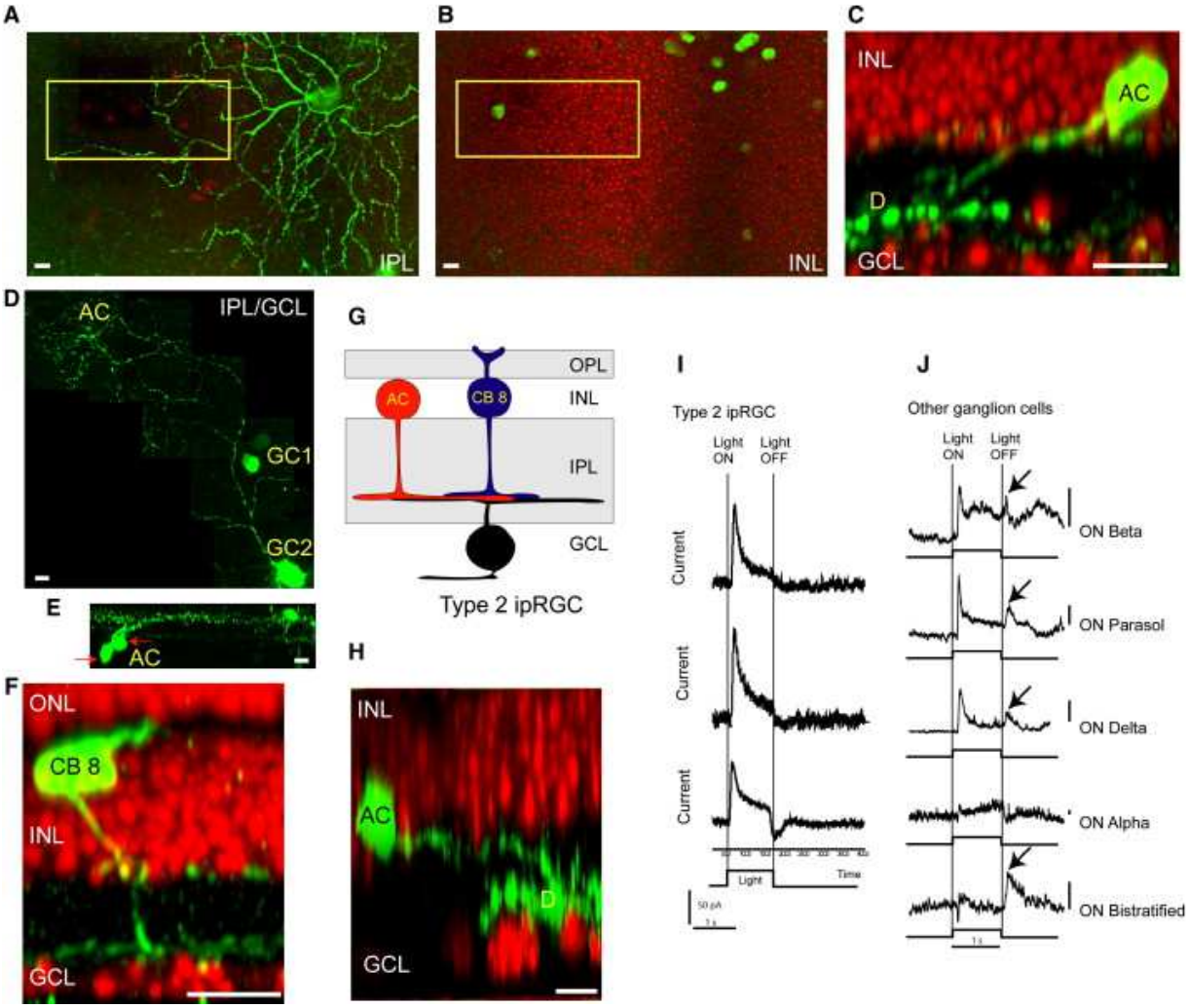

Figure 2-3. *Local Circuit and Physiology of M2 ipRGCs. (**A**) Confocal scan in the proximal part of the IPL in the left retina at 5 days after PRV152 injection into the right eye. A GFP-labeled (green) M2 ipRGC is shown. (**B**) Confocal scan of the same area as in (**A**) but in the INL. The GFP-labeled cells are amacrine cells. Cell nuclei labeled by DAPI are shown in red. (**C**) An x-z projection of a high-resolution scan of the yellow box shown in (**A**) and (**B**). An amacrine cell (AC) in contact with the dendrites (indicated by "D") of the M2 ipRGC is shown. (**D**) Five confocal scans were stitched together to show the dendritic arbor of two amacrine cells (ACs) and of a M2 ipRGC (GC2). A M1 ipRGC is also shown (GC1), although its dendrites are not visible because they are in a different depth. (**E**) An x-z projection of the stack shown in (**D**). Here the dendrites of the two amacrines, as well as the M1 ipRGC, are shown. Red arrows point to the two amacrine cell bodies. (**F**) An x-z projection of a high-resolution scan from another M2 ipRGC shows a type 8 cone bipolar cell (CB 8). (**G**) The identified cell types, based on the viral tracing, in the local circuit of M2 ipRGCs. (H) The same as (**C**), except that this amacrine cell was from an experiment where the retina was isolated at 4 days and kept in a perfusion chamber for 1 day (see main text). Scale bars represent 10 μm for all figures. (**I**) Light-evoked inhibitory currents from three different M2 ipRGCs. Inhibition cannot be detected after light OFF. The currents were measured in voltage clamp at 0mV*

*holding potential. The stimulus was a 1-mm-diameter bright spot. The timing of the stimulus is indicated by black bars. (**J**) Light-evoked inhibitory currents from five different types of ON ganglion cells in the rabbit retina. Light evokes inhibition at both light ON and light OFF in four out of the five cell types (names shown to the right of each). The OFF response is indicated by arrows. The stimulus is the same as in (**A**). Scale bars represent 100 pA.*

M2 ipRGCs receive GABAergic lateral inhibition from Arc positive amacrine cells

In order to identify the presynaptic inhibitory cells of the M2 ipRGCs we took advantage of the Gensat retina library where retinal cells are identified genetically by BAC transgenic mouse lines expressing GFP (*71*) from various promoters. We selected those lines, where only amacrine cells are labeled and the processes of the amacrine cells co-stratify with the dendrites of the M2 ipRGCs (**Figure 2-4 A**). These conditions are fulfilled by four mouse lines expressing the GFP from the following gene loci: activity-regulated cytoskeleton-associated protein (Arc), insulin-like growth factor binding protein 2 (Igfbp2), cholinergic receptor, nicotinic, alpha 3 (Chrna3) and immediate early response 5 (Ier5). To test which of the genetically labeled amacrine cells are synaptically connected to the M2 ipRGCs, we initiated transsynaptic viral tracing through the PLR in each of the mouse lines. This time we used the Red-PRV02 expressing the red fluorescent protein DsRed and imaged the INL for co-localization of the genetic marker GFP and the tracer marker DsRed. We found that only the amacrine cells identified by the Arc-GFP mouse line were co-labeled by the Red-PRV02 (**Figure 2-4 B, D**). It is known that the amacrine cells labeled in the Arc-GFP mice also express the Arc protein, therefore we call them Arc positive amacrine cells or briefly Arc cells. We found that the majority of virus labeled cells surrounding the M2 ipRGCs were also Arc positive amacrine cells (84.8% 128/151 in 5 injected animals) which indicates that the primary inhibitory neurons of M2 ipRGCs are the Arc positive amacrine cells. To assess how specific is the connection between the Arc cells and M2 cells we initiated viral tracing from the primary visual cortex in Arc-GFP mice. Since the visual cortex receives input from most of the retinal ganglion cell types through the LGN, we obtained massive labeling by the tracer in both the GCL and the INL of the retina (**Figure 2-4 C**). We analyzed those regions in the retina for co-labeling where no melanopsin positive ganglion cells has been detected. In these areas we found that only 3.6% (5/137 in 3 injected animals) of the

virus labeled cells were Arc positive amacrine cells. This indicates that Arc positive amacrine cells are specific presynaptic partners of the M2 ipRGCs. It has been shown that Arc positive amacrine cells are GABAergic inhibitory neurons (*71*), therefore we tested the effect of the GABA blocker picrotoxin on M2 ipRGCs, in order to obtain more evidence for a functional connection. Action potentials from M2 ipRGCs were recorded at loose patch configuration while stimulating the retina with different size light spots. We found that at control conditions M2 ipRGCs activated stronger by a 200 µm light spot than by a 1 mm light spot, but when picrotoxin was applied spiking rate at the 1 mm spot increased (**Figure 2-4 E**) We also performed whole-cell patch recording which allowed us to study inhibitory and excitatory inputs on M2 ipRGCs separated. We found that the 200 µm spot generated smaller inhibitory and larger excitatory currents than the 1 mm spot (**Figure 2-4 F**). These electrophysiological experiments not only support that the Arc cells have direct contact to M2 ipRGCs but also shows that Arc cells provide lateral inhibition to M2 ipRGCs, which overwrite the former view about ipRGCs characterized as bare light meters reporting the ambient illumination level. This could mean that non-image forming functions require more details of the visual scene and also raise the possibility that M2 ipRGCs has a role in image formation as well.

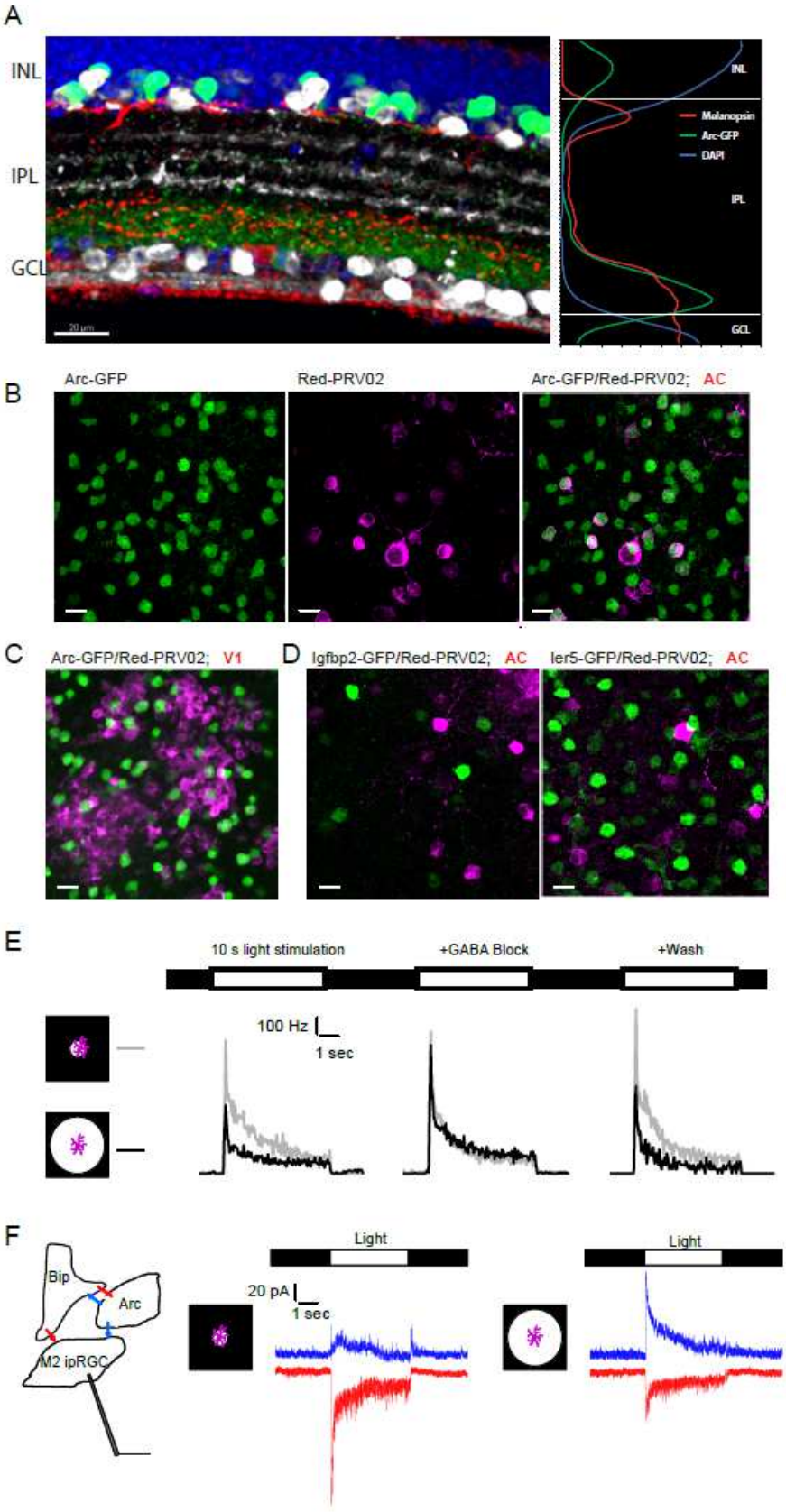

Figure 2-4. *M2 ipRGCs are synaptically connected to Arc positive amacrine cell. (**A**) Fluorescent image of a retinal slice from an Arc-GFP mouse stained against melanopsin (red), GFP (green), calretinin (gray) and the cell bodies (blue). Graph shows the signal strength of the melanopsin, GFP and nuclear staining along the inner plexiform layer. (**B**) Confocal image taken from the amacrine cell layer of an Arc-GFP mouse retina backlabeled with Red-PRV02 from the anterior chamber (AC) of the contralateral eye. GFP positive amacrine cells are shown in green, the viral labeld neurons in magenta.(Scale bars are 20 µm). (**C**) Confocal image taken from the*

Dopaminergic Interplexiform Cells Are Synaptically Connected to M1 ipRGCs

Similar to M2 ipRGCs, M1 ipRGCs were surrounded by GFP-positive amacrine cells (**Figure 2-5 A**). These amacrine cells had processes in the same strata as M1 ipRGCs. Because the morphology and stratification of the labeled INL cells were very similar to those of a well-described cell subtype, the dopaminergic interplexiform/amacrine cells, we triple-labeled retinas for tyrosine hydroxylase (TH), GFP, and melanopsin. **Figure 2-5 B-E** show that a number of amacrine cells around a melanopsin- and GFP-positive M1 ipRGC (**Figure 2-5 E**) were both GFP and TH positive. **Figure 2-5 C and D** show that TH-positive processes and melanopsin-positive dendrites of ipRGCs cofasciculate in the IPL. These results suggest that dopaminergic cells provide synaptic input to M1 cells. Dopaminergic amacrine cells in the mouse retina are interplexiform cells that have processes in the IPL and in the outer plexiform layer (OPL) (*72*). Five and a half to six days after contralateral virus infection, a number of horizontal cells become labeled with GFP (**Figure 2-5 F**). The PRV labeling of horizontal cells suggests that these cells are not only postsynaptic targets (*73*) of but also presynaptic to dopaminergic interplexiform cells. Our previous finding that PRV152 very inefficiently passes to bipolar cells and the fact that no bipolar cells were detected in the vicinity of the labeled horizontal cells (data not shown) indicate that the virus spread from interplexiform cells to horizontal cells. Interestingly, even after 7 days of infection, we could not detect rods or cones; this reinforced our conclusion that PRV152 very inefficiently crosses ribbon synapses. Dopamine is a neurotransmitter that is in the retina and controls light adaptation(*74*). Dopaminergic cells of the mouse retina are GABAergic (*72*). These cells make conventional synapses and also release neurotransmitters extrasynaptically (*74*). Our study suggests that dopaminergic cells are in synaptic contact with M1 ipRGCs. The synapse between dopaminergic cells and ipRGCs are GABAergic, dopaminergic, or both. It is possible that, similar to the synapse between dopaminergic cells and AII amacrine cells, both GABA and dopamine are released, but the

postsynaptic receptors are positioned at different distances from the release site. In either case, however, the synaptic contact between interplexiform cells and ipRGCs suggests that the activity of dopaminergic cells synaptically influences the activity of and/or gene expression in ipRGCs. Recent studies suggested that the dopaminergic system, which controls light–dark adaptation, strongly influences the circadian rhythm (*75*–*77*). Our results suggest a circuitry link between light–dark adaptation and ipRGC function.

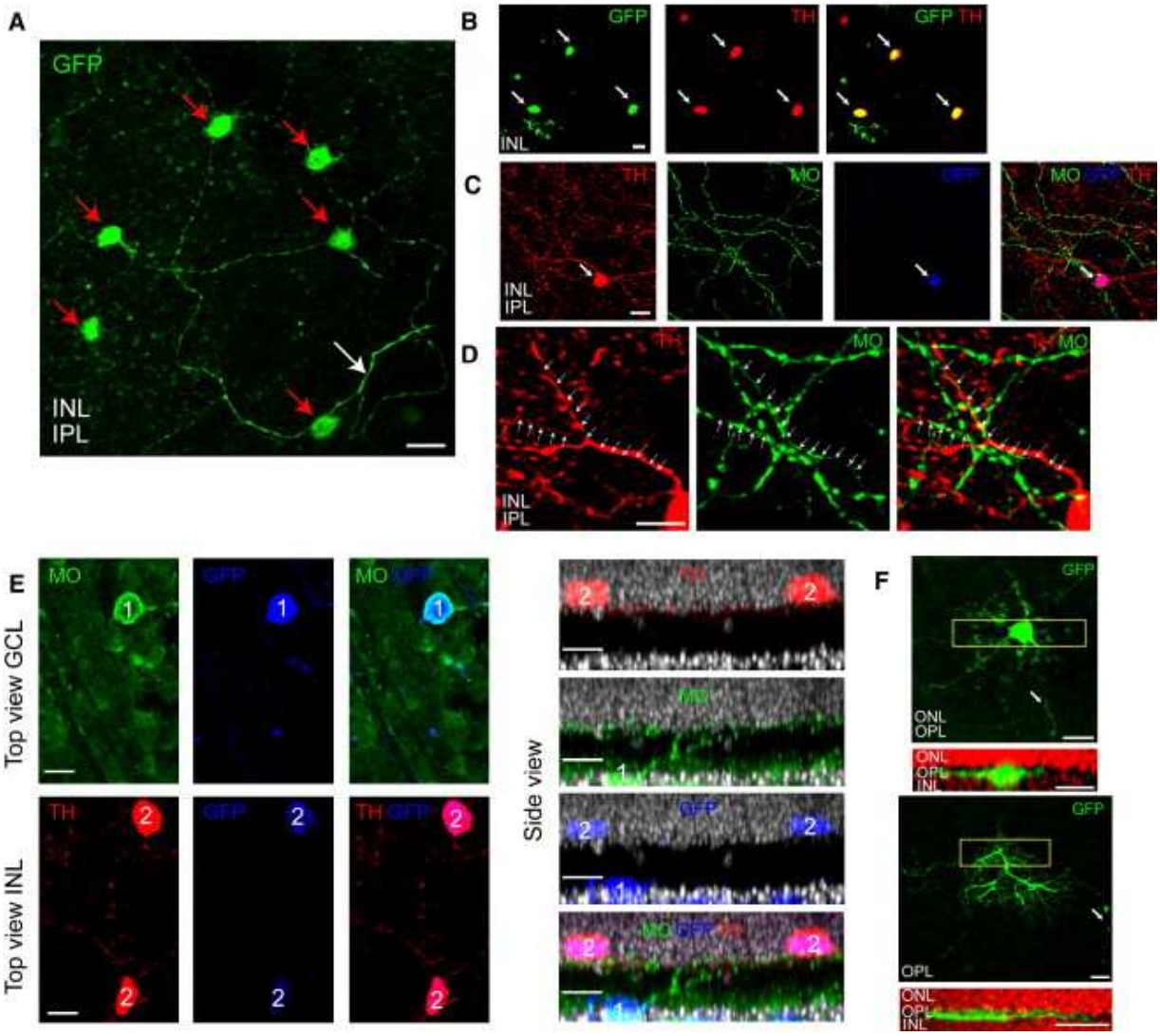

Figure 2-5. *M1 ipRGCs Are Synaptically Connected to Dopaminergic Amacrine/Interplexiform Cells.* ***(A)*** *Confocal scan of a region in the INL–IPL border around a GFP-positive M1 ipRGC. A descending dendrite of the ipRGC is shown by the white arrow. Red arrows point to a number of GFP-positive cell bodies in the INL.* ***(B)*** *Colocalization of GFP (green) and TH (red) in amacrine cells around a M1 ipRGC in the INL. Arrows point to double-labeled cells.* ***(C)*** *Triple staining for TH (red), melanopsin (green), and GFP (blue) at the IPL–INL border. The arrow points to the TH- and GFP-positive amacrine cell.* ***(D)*** *Higher magnification of a region in (C). Arrows point to cofasciculating TH- and melanopsin-positive processes.* ***(E)*** *Triple staining for TH (red), melanopsin (green), and GFP (blue) labels a M1 ipRGC (cell labeled as "1") and two dopaminergic amacrines (two cells labeled as "2") in close proximity. Top views are on the left and side views are on the right.* ***(F)*** *Top: A confocal scan of a region in the IPL–ONL border shows a labeled horizontal cell body (left) and axon terminal (right). Bottom: A Z axis view of the yellow-window region from the upper panels. Scale bars represent 15 μm for all panels.*

Chapter 3 - Spatially asymmetric reorganization of inhibition establishes a motion-sensitive circuit

*Yonehara K, **Balint K**, Noda M, Nagel G, Bamberg E, Roska B.*

Summary

Spatial asymmetries in neural connectivity have an important role in creating basic building blocks of neuronal processing (*78*, *79*). A key circuit module of directionally selective (DS) retinal ganglion cells is a spatially asymmetric inhibitory input from starburst amacrine cells (*80–82*). It is not known how and when this circuit asymmetry is established during development. Here we photostimulate mouse starburst cells targeted with channelrhodopsin-2 (*83*) while recording from a single genetically labelled type of DS cell (*84*). We follow the spatial distribution of synaptic strengths between starburst and DS cells during early postnatal development before these neurons can respond to a physiological light stimulus, and confirm connectivity by monosynaptically restricted trans-synaptic rabies viral tracing. We show that asymmetry develops rapidly over a 2-day period through an intermediate state in which random or symmetric synaptic connections have been established. The development of asymmetry involves the spatially selective reorganization of inhibitory synaptic inputs. Intriguingly, the spatial distribution of excitatory synaptic inputs from starburst cells is significantly more symmetric than that of the inhibitory inputs at the end of this developmental period. Our work demonstrates a rapid developmental switch from a symmetric to asymmetric input distribution for inhibition in the neural circuit of a principal cell.

Results and discussion

DS retinal ganglion cells respond to movement in a 'preferred' direction with robust spiking, but show minimal response to movement in the opposite, or 'null', direction (*79*, *85*, *86*). DS cells receive GABAergic inhibitory inputs from starburst amacrine cell processes pointing in the null direction, but not from those pointing in the preferred direction (*80*, *87*). Glutamatergic excitatory input from bipolar cells is also directionally selective. Interestingly, starburst cells

also communicate to DS cells using acetylcholine (*88*). but this excitatory connection seems to be symmetric (*89*). Directional selectivity is present before eye opening (around postnatal day 13 (P13) in mice), as well as in dark-reared animals (*84*, *90*) indicating that the establishment of circuit asymmetry does not require visual experience. How and when such highly specific synaptic connections are established between starburst and DS cells during development remain unknown. Retinal cells do not respond to light until P10–11 in mice (*91*) with the exception of melanopsin-containing ganglion cells (*38*), which limits the ability to follow the early development of functional connectivity. Directional selectivity may develop by the asymmetric refinement of previously formed inhibitory connections or, alternatively, the inhibitory synaptic inputs form asymmetrically. To distinguish between these possibilities, we probed the spatial distribution of synaptic strengths from starburst amacrine cells to individual ON DS cells during postnatal development. ON DS cells respond to slow movement and are critical for mediating the optokinetic reflex (*42*, *92*, *93*). In SPIG1–GFP (SPIG1, also known as Fstl4, locus driving green fluorescent protein expression) knock-in mice, upward-motion-preferring ON DS cells are selectively labelled with GFP throughout development in most retinal regions. To activate the starburst cells of SPIG1–GFP mice before amacrine and ganglion cells receive light-driven inputs from bipolar cells, this mouse line was crossed with another line expressing Cre recombinase specifically in starburst cells (choline acetyltransferase (ChAT)–Cre knockin mice). At P0, we transduced these SPIG1–GFP 3 ChAT–Cre mice with a Cre-recombinase-dependent adeno-associated virus (AAV) carrying a reversed and double-floxed C128T mutant channelrhodopsin-2 (ChR2c) (*83*, *94*), followed by 2A–DsRed2 (ChR2c–2A–DsRed2, see Methods, **Figure 3-1 A**). 2A sequence codes for a cis-acting hydrolase element26 that creates equimolar amounts of ChR2c and red-fluorescent, soluble DsRed2. A soluble marker in the cell body allowed easier quantification of fluorescence, and therefore ChR2 expression, than in a membrane bound fusion construct. ChR2c-expressing cells are responsive to light at an intensity 50-fold lower than cells expressing wild-type ChR2 and could, therefore, be activated by light patterns generated by an overhead projector. Immunohistochemistry showed that all DsRed2-marked neurons were also positive for ChAT, a marker for starburst

cells. Conversely, a substantial fraction (60%) of starburst cells in both the ganglion cell layer (GCL) and inner nuclear layer (INL) (**Figure 3-1 B and C**) were DsRed2- labelled.

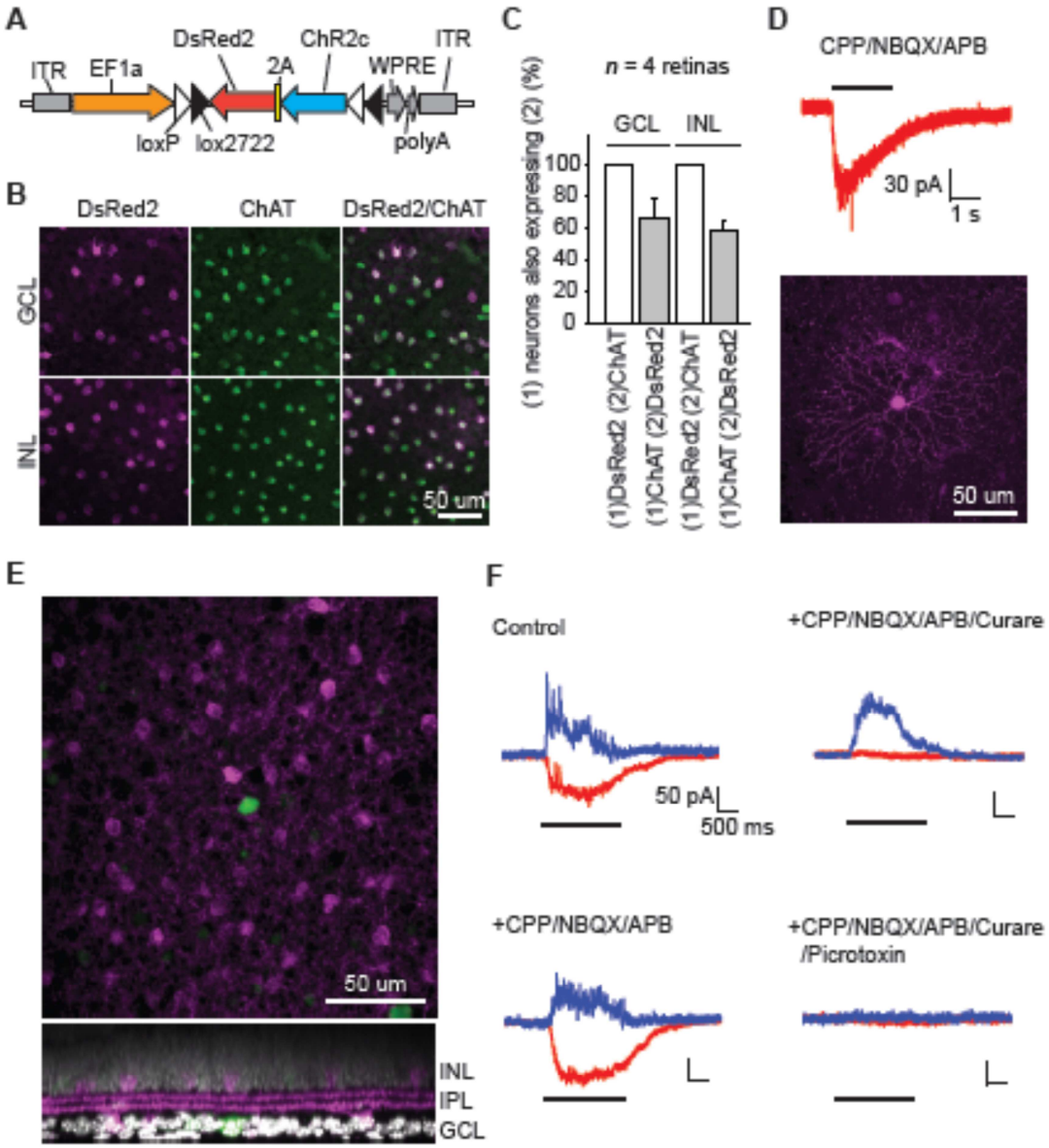

Figure 3-1. *Targeting of ChR2c to starburst amacrine cells at P8. (**A**) AAV vector. EF1a, promoter; ITR, inverted terminal repeat; WPRE, woodchuck post-transcriptional regulatory element. (**B**) Confocal images from an AAV-transduced retina. (C) Relationship between DsRed2-expressing and ChAT-positive cells. (**D**) Top, excitatory currents in an AAV-labelled starburst cell in the presence of synaptic blockers. Full-field flash stimulus. Bottom, confocal image of the recorded starburst cell. (**E**), Top, confocal image of a retina in which ON DS cells are expressing GFP (green) and starburst amacrine cells are expressing ChR2c and DsRed2 (magenta). Bottom, side-view. IPL, inner plexiform layer. (**F**), Synaptic currents recorded at −60 mV (red) and 20 mV (blue) holding potentials from a GFP-positive ON DS cell in response to a full-field flash. Error bars, s.d.*

Therefore, starburst cells, but no other cell type in these mice, are labelled red and express light-sensitive ChR2c, whereas upward motion-preferring ON DS cells are labelled green (**Figure 3-1 E**). First, we characterized the light-excitability of ChR2c-positive starburst cells in intact, isolated retinas between P6 and P9. Light illumination evoked robust currents in DsRed2-expressing cells, even in the presence of glutamatergic synaptic blockers (CPP, NBQX, APB), suggesting ChR2c as the source of the currents (**Figure 3-1 D**). Increasing illumination evoked increasing membrane potential changes in starburst cells and, as expected due to the 2A element, the red fluorescence intensity of the recorded cell bodies correlated well (R 5 0.83) with the magnitude of the membrane potential change at the stimulation intensity which is used to test the distribution of synaptic strengths in subsequent experiments. To test whether the genetically tagged neural circuit could report the synaptic strengths from starburst to ON DS cells, we isolated excitatory and inhibitory inputs to ON DS cells at P8 while stimulating ChR2cexpressing starburst cells with light patterns (see Methods). A full-field light step elicited both inhibitory and excitatory currents in ON DS cells (**Figure 3-1 F**). The inhibitory component was blocked by the GABA receptor antagonist picrotoxin, and the excitatory input by the cholinergic receptor antagonist curare. Blocking glutamate receptors had no effect on the light-evoked currents (**Figure 3-1 F**) or on the miniature excitatory postsynaptic currents (mEPSC,). mEPSCs were blocked by curare. These results confirmed that ON DS cells receive GABAergic and cholinergic synaptic inputs in response to starburst cell stimulation, but do not receive glutamatergic synaptic input from bipolar cells at this stage. The ChR2c-assisted synaptic strength mapping depends on direct connections between starburst and ON DS cells during early postnatal development. To test whether this is the case, we performed monosynaptically restricted retrograde synaptic tracing with G-deleted rabies virus(*46*) complemented with G-expressing herpes virus initiated from GFP-labelled ON DS cells (see Methods). At P6, starburst cells were rabies-labelled around infected GFP-marked ON DS cells (**Figure 3-2**), indicating that starburst cells are directly connected to ON DS cells at this developmental stage.

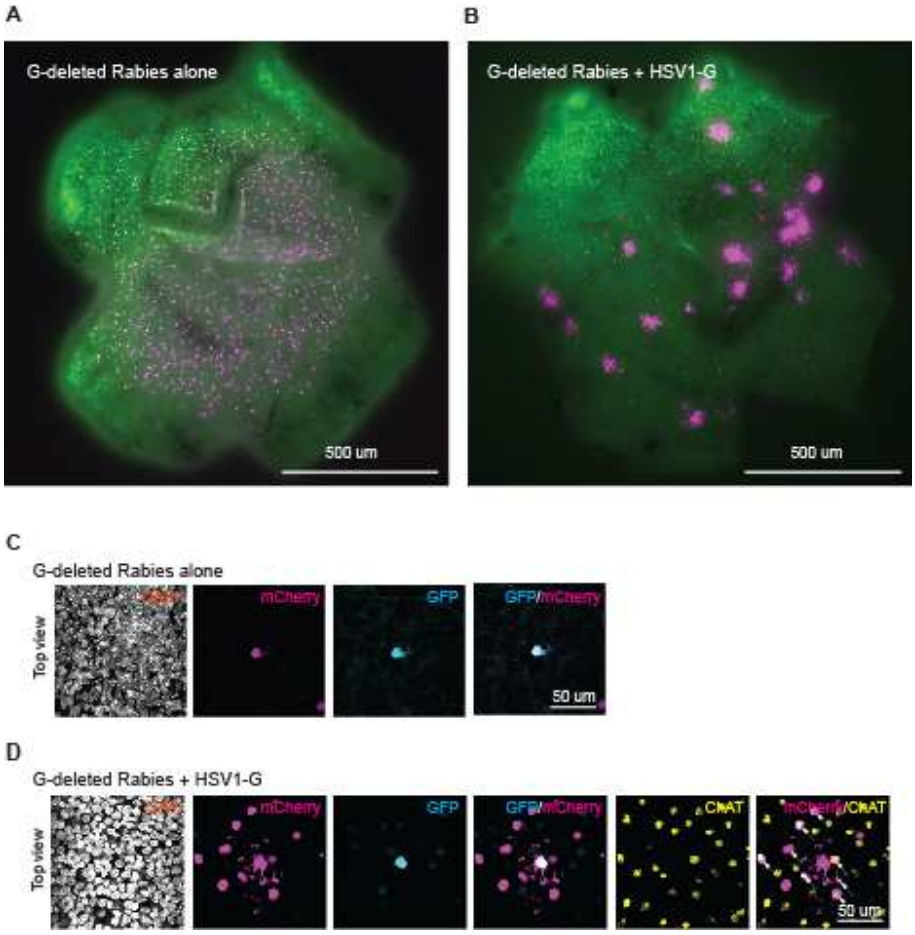

Figure 3-2. *Monosynaptically restricted circuit mapping initiated from ON DS cells. (**A and B**) Live images of SPIG1–GFP retinas at P6 in which GFP-labelled ON DS cells (green) were infected with G-deleted rabies expressing mCherry (magenta) either alone (**A**) or in combination with G-encoding herpes virus (**B**). (**C**) Confocal images of a GFP-labelled ON DS cell (cyan) infected with G-deleted rabies virus only (magenta). (**D**) Confocal images of an ON DS cell infected with both G-deleted rabies virus and G-encoding herpes virus from **B**. Most of the labelled presynaptic cells (arrows) are ChAT-positive starburst cells (yellow) in the GCL.*

Having confirmed monosynaptic connection from starburst cells already at P6, we investigated the spatial distribution of the strength of synaptic connections by stimulating starburst cells with light steps in eight sectors surrounding the recorded ON DS cells (**Figure 3-3**). We calculated a spatial asymmetry index (SAI) that quantified the degree of spatial asymmetry of the synaptic inputs to ON DS cells along the dorso-ventral axis (see Methods). We found that

the inhibitory input was already spatially asymmetric along the dorso-ventral axis by P8; stimulation of the ventral (null) side evoked more inhibitory current than stimulation of the dorsal (preferred) side. In contrast, the excitatory input was significantly more symmetric along the same axis (**Figure 3-3**). To avoid potential bias due to non-uniform viral transduction we normalized the synaptic currents with either the number of DsRed2-expressing starburst cells (using a threshold) or the sum of the measured red fluorescence (which reflects the voltage change in starburst cells, as shown before) of the starburst cells in each of the eight sectors in which the light stimulus was presented (see Methods). The normalized responses, like the recorded raw responses, also showed asymmetric inhibition and more symmetric excitation along the dorso-ventral axis at P8 (**Figure 3-3**). In contrast to P8, the raw and normalized inhibition and excitation at P6 was symmetric along the same axis (**Figure 3-3**). The lack of asymmetry in inhibition at P6 was not due to ineffective activation of starburst cells because of low ChR2c expression level, since half-maximal activation at P9, which should be similar to maximal activation at P6 in terms of eliciting changes of membrane potential, revealed asymmetry.

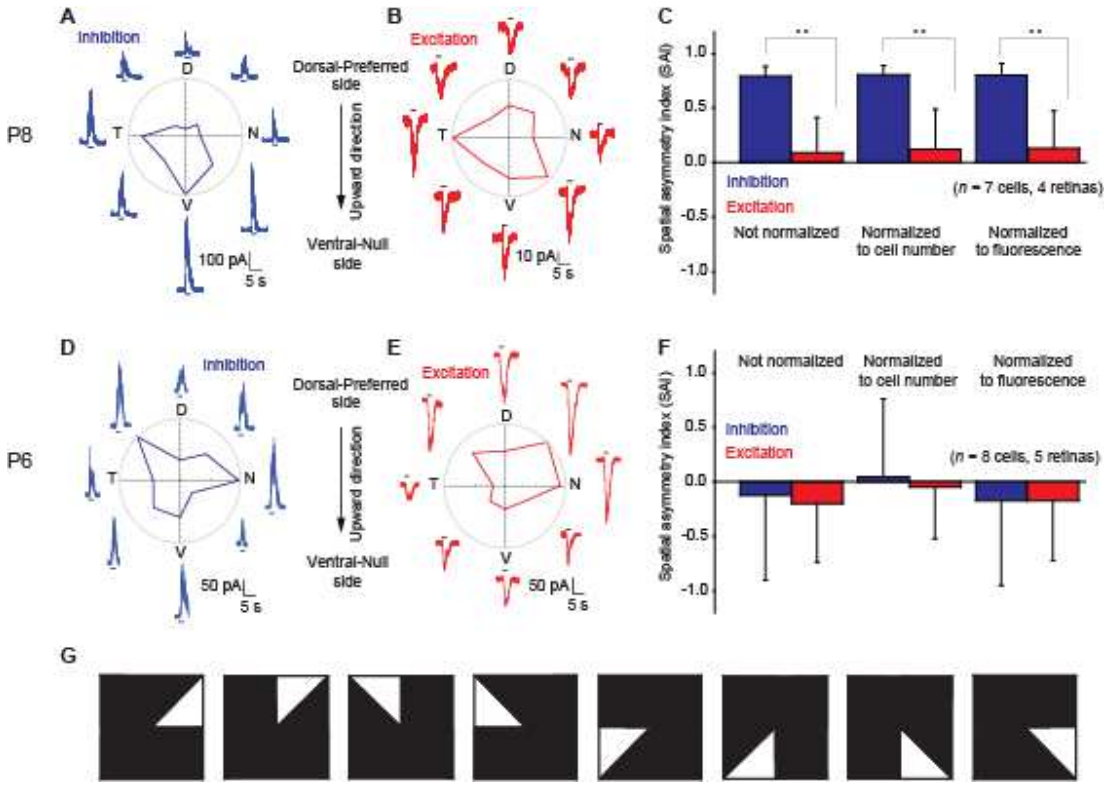

Figure 3-3. *ChR2c-assisted circuit mapping at P8 and P6. (**A–F**), Recordings from ON DS cells at P8 (**A–C**) and P6 (**D–F**). Inhibitory (**A, D**) and excitatory (**B, E**) postsynaptic currents elicited in an ON DS cell by the stimulation of eight sectors surrounding the cell. Polar plots are also shown. (**C, F**), Spatial asymmetry index (SAI) for inhibition and excitation. (**G**), Sketch of light patterns used to stimulate one of eight sectors around the recorded ON DS cell. Error bars, s.d.*

Next, we investigated the emergence of asymmetry from P6 to P9 (**Figure 3-4**). SAI of inhibition increased significantly, but there was no significant change in excitation between any pairs of days. The lack of statistically significant change in excitation was not due to saturating intensities because half-maximal activation of excitatory inputs to ON DS cells did not significantly change the SAI of excitation at P9. The mean direction of inhibitory input of individual recorded cells, computed as the vector sum of inputs for all eight directions, was random at P6 but became confined to the ventral side by P8 (direction of red bars in **Figure 3-4 H**). Because the variation in DsRed2 expression across the eight sectors was not statistically different between P6 and P9, the randomness at P6 is not due to greater variation in gene expression from AAV at earlier time points. We conclude that before P6 the spatial distribution

of inhibitory connectivity between starburst cells and ON DS cells is either random or symmetric (with some synapses having little strength). Inhibitory connectivity rapidly reorganizes to become asymmetric along the 'preferred-null' (dorso-ventral) axis between P6 and P8, whereas excitatory cholinergic input remains significantly more symmetric throughout this developmental period.

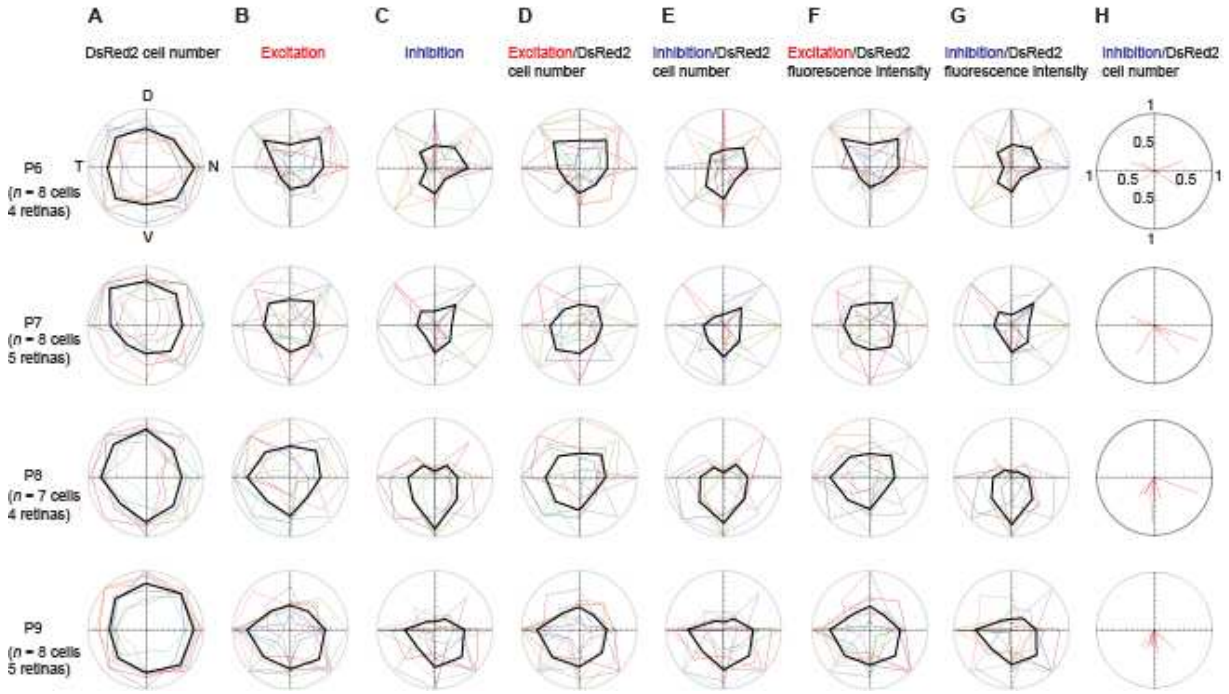

Figure 3-4. *Development of asymmetry. Coloured lines indicate normalized current responses from individual cells and the black line indicates the mean response of all recorded cells (or the mean cell number for* ***A****). Polar plot of the number of DsRed2-expressing cells (****A****), excitatory (****B****) and inhibitory (****C****) inputs, excitatory (****B****) and inhibitory (****C****) inputs normalized to the number of DsRed2 expressing cells in each sector, excitatory (****F****) and inhibitory (****G****) inputs normalized to the mean DsRed2 fluorescence intensity of cells in each sector.* ***H****, Red bars indicate the vector sum of inhibitory inputs normalized to the number of DsRed2 expressing cells in each sector.*

Is inhibitory connectivity strengthened at the ventral ('null') and weakened at the dorsal ('preferred') side or is only one of these two mechanisms driving the development of asymmetry? Since starburst cells similarly control the strength of cholinergic excitation and GABAergic inhibition to ON DS cells and excitation is not significantly different along the dorso-

ventral axis from P6 to P9, the ratio of inhibition to excitation (neither normalized) in the dorsal and ventral sides should be a measure of the inhibitory synaptic strength that depends less on the level of ChR2c expression (which increases over the days) than inhibition alone. This ratio increased in the ventral (though the increase was not significant) and decreased in the dorsal side, suggesting that 'push-pull' synapse reorganization is at work. The retinal stratum in which ON DS cells extend their dendrites embodies three different directionally selective computations that lead to preferential responses to nasal, upward and downward motion in different types of ON DS cells. We suggest that, in the physical space shared by these circuits, it is the spatially selective refinement of the distribution of inhibitory input strength to each DS ganglion cell that underlies the establishment of each directionally selective retinal circuit. Higher-order brain computations, for example orientation selectivity in the visual cortex, also rely on spatial circuit asymmetries. Mechanistic insights from the development of retinal directional selectivity may help to understand how asymmetry in cortical circuits is established.

Chapter 4 - Direction selectivity in retina is computed at a single synaptic stage

*Yonehara K, Farrow K, Ghanem A, Hillier D, **Balint K**, Teixeira M, Jüttner J, Noda M, Neve RL, Conzelmann KK, Roska B.*

Summary

Inferring the direction of image motion is a fundamental component of visual computation and essential for visually guided behavior. In the retina, the direction of image motion is computed in four cardinal directions, but it is not known at which circuit location along the flow of visual information the cardinal direction selectivity first appears. We recorded the concerted activity of the neuronal circuit elements of single direction-selective (DS) retinal ganglion cells at subcellular resolution by combining GCaMP3-functionalized transsynaptic viral tracing and two-photon imaging. While the visually evoked activity of the dendritic segments of the DS cells were direction selective, direction-selective activity was absent in the axon terminals of bipolar cells. Furthermore, the glutamate input to DS cells, recorded using a genetically encoded glutamate sensor, also lacked direction selectivity. Therefore, the first stage in which extraction of a cardinal motion direction occurs is the dendrites of DS cells.

Introduction

The visual system analyzes different categories of motion from the image flow that is projected onto the photoreceptors. Even at the front of the visual stream, in the retina, a number of parallel circuits extract information about motion. Within the different motion categories, most retinal hardware is dedicated to the analysis of the direction of motion (*45*, *87*, *95*). Three different groups of ganglion cell types are dedicated to this task in mice: ON-OFF (*44*); ON (*42*) and OFF (*43*) DS cells. Individual cell types within these three groups respond preferentially to one of the four cardinal directions—backward, upward, forward, or downward—and project their axons to various target brain regions, including the lateral geniculate nucleus, the superior

colliculus, and the medial or dorsal terminal nuclei. Both ON-OFF and ON DS cells are remarkably selective for motion direction along the axis of their preferred direction, producing no spikes, or only a few, when an image is moving opposite to the preferred, the so-called null, direction. This high degree of selectivity along the cardinal directions may be achieved by incrementally increasing direction selectivity along the photoreceptor-bipolar cell-ganglion cell route of visual information (*87*) or, alternatively, the first stage of cardinal direction selectivity is localized to retinal ganglion cells(*96*, *97*). Supporting evidence for the incremental computation of direction selectivity (**Figure 4-1 A**) has come from electrophysiological studies that have shown that both the excitatory and the inhibitory input currents recorded at the cell body of DS cells were direction selective(*42*, *80*, *87*). ON-OFF and ON DS cells receive glutamatergic excitatory input from specific types of bipolar cells and inhibitory input from starburst amacrine cells. Therefore, it has been postulated that the computation of cardinal direction selectivity is first achieved at the axon terminals of bipolar cells (*87*, *98*) and a further increase in selectivity occurs at the dendrites of DS cells and that this pre- and postsynaptically distributed processing ensures robustness (*87*). It has been shown that starburst cells are necessary for the computation of direction selectivity (*99*) and it has been proposed that the spatially asymmetric connectivity from starburst cells, as well as dendritic computations within starburst cells(*81*, *82*, *100*), provide the basis for the computation of direction selectivity. Experimental evidence for asymmetric connectivity from starburst cells to DS cells has been obtained for both ON-OFF (*101–103*) and ON (*104*) DS cells. Recordings of direction-selective activity at subcellular resolution has been shown at the dendrites of ON-OFF DS cells (*105*) but not yet at the dendrites of ON DS cells. Direction selectivity has not yet been demonstrated directly at the axon terminals of bipolar cells that provide input to any of the DS cell groups.

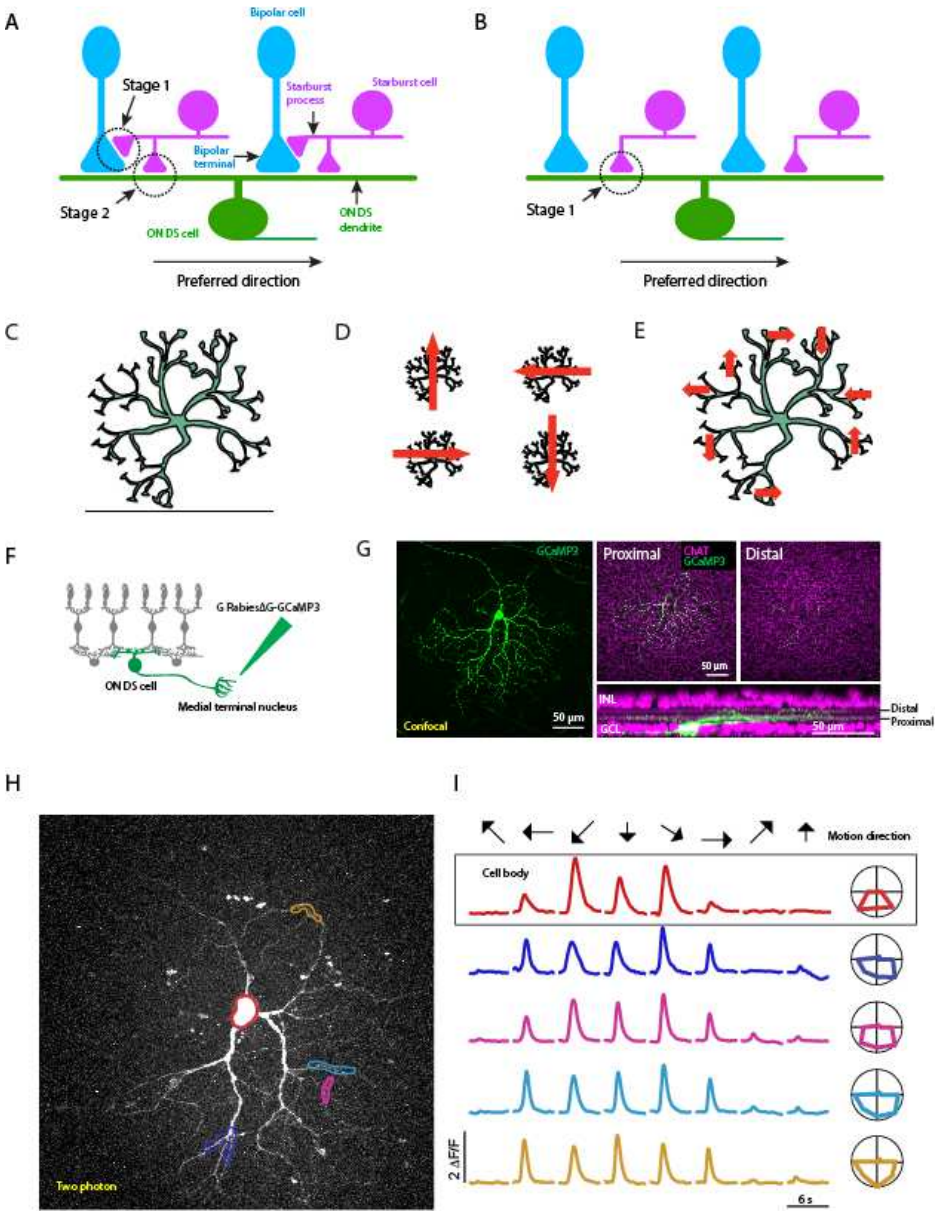

Figure 4-1. *Dendritic Segments of ON DS Cells Are Direction Selective (**A and B**) Two circuit models of cardinal direction selectivity in ON DS cells. (**A**) Cardinal direction selectivity is set up first at bipolar cell terminals and further enhanced at ganglion cell dendrites. (**B**) Cardinal direction selectivity is set up first at ganglion cell dendrites. (**C–E**) Schematics of three models for the functional units of direction selectivity in the bipolar cells: single bipolar cell type with axon terminals that are not selective for direction of motion (**C**); four different bipolar cell types having axon terminals at the same retinal layer, each bipolar cell type selective for a different direction (**D**); single bipolar cell type with four types of terminals, each selective for a different direction (**E**). (**F**) ON DS cells were targeted by GCaMP3-expressing, Gcoated G-deleted rabies virus, which was injected into the medial terminal nucleus. (**G**) Confocal images of a retina in which an ON DS cell is labeled with GCaMP3 (green). Most dendritic segments of the labeled cell are stratified at the proximal ChAT-labeled layer*

*(magenta). (**H**) Maximum image projection of two-photon image of the same ON DS cell shown in (**G**). Regions of interest are marked by colored lines. (**I**) Two-photon imaging of calcium transients in the cell body (top row) as well as in four dendritic segments of the ON DS cell shown in (**H**), in response to stimuli moving in eight different directions. Colors of the traces indicate locations of the recorded compartments in (**H**). Polar plots of the peak responses are shown on the right. See also Figure S1.*

The alternative model is that direction selectivity for cardinal directions appears first at the dendrites of the direction-selective ganglion cells (**Figure 4-1 B**) (*97*). According to this view, activity at the bipolar terminals is not selective for motion direction (**Figure 4-1 C**), and the direction selective excitatory input measured at the cell bodies of DS cells reflects the technical limitations of patch-clamp recording: the inability of an electrode positioned at the cell body to voltage clamp at the location of synapses(*45*, *106*). This model is attractive, since the spatially asymmetric connectivity at the axon terminals of bipolar cells raises conceptual problems (*107*). Since direction selectivity has been described for motion in three (ON DS cells) or all four (ON-OFF DS cells) cardinal directions, there should be either four types of bipolar cells, each being selective for one of the directions (**Figure 4-1 D**), or each bipolar cell should perform parallel processing (*108*) so that the different axon terminals of the same bipolar cell have different preferred directions (**Figure 4-1 E**). The first scenario would require many physiologically different types of bipolar cells; the second would require a sophisticated wiring between starburst cells and individual bipolar terminals. To differentiate between these two alternative models for computing direction selectivity, we used monosynaptically restricted retrograde viral circuit tracing (*11*, *109*, *110*) initiated from individual upward or downward motion-selective ON DS cells (*104*). First, we determined the types of bipolar cells that are connected to these ON DS cells. Next, using GCaMP3 (*111*) a genetically encoded calcium indicator that we expressed from the tracer virus, we performed simultaneous two-photon imaging of activity from the dendrites of ON DS cells, the axon terminals of ON DS cell-connected bipolar cells, and the processes of starburst amacrine cells during visual motion stimulation (*112*). The individual dendritic segments of ON DS cells were highly direction selective, with the same preferred cardinal direction. The processes of starburst cells were also direction selective along the centrifugal axis, from the cell body to the process tip (*113*). In striking contrast, the activity at

the axon terminals of bipolar cells that were connected to ON DS cells were not direction selective. Finally, we monitored glutamate concentration around ON DS cell dendrites during motion stimulation using iGluSnFR, a genetically encoded glutamate sensor (*114*). iGluSnFR signals were also not direction selective. Therefore, our results imply that cardinal direction selectivity appears first at the dendrites of DS cells.

Results

Dendritic Segments of ON DS Cells Are Direction Selective

To investigate whether individual dendritic segments of ON DS cells are direction selective, we labeled ON DS cells with GCaMP3 using the retrogradely transported G-deleted rabies virus (*13*) injected into the medial terminal nucleus where the axons of upward or downward motion-selective ON DS cells terminate (**Figure 4-1 F**). Immunohistochemistry with the ChAT antibody, a marker of starburst cells and the retinal layer where ON DS cells extend their dendrites, revealed that most dendritic segments of GCaMP3-marked ganglion cells were stratified at the proximal ChAT-labeled layer (*84*, *90*) suggesting successful targeting of ON DS cells (**Figure 4-1 G**). We stimulated isolated retinas with a positive contrast spot moving in eight different directions, and performed two-photon imaging of GCaMP3-labeled ganglion cells (**Figure 4-1 H and I**). Calcium responses in the cell body were highly direction selective. Next, we recorded calcium responses along dendrites of ON DS cells. We found that most dendritic segments examined were direction selective and showed the same preferred direction as the cell body. These experiments showed that the dendritic segments of ON DS cells, in a similar way to ON-OFF DS cells (*105*), are direction selective. To confirm that electrophysiological recordings from the cell bodies of ON DS cells display direction-selective excitatory and inhibitory input currents (*42*), we made two photon targeted patch-clamp recordings from ON DS cells in Spig1-GFP mice (*84*, *90*), where upward direction-selective ON DS cells are fluorescently labeled. We found both the excitatory and the inhibitory currents to be direction selective.

Type-5 Bipolar Cells Are Connected to ON DS Cells

We sought to investigate the types of bipolar cells and amacrine cells that are connected to ON DS cells. We injected the retrograde tracer AAVs or herpes viruses expressing TVA receptor and

rabies-G protein into the medial terminal nucleus. As a result, ON DS cells expressed the TVA receptor and the rabies-G protein (**Figure 4-2 A**). We then injected GCaMP3- expressing, EnvA-coated G-deleted rabies viruses into the eye. Since EnvA specifically binds to TVA, rabies virus infected only ON DS cells. Due to the presence of rabies-G expressed from AAV/herpes viruses in ON DS cells, the G-deleted rabies viruses were complemented with rabies-G and crossed one synapse retrogradely to mark the monosynaptically connected cells (*12*, *115*) (**Figure 4-2 A**). The transsynaptic spread of rabies virus has been observed to be specific to synaptically connected neurons and not to adjoining neurons that are either not connected or gap-junction connected (*11*). Injection of EnvA coated rabies virus into the eye without supplying the TVA receptor did not result in any labeling of retinal cells in 15 independent eye injections. Immunohistochemistry, together with three-dimensional (3D) confocal image reconstruction, showed that bipolar and amacrine cells were labeled together with ON DS cells. Most of the labeled amacrine cells were ChAT-positive starburst amacrine cells located in the ganglion cell layer (**Figure 4-2 B**), confirming previous results that starburst cells are presynaptic to ON DS cells (*104*). Based on the confocal image stacks, we identified a morphological type of bipolar cell as presynaptic to ON DS cells. The axon terminals of all (21/21) bipolar cells were positioned slightly above the proximal ChAT-labeled layer and were therefore categorized as type-5 bipolar cells (*69*). (**Figure 4-2 C and D**. We did not find any labeled type-6 or type-7 bipolar cells, even though the axon terminals of these bipolar cells are physically close to the dendrites of ON DS cells at the proximal ChAT-labeled layer (*69*) and have therefore had opportunities to contact ON DS cell dendrites.

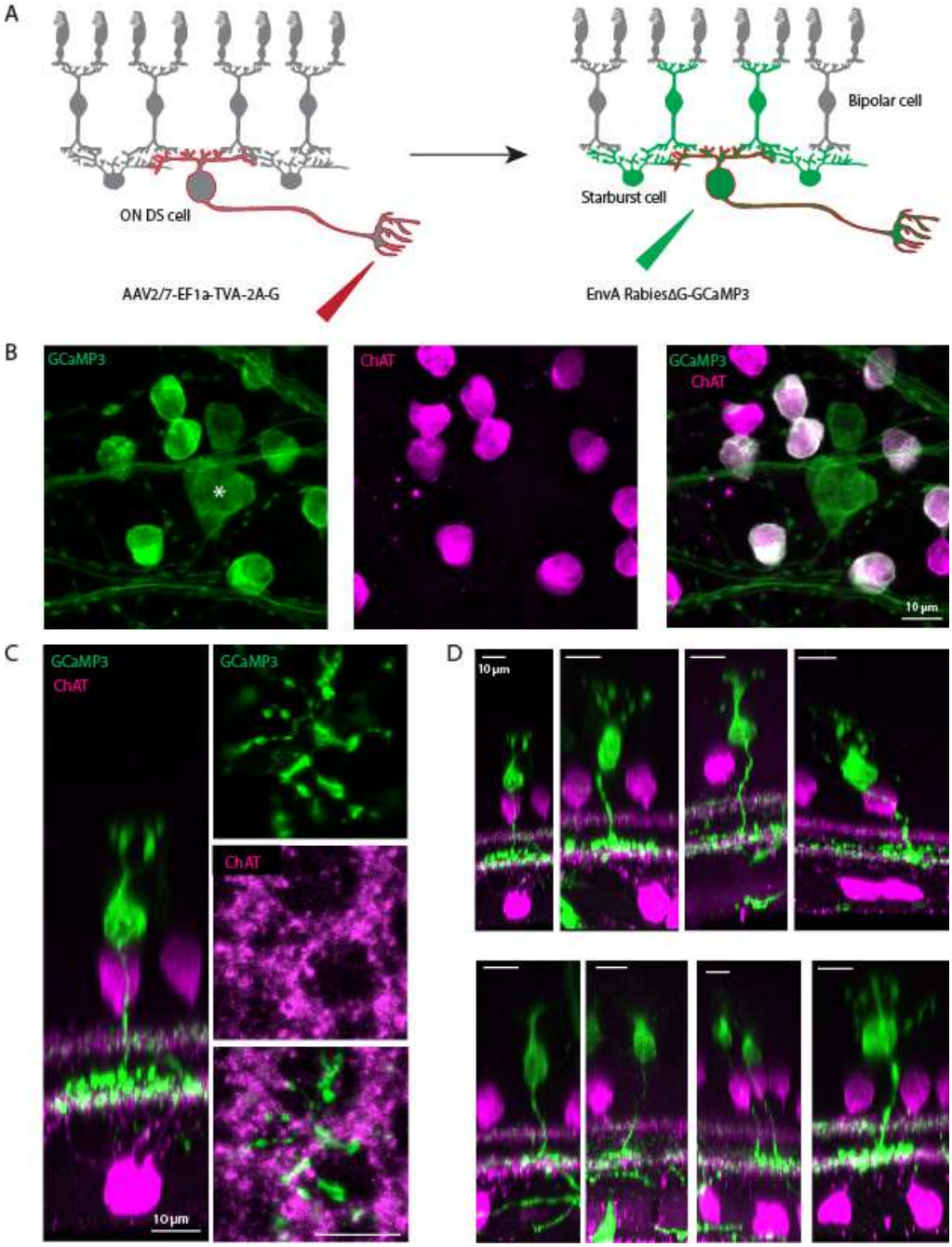

Figure 4-2. *Type-5 Bipolar Cells Are Connected to ON DS Cells (**A**) Schematics of the viral tracing approach used to label ON DS cells as well as their presynaptic bipolar cells and starburst amacrine cells. (**B**) Confocal images of a retina in which an ON DS cell (*) and starburst amacrine cells (magenta) are infected with G-deleted rabies virus expressing GCaMP3 (green). (**C**) Side view (left) and top view (right) of an example of a labeled type-5 bipolar cell. The image for the top view was taken at the depth of the proximal ChAT-labeled layer. (**D**) Nine more examples of labeled type-5 bipolar cells.*

Activity at the Axon Terminal of ON DS Cell-Connected Bipolar Cells Is Not Selective for Motion Direction

We used the same combination of rabies and AAV/herpes viruses that we had used for circuit labeling to record calcium responses via GCaMP3 from the axon terminals of labeled bipolar cells. We stimulated retinas with a positive contrast spot moving in eight different directions. We first imaged the cell body of an ON DS cell and made sure that it was direction selective. Next, we imaged calcium responses in the axon terminal endings of connected bipolar cells. Each axon terminal button of a connected bipolar cell was visible under the two-photon microscope (**Figure 4-3 A**). Based on their appearance (large buttons), we could differentiate them from ON DS dendrites and starburst processes. To further ensure the subcellular and cellular identity of each recorded compartment, we obtained a two-photon image stack at the end of each recording session, fixed the retina, performed immunohistochemistry to label GCaMP3 and starburst cells, and reconstructed the labeled ON DS circuit using 3D confocal imaging. We then aligned the confocal and two-photon image stacks and determined whether the recorded compartments were axon terminals of bipolar cells, processes of starburst cells, or dendrites of ON DS cells **Figure 4-3 A and B**). Starburst processes could be identified because they were double-positive for GFP and ChAT. Strikingly, we found that none of the axon terminals of the 17 type-5 bipolar cells that belonged to the local circuit of nine ON DS cells that were recorded were direction selective: they responded in a similar way to all directions (**Figure 4-3 C-J**). The lack of direction selectivity was not only observed in averaged signals (three repetitions) but also in individual responses and we did not find response failures. The response vector of bipolar terminals pointed in random directions, neither aligned with the preferred direction of the connected ON DS cell nor with any other cardinal directions (Figures 3H and 3I). Some type-5 bipolar terminals provide synaptic input to ON DS cells, while others may drive different ganglion cell types; however, we found no direction-selective activity even when the analysis was restricted to those bipolar terminals that were positioned next to ON DS cell dendrites (**Figure 4-3 E-G**), suggesting that activity in all identified type-5 bipolar cell terminals are direction nonselective.

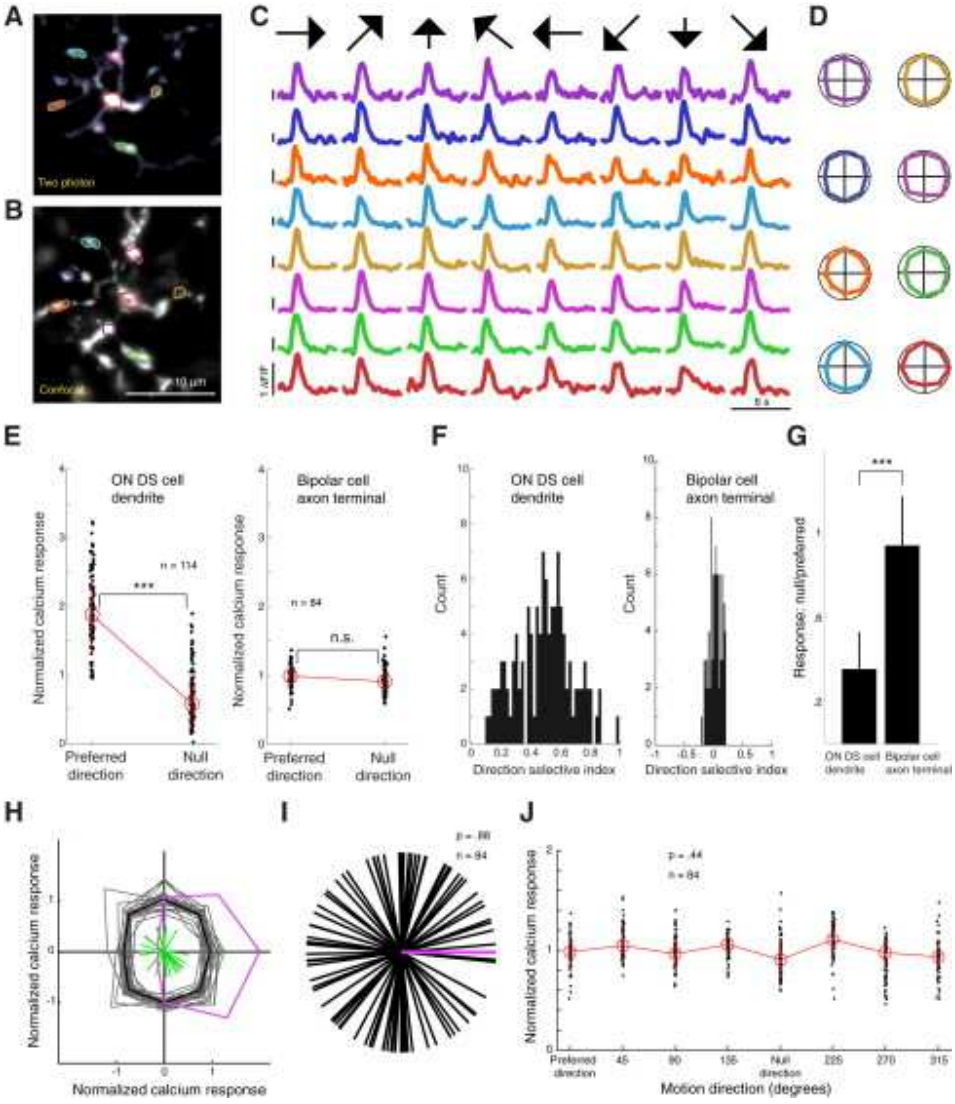

Figure 4-3. *Activity at the Axon Terminal of ON DS Cell-Connected Bipolar Cells Is Not Selective for Motion Direction* ***(A)*** *Top view of two-photon image of bipolar cell axon terminal labeled with GCaMP3 expressed from transsynaptic rabies virus initiated from an ON DS cell. Regions of interest are marked by colored lines.* ***(B)*** *Confocal picture of the same region as in* ***(A)****.* ***(C)*** *Calcium transients recorded by two-photon imaging in response to stimuli moving in eight different directions. Colors of the traces indicate locations of the recorded compartments in* ***(A)*** *and* ***(B)****.* ***(D)*** *Polar plots of peak responses to each direction of motion. Colors of the plots indicate the recorded compartments marked in* ***(A)*** *and* ***(B)****.* ***(E)*** *Normalized ([DF/F]/mean[DF/F]) calcium responses of ON DS cell dendritic or bipolar cell axon terminal compartments in the preferred and null directions. The response of each recorded compartment is shown as a small dot. Large open dot and red vertical line represent the mean and ±SD, respectively. The preferred/null directions for the bipolar terminals refer to the preferred/null directions of the monosynaptically connected ON DS cell.* ***(F)*** *Histograms of the direction-selective index of ON DS cell dendritic (left) and bipolar cell axon terminal (right) compartments.* ***(G)*** *The ratio of the null*

*direction response to the preferred direction response for ON DS cell dendrites and bipolar cell axon terminals. Data are represented as mean ± SD. (**H**) Polar plot of normalized calcium responses ([DF/F]/mean[DF/F] of each compartment) of an example ON DS cell body (magenta) and axon terminal compartments of the connected bipolar cells (gray and black) to each direction of motion. Gray plots and a black plot are the responses of each recorded compartment and the mean, respectively. Green bars indicate the direction of the vector sum of the activity of each bipolar terminal compartment within this single circuit. (**I**) The direction of the vector sum of the activity of each bipolar terminal compartment (black) across all recorded bipolar terminals relative to the preferred direction of the monosynaptically connected ON DS cell body (magenta). All preferred directions of ON DS cell bodies were chosen to point in the same direction. (**J**) Normalized ([DF/F]/mean[DF/F] of each compartment) calcium responses of bipolar cell axon terminal compartments in each direction of motion. The response of each recorded compartment is shown as a small dot. Large open dot and red line represent the mean and ±SD, respectively. See also Figure S3.*

Concerted Activity at Subcellular Resolution within the Circuit of a Single ON DS Cell

To simultaneously observe the concerted activity of ON DS-connected bipolar terminals, starburst cell processes, and ON DS dendrites during motion stimulation, we imaged retinal regions around an ON DS cell where all of these three elements were labeled. It was possible to visualize the synaptic compartments of the circuit simultaneously, since these compartments are restricted to one two-photon image plane in the inner plexiform layer of the retina (**Figure 4-4 A and B**). The simultaneous imaging of subcellular compartments clearly showed the different behavior of the three circuit elements: the axon terminals of bipolar cells were not direction selective, the processes of starburst cells showed ‘‘local’’ direction selectivity along the centrifugal axis (*113*), and the dendrites of ON DS cells were all ‘‘globally’’ direction selective along the same axis (**Figure 4-4 C and D**).

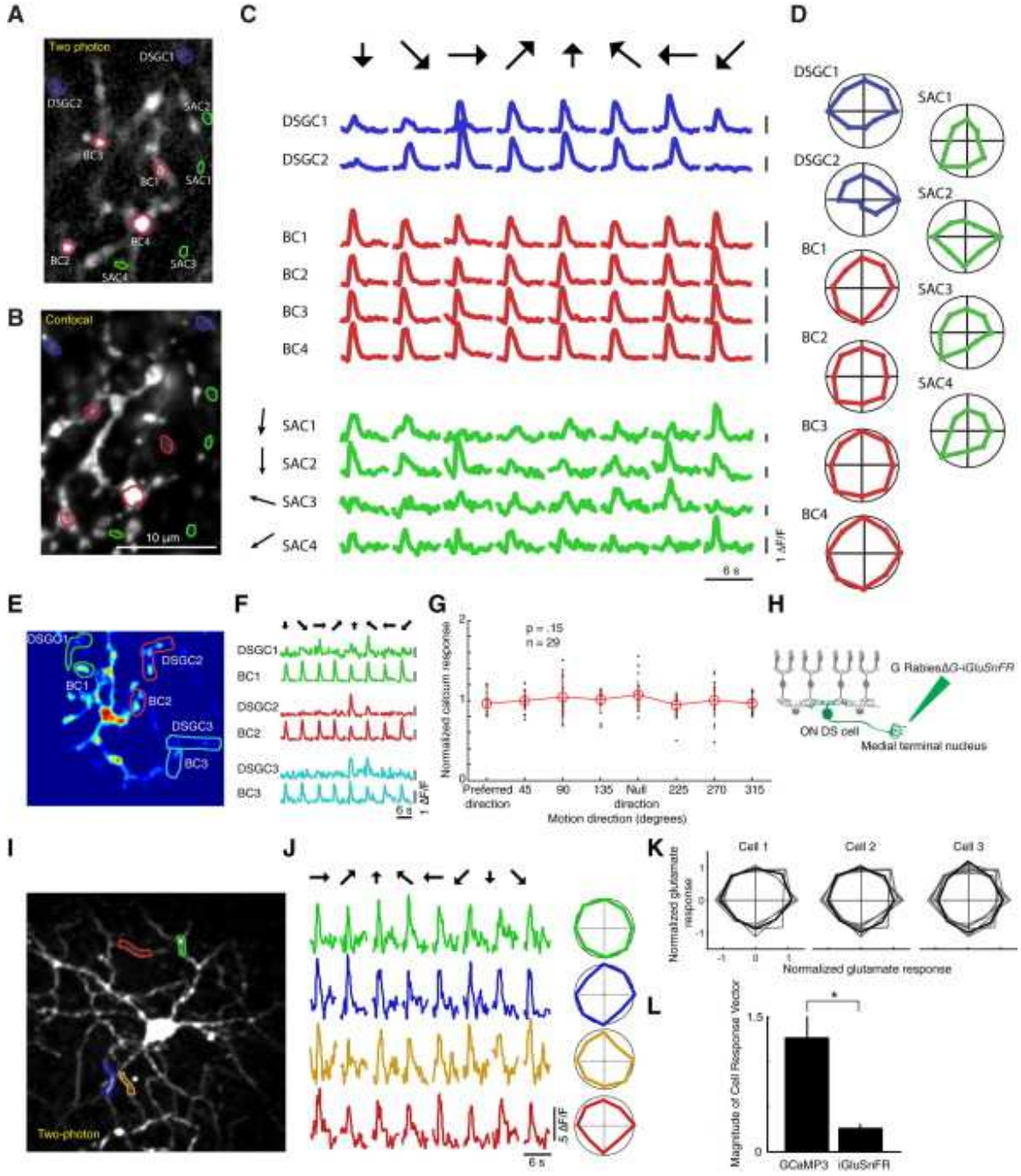

Figure 4-4. *Concerted Activity at Subcellular Resolution within the Circuit of a Single ON DS Cell and Glutamate Input onto Dendrites of ON DS Cells (**A**) Top view of two-photon image of bipolar cell axon terminal, starburst cell process, and ON DS cell dendrite labeled with GCaMP3 expressed from transsynaptic rabies virus initiated from an ON DS cell. Regions of interest are marked by colored lines. BC, bipolar cell; SAC, starburst amacrine cell; DSGC, ON DS cell. (**B**) Confocal picture of the same region as in (**A**). (**C**) Calcium transients in ON DS cell dendrites (blue), bipolar cell axon terminals (red), and starburst cell processes (green) recorded by two-photon imaging in response to stimuli moving in eight different directions. Labels to the left of traces indicate*

*locations of the recorded compartments in (**A**). The centrifugal directions of starburst cell processes are indicated by arrows at the left side. (**D**) Polar plots of peak responses to each direction of motion. (**E**) Two-photon image (top view) of GCaMP3-expressing bipolar cell axon terminals and ON DS cell dendrites shown as a heat map. Regions of interest are marked by colored lines. BC, bipolar cell; DSGC, ON DS cell. (**F**) Calcium transients recorded by two-photon imaging in response to stimuli moving in eight different directions. Colors of the traces indicate locations of the recorded compartments in (**E**). (G) Normalized ([DF/F]/mean[DF/F] of each compartment) calcium responses of those bipolar cell axon terminals that were juxtapositioned to monosynaptically connected ON DS cell dendrites. The response of each recorded compartment is shown as a small dot. Large open dot and red line represent the mean and ±SD, respectively. (H) ON DS cells were targeted by iGluSnFR-expressing, G-coated G-deleted rabies virus, which was injected to the medial terminal nucleus. (**I**) Maximum image projection of two photon image of the same ON DS cell. Regions of interest are marked by colored lines. (**J**) Two-photon imaging of glutamate input signals onto the four color-marked dendritic segments of the ON DS cell shown in (**I**), in response to stimuli moving in eight different directions. Colors of the traces indicate locations of the recorded compartments in (**I**). Polar plots of the peak responses are shown on the right. (**K**) Polar plot of normalized glutamate signals ([DF/F]/ mean[DF/F] of each compartment) in the dendrites of three different ON DS cells to each direction of motion. Gray plots and a black plot are the signals of each recorded dendritic compartment and the mean, respectively. (**L**) Comparing the magnitude of cell response vectors in calcium and glutamate recordings in ON DS cells. Data are represented as mean ± SD.*

Glutamate Signaling at ON DS Cell Dendrites Is Not Direction Selective

Neurotransmission from bipolar cells to ganglion cells is mediated by glutamate. To directly test whether the glutamate input signal to ON DS cells is direction selective or not, we developed a G-deleted rabies virus expressing a glutamate sensor iGluSnFR (*114*, *116*) and injected it into the medial terminal nucleus (**Figure 4-4 H**). Similar to GCaMP3-marked ganglion cells, most dendritic segments of iGluSnFR-marked ganglion cells were stratified at the proximal ChAT-labeled layer (*84*, *90*) suggesting successful targeting of ON DS cells. We stimulated isolated retinas with a positive contrast spot moving in eight different directions and performed two-photon imaging of iGluSnFR-labeled ganglion cells. The dendritic segments of five recorded ON DS cells did not have direction-selective iGluSnFR signals (**Figure 4-4 I-L**). These experiments suggested that the glutamate input signal to the dendrites of ON DS cells is not direction selective.

Discussion

The key finding of this work is that direction-selective activity is absent both in the Ca signals measured at axon terminals of those specific bipolar cells, type-5, that connect to ON DS cells, as well as in the glutamate signals around the dendrites of ON DS cells. In contrast, the visually evoked Ca signals of the dendritic segments of ON DS cells are direction selective.

Mechanism of Direction Selectivity

Direction-selective computation in the retina, discovered in 1963 (*117*) served for a long time as a model circuit to explain how a specific neuronal computation is implemented by neuronal hardware. It has been proposed that the key components of this computation are the centrifugal direction selectivity in starburst cells and the asymmetric connectivity between starburst and DS cells, as well as those bipolar cell axon terminals that provide input to DS cells. An increase in direction selectivity also occurs within ganglion cells, after the combination of inhibition and excitation, by the action of active conductances(*105*, *118*). In addition, in the case of the upward-motion-sensitive ON-OFF DS cell, the shape of the cell plays an important role in contributing to direction selectivity at slower speeds (*119*). There is direct proof of the centrifugal direction selectivity of starburst cells (*81*, *82*) and the asymmetric connectivity between starburst and ON-OFF DS cells (*87*, *101–103*), as well as ON DS cells (*104*). Asymmetric connectivity between starburst cells and bipolar cell axon terminals was inferred from indirect evidence, electrophysiological recordings from ganglion cell bodies (*80*, *87*). Our results, demonstrating the lack of direction selectivity in the Ca signals at bipolar cell axon terminals as well as the glutamate signals around ON DS cell dendrites, suggest that there is no spatially asymmetric connectivity to bipolar terminals and that the electrophysiological results probably reflect space-clamp problems at the synaptic sites(*45*, *106*). We found that direction selectivity in the cardinal directions is first achieved at the third (and last) neuron of the retina's excitatory neuronal chain. In the rabbit retina, some of the dendritic segments of ON DS cells run together in tight fascicles (*120*). If the dendrites of ON DS cells are arranged similarly in mice, an alternative explanation for the lack of direction-selective glutamate signals in ON DS ganglion cells could be that glutamate spills over from the bipolar-to-ganglion cell synapse(*121*, *122*), activating extrasynaptically expressed iGluSnFR in the cofasciculating dendrites. If these

dendrites had different preferred directions, despite a potentially direction-selective glutamate signal in the synapse, motion in various directions would activate iGluSnFR on the same dendrite. Therefore, the recorded signal would appear direction nonselective. This explanation is, however, unlikely for the following two reasons. First, it was shown previously that glutamate transmission from mouse ON bipolar cells is mostly confined to the synapse. This is achieved by presynaptic inhibition to bipolar cell axon terminals through GABA C receptors, which limits the spillover of glutamate from the synapse to perisynaptic regions (*122*). In addition, evidence supporting the lack of extrasynaptic glutamate contributing to iGluSnFR signals in ganglion cells during light stimulation has also been recently provided, by showing that at the border between the termination of ON and OFF bipolar axon terminals, iGluSnFR-expressing ganglion cell dendrites do not report mixed ON and OFF signals (*116*). Second, only a fraction of the dendrites of rabbit ON DS cells run together (*120*). Therefore, even if the glutamate signal in the synapse were direction selective and if glutamate spill over would blur the iGluSnFR signals across cofasciculating dendrites, some dendritic segments would still show direction selective responses. We found iGluSnFR signals to be direction nonselective in every dendritic segment analyzed.

The Concerted Activity of Circuit Elements at Subcellular Resolution

Recent advances in monosynaptic viral tracing have opened up the possibility to follow the activity of many neurons belonging to the same circuit (*110*). Here, we used GCaMP3-functionalized viral tracing and two-photon imaging to record the activity of the circuit elements of single DS cells at subcellular resolution while these circuit elements were computing a specific task. We were able to image the different synaptic compartments of the circuit simultaneously because these compartments are arranged on a horizontal plane, within a layer in the inner plexiform layer of the retina. We then combined information from recordings with the Ca sensor GCaMP3 in both the presynaptic axon terminals and in the postsynaptic dendrites together with recordings using the glutamate sensor iGluSnFR in the postsynaptic dendrites to define the specific subcellular compartment, in this case the postsynaptic dendrite, at which a particular computation occurs. The recording of synaptic activity at three consecutive levels, Ca signals in axon terminals, glutamate input signals at

dendrites, and Ca signals in dendrites, within an identified circuit can not only reveal the computation logic of a neuronal circuit but could also be used to study the molecular logic of circuit assembly from specific cell-type components or to investigate genetic diseases that lead to synaptic dysfunction.

Unanswered Questions

A number of unanswered questions regarding computations by DS cell circuits in the retina remain. First, why are ON-OFF DS cells optimally stimulated with motion at higher speeds than ON DS cells (*123*)? Our finding that ON DS cells are specifically connected by type-5 bipolar cells, one of the three bipolar cell types that could provide synaptic input based on proximity, and another finding that type-7 cells connect to ON-OFF DS cells (*124*) either inclusively or exclusively, point to the bipolar cell input as one potential component of speed selectivity. Second, what are the roles of those amacrine cells (*125*, *126*) that influence the DS circuit but are not necessary for direction selectivity? Third, so far most retinal studies, including this study, have focused on spatial asymmetries between inhibitory and excitatory circuit elements or on the centrifugal asymmetry within starburst cells as the explanation for direction selectivity. However, time delays among excitatory circuit elements, such as bipolar cells, could also contribute to direction selectivity (Reichardt-model), as it is predicted in insects (*127*). Future experiments with faster Ca sensors could address the question of whether type-5 cells are engaged in a Reichardt-model-like activation pattern and, thereby, enhance direction selectivity in DS cells. Time delays between the bipolar cells that provide input to starburst cells could also confer centrifugal direction selectivity upon the processes of starburst cells. There are also unanswered questions regarding the message that DS cells send to the higher visual centers. How do the higher centers interpret the spiking pattern of DS cells? DS cells vary in their activity depending on the direction, speed, and contrast of the motion stimuli. How does the brain sort out these stimulus parameters, especially during natural vision, based on the spikes it receives from a single or multiple DS cells? New technologies combining genetic and transsynaptic labeling, together with optical or electrical readout of activity from the different circuit elements, will probably allow researchers in the field to approach these questions.

Chapter 5 - Deciphering cortical and subcortical pathways of non-image forming vision

***Balint K**, Hilier D, Raics Z, Yonehara K, Hantz P, Delogu A, Roska B.*

Introduction

Sensory information gathered from the intrinsic and extrinsic environment of our body splits into two major computational directions in an anatomically characteristic manner. On one hand sensory information is carried to the cortex and turned into a conscious perception allowing a controlled decision making, while other afferents stay subcortical and computed autonomously. The cortical and subcortical pathways of a sensory modality can share some elements or form separated circuits. Information carried by light to our retina is transmitted to both cortical and subcortical locations (*34*). It is generally accepted that the cortical pathway of photoreception leads to image forming vision, while the non-image forming functions stay subcortical. Several studies demonstrated that cone and rod photoreceptors serve both image-forming and non-image forming vision but they are separated in the inner retina, where intrinsically photosensitive retinal ganglion cells (ipRGCs) become the sole conduits of non-image forming vision such as the circadian light entrainment and pupillary reflex (*35*, *128*). IpRGC circuits carry the integrated response of cone, rod and melanopsin to different subcortical brain nuclei (*40*, *53*, *129*). It is unknown, how much if any of the ipRGC signaling is channeled into the image forming vision, however in the last decade a number of findings indicated this possibility(*39*, *40*, *130*). In addition, ipRGCs form multiple subtypes (M1-M5) based on their morphological and physiological characteristics (*131*). In this study we are addressing two basic questions: (i) does the signal from ipRGCs reach the visual cortex and (ii) do all ipRGC subtypes participate in subcortical non-image forming circuits? We are investigating the cortical connections via recording visual activity in the primary visual cortex of mice lacking the function of cones and rods. The subcortical connections of the distinct ipRGC subtypes are addressed by

monosynaptic retrograde tracing from different subcortical centers of the circadian system to the retina.

Results and Discussion

The visual cortex receives signals from ipRGCs

Rd1 mice missing cone and rod photoperception and therefore used to study melanopsin driven functions in isolation from the other photopigments (*39*, *132*). First, we examined if any light induced neuronal activity can be detected in the visual cortex of rd1 mice. The left visual cortex was injected with adeno-associated virus (AAV) encoding the calcium sensor GCaMP6s. We recorded the neuronal activity with 2-photon calcium imaging while the right eye of the mouse was illuminated with 5s, 100 µW intensity, 480 nm light flashes interrupted with 30 s dark periods (**Figure 5-1 A, B**). Light elicited sluggish fluorescence increase in the cell bodies and dendrites in all depth recorded from the surface (**Figure 5-1 C**). Since rd1 mice are physiologically not intact and the long time required for photoreceptor loss gives time for cortical plasticity we aimed to test the presence of ipRGC activity in the cortex of wild type mice. In order to do so we injected glutamatergic blockers into the eye before stimulation. The combination of APB, CPP and NBQX is used broadly in retina research to block the transmission from the photoreceptors to the ganglion cells (*133*–*136*). Since the limited time of the drug effect, here we used accusto-optical random-access 3D microscopy which allow us to record hundreds of neurons in a three dimensional space at the same time (*19*, *137*). We compared the cortical responses in wild type mice with and without the blockers and in rd1 mice. (**Figure 5-1 E, F**). We accepted cells as light responsive if the signal-to-noise ratio of the fluorescence increase after the light stimulation was larger than 3. For instance, in rd1 mice more than 900 cells fulfilled this criterion (**Figure 5-1 D),** which is 31% of all recorded neurons (**Figure 5-1 F)**. This ratio was larger in wild type animals at control conditions and smaller when blockers were applied, 45% and 7% respectively (**Figure 5-1 F)**. Not only the number of responding cells decreased dramatically after the blockers were applied, but the characteristics of the responses changed as well. At control condition the onset of the response is quicker (**Figure 5-1 G**) and

has an ON-OFF characteristic (**Figure 5-1 H**), while at blocker conditions the slow onset and the ON-only responses are characteristic, however some cells produce OFF activation as well, which we will discuss in the next section (**Figure 5-2 A**). In rd1 mice the onset of the response is quicker and no OFF response can be detected. These findings altogether indicate that ipRGC signaling reaches the visual cortex through excitatory pathways. The increased sensitivity in rd1 mice can be explained by the fact that melanopsin expression is increased in rd1 mice. Since the melanopsin is not expressed ectopically it is likely that the elevated melanopsin level in the low melanopsin content ipRGCs (M2, M4 and M5) has a primary contribution in generating the cortical hypersensitivity. In order to clarify the role of M1 ipRGCs possessing the highest sensitivity in wild type animals, we recorded calcium signals from wild type mice at one magnitude lower, 10 μW strong stimulating light. This intensity is strong enough to excite M1 ipRGCs, but we could not detect any signal at blocker condition and the plateau-like component disappeared at the control condition (**Figure 5-1 H).** This indicates that the cortical melanopsin signal can originate from any ipRGCs but M1 cells.

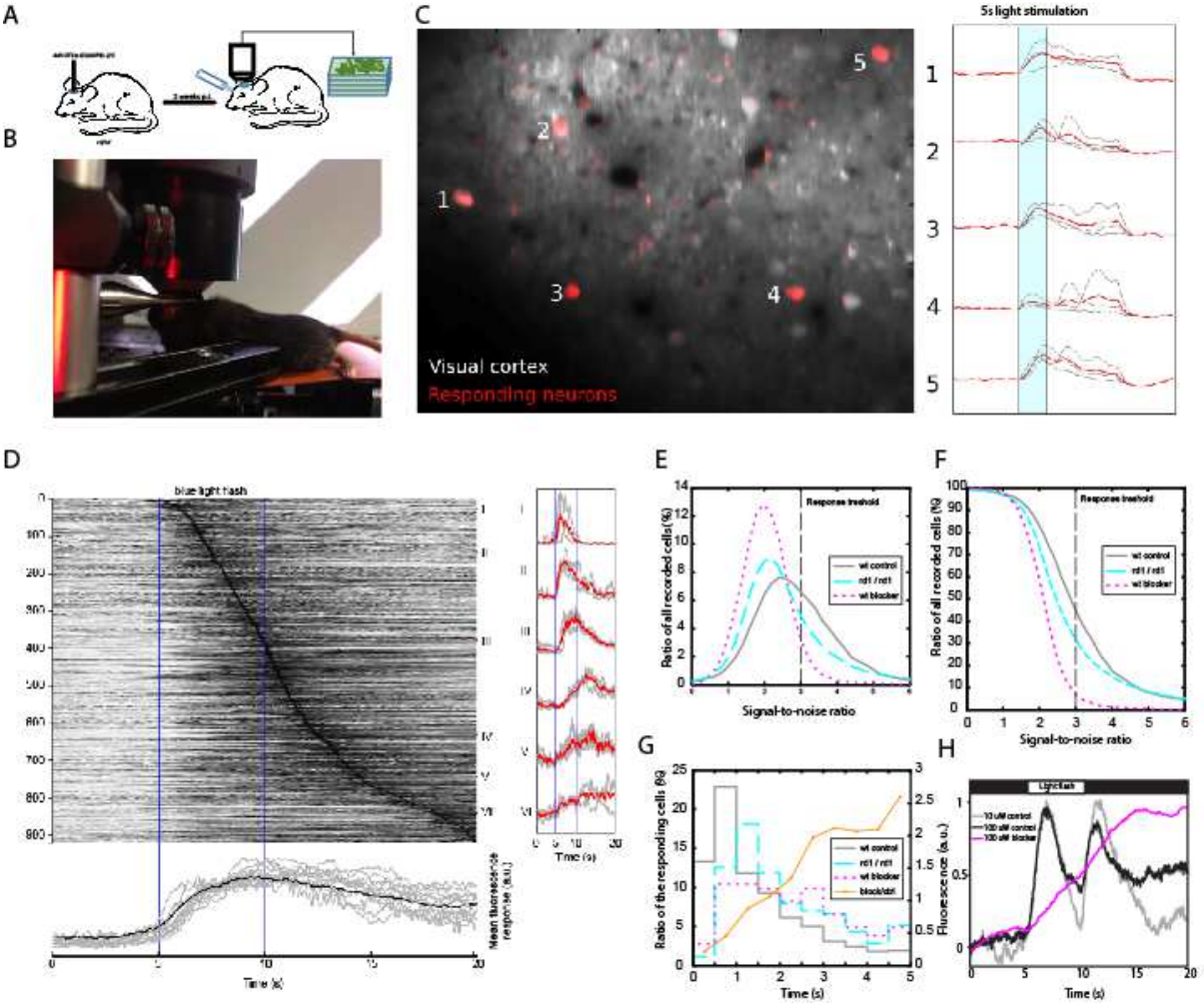

Figure 5-1. Cortical signals driven by ipRGCs. ***(A)****, Experimental layout: mice are injected with AAV expressing GCaMP6s and chronic window is prepared. Two weeks later the in vivo calcium imaging performed while stimulating the eye with a blue LED.* ***(B)*** *Picture about the head fixed animal while recording cortical calcium signals elicited by moving bar stimulus.* ***(C)*** *Calcium imaging from GCaMP6 expressing cortical plane in rd1 mouse. Grey image shows GCaMP labeled brain, red labels are the light responsive active zones identified by automatic analysis. Graphs on the right represent the fluorescence change over time in the corresponding cell bodies labeled by numbers.* ***(D)*** *The image shows all responding cells recorded in rd1 mice with accustom-optical 3D microscopy. Each vertical line represents a single cell, which are ordered by the delay of the peak amplitude from light on. Blue lines indicate the light on and light off. Below the image the average fluorescence change of all experiment (black) and from individual animals (grey) is shown. On the right, graphs are examples of individual neurons. Numbers indicting their location in the entire cell pool* ***(E)*** *Histogram and (F) cumulative histogram shows the distribution of signal-to -noise ratio of all recorded cells at control (grey), blocker conditions (magenta) and in rd1 mice (cyan).* ***(G)*** *Normalized histogram shows the distribution of the onsets of the responses after the stimulating light is turned on. Control (grey), blocker (magenta), rd1 (cyan). Yellow plot shows the ratio between the blocker and control histograms.* ***(H)*** *The averaged response of the responding cells at blocker and control conditions stimulating with either 10µW or 100µW intensity light.*

Blocker sensitive OFF response in the visual cortex is originated from OFF ganglion cells with non-conventional presynaptic retinal circuits

The intrinsic response of the ipRGCs has ON characteristics. Yet, we measured OFF responses in the visual cortex, when all neurotransmission was blocked between the photoreceptor layer and the ganglion cell layer by injecting a cocktail of APB, NBQX, CPP into the eye (**Figure 5-2 A**). This cocktail has been used in a number of studies to separate ganglion cells from their presynaptic excitatory inputs but in those experiments the ex vivo retinal implants were perfused with Ringer solution containing the blockers (*133–136*), while our approach used a bulk injection of drug cocktail into the eye. Although we have used fifty times higher concentration (500µM) than others in their ex vivo experiments, it is still possible that the residual OFF activity is a result of insufficient penetration or rapid dilution and wash out of the drugs. Other possibility is that some OFF ganglion cells in the retina are resistant against the classical blocking cocktail. In order to clarify this, we placed the retina of wild type mice on multi electrode array and we recorded action potentials in the presence of the blockers at light on and light off (**Figure 5-2 B**). This way we were able to record in a high throughput manner from hundreds of ganglion cells at the same time. Surprisingly, we found that some OFF cells could not be silenced by the blockers (18/250). The low number and uniform characteristics of the blocker resistant responses indicated that they are originated from a single cell type. There are only few transgenic mouse lines in which OFF ganglion cells are labeled specifically and most of these genetically identified cells has been extensively studied and they sensitivity against the glutamate blockers was confirmed(*31*). We found however that in the Opn3-GFP BAC transgenic mouse line the retinal GFP expression localized mainly in two cell types: the M2 ipRGCs and an unknown monostratified ganglion cell arborizing deeply in the OFF part of the inner plexiform layer (**Figure 5-2 C, D**). The Opn3 gene encodes the protein encephalopsin and therefore we called these cells E1 cells, even though encephalopsin could not be detected in these ganglion cells by immunohistochemistry. We used two photon targeted loose cell patch recording to characterize the response of E1 cells to light on and light off, at control conditions and in the presence of the glutamatergic blockers. At control conditions, we found that E1 cells produce strong burst of firing at light off but the spiking is silenced by turning the light on

(**Figure 5-2 E**). When blockers applied the ON suppression completely disappears as expected, but the OFF excitation remains prominent despite the significantly lower frequency (**Figure 5-2 F**). This is very similar to the phenomenon we observed with multielectrode array and it can explain the origin of the residual OFF activity in the visual cortexat blocker condition. To date, the only known blocker resistant light response is the ON response generated by melanopsin in the ipRGCs and therefore our finding indicated the possibility of a novel type of ipRGC producing an intrinsic OFF response due to the expression of an unidentified photopigment. This was further supported by the fact, that the cells are identified by the promoter of the encephalopsin, which is principally able to participate in light detection similarly to other opsins(*138*). Alternatively, the E1 cells might excited by the cones and/or rods through a non-conventional inner retinal pathway.

To clarify this, we performed three distinct tests. First we recorded action potentials and intracellular currents from E1 cells in the presence of cobalt-2-chloride. Cobalt interferes with calcium mediated processes including the neurotransmitter release and therefore stops all transmission through chemical synapsis. It is unable though to eliminate the melanopsin induced intrinsic activation(*139*). We found that cobalt eliminated both action potential firing and intracellular excitatory currents in the E1 cells (**Figure 5-2 F**). This can indicate, that the E1 cells are activated through synapses or that the intrinsic photopigment activates the E1 cells through a cobalt sensitive pathway, different than the one used by melanopsin. Therefore we measured the spectral sensitivity of the E1 cells during glutamatergic blockade. The four known functional pigment in the mouse retina have different spectral sensitivity. The peak sensitivity of the 4 opsins are as follows: S-opsin 360nm, L-opsin 510 nm, rhodopsin 500 nm, melanopsin 470 nm. Furthermore the distribution of the cone opsins are not homogenous in the retina along the dorso-ventral axis. The ventral part is dominated by UV-cones expressing S-opsin, while the dorsal part by green cones, expressing L-opsin (*140*). The peak sensitivity of the E1 cells located in the ventral retina were shifted towards the peak sensitivity of the UV cones (**Figure 5-2 G**), while E1 cells in the dorsal part had a peak sensitivity similar to green cones (**Figure 5-2 H**). This was equally valid for the responsiveness to both on and off stimuli at control conditions as well as the off response in the presence of glutamatergic blockers. This indicates

that the E1 cells are activated by S- and L-cones which are likely expressed in the cones and not in the E1 cells. This later was proven by layer specific 2-photon laser stimulation of the retina. When recording from a normal ganglion cell, the most robust response can be measured while the 2-photon laser is focused on the photoreceptor layer. In contrary, M2 ipRGCs in the presence of glutamate blockers can be excited the most when stimulating the ganglion cell layer and the inner plexiform layer. E1 cells showed identical layer sensitivity to control ganglion cells and not to M2 ipRGCs (**Figure 5-2 I**), suggesting that the photopigments driving the blocker sensitive off responses in the E1 cells, are located in the photoreceptor layer. These data together indicates that the residual off responses in the visual cortex are the result of the activation of E1 cells from conventional photoreceptors through a non-conventional inner retinal pathway. Deciphering the components of this novel pathway would require further experiments.

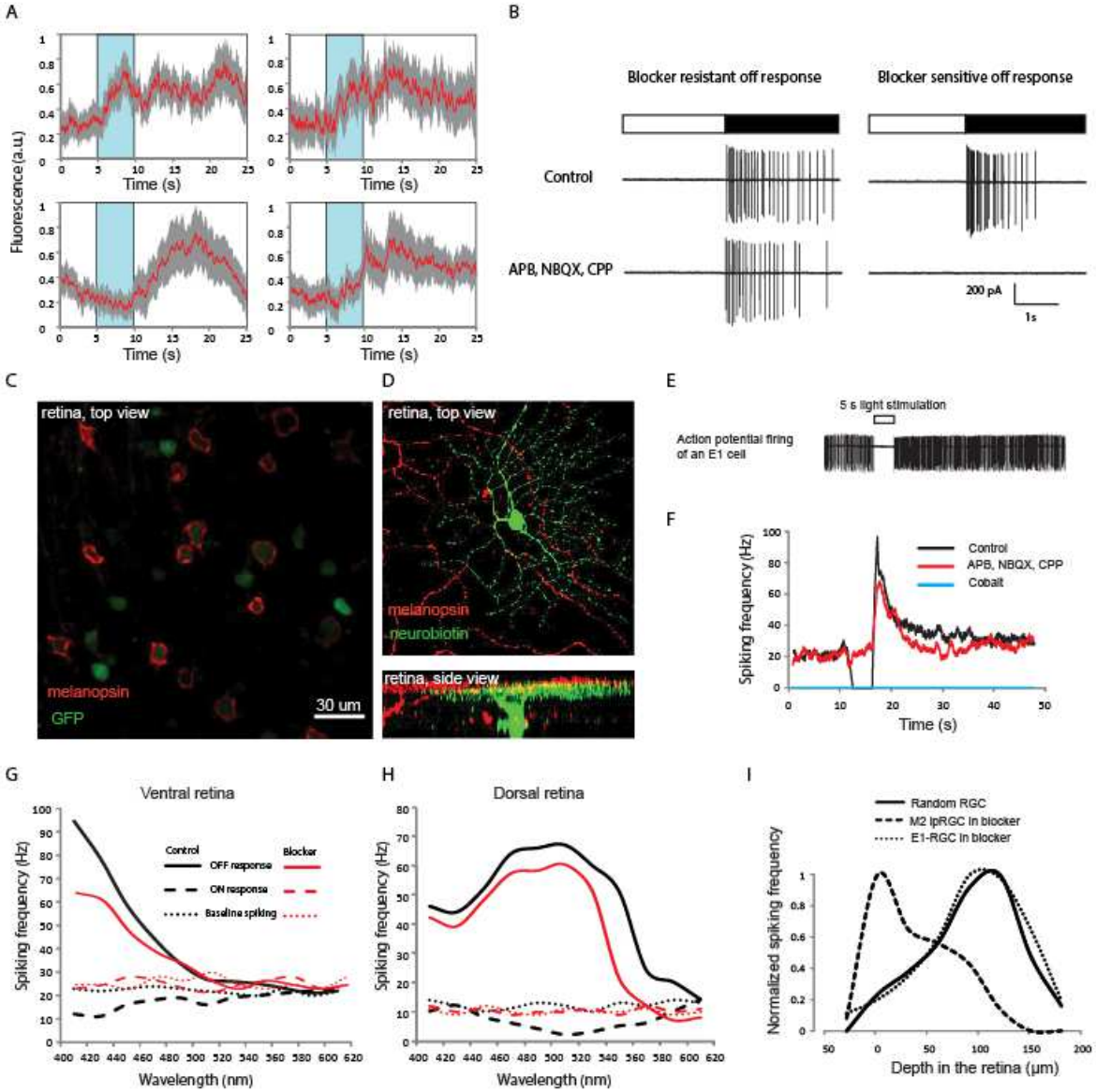

Figure 5-2. Blocker resistant off responses in the cortex and retina *(A) Example traces from cortical recordings where residual off responses can be detected. (B) Examples of blocker resistant and blocker sensitive OFF responses of retinal ganglion cells recorded with multielectrode array. (C) Images show the Opn3-GFP retina from top view after staining against melanopsin. (D) Top and side view of a melanopsin negative, GFP labeled OFF cell after filled with neurobiotin. (E) Example spiking trace from an E1 neuron. (F) Effect of glutamatergic blockers (red) and cobalt (blue) on the spiking frequency of the E1 cell. (G) Spiking frequencies as function of stimulation wavelength in the ventral retina at control and blocker conditions. (H) Spiking frequencies as function of stimulation wavelength in the dorsal retina at control and blocker conditions. (I) Normalized spiking frequency of M2 ipRGCs, E1 cells and control retinal ganglion cells in the function of the depth where the stimulating laser focused.*

All type of ipRGCs participate in subcortical visual circuits

We have shown here that some ipRGCs project to the cortex with the exception of M1 ipRGCs. It has been shown by others, that M1, M2 and M3 ipRGCs can be traced back with classical tracers from non-image forming centers such as the SCN and OPN (*55*). As I have shown in Chapetr 1 and 2, these ipRGCs can be detected in the retina with multisynaptic tracing through the pupillary reflex pathway as well, therefore the role of the three subtypes in non-image forming vision is relatively well founded. In contrary, there is no indication other than their intrinsic photosensitivity, that M4 and M5 ipRGCs participate in non-image forming functions as well. They might be dedicated entirely for image forming vision. To assess this question we performed monosynaptic retrograde tracing from various centers of the circadian regulation through the intergeniculate leaflet (IGL) and analyzed the back-traced ganglion cells in the retina. We have chosen the IGL because it is a known target of ipRGCs (*129*) and it consist long projecting inhibitory neurons targeting most of the known locations related to circadian regulation (*141*). In order to initiate the tracing from the long projecting inhibitory neurons of the IGL we took advantage of the Sox14-Cre mouse line (unpublished) which expresses Cre-recombinase in in the inhibitory neurons of the subcortical visual shell, including the long projecting inhibitory neurons of the IGL.

First we tested if the long projecting inhibitory neurons are targeted directly by retinal ganglion cells. The left IGL of Sox14 mice was injected with a mixture of adeno-associated viruses (AAVs) expressing the TVA, rabies G and NLS-tdTomato from the elongation factor 1α (EF1α) promoter in Cre-conditional manner. In order to keep the AAV infection localized we used the only-anterograde AAV serotype 2/1 which does not allow retrograde gene delivery to other nuclei. This was necessary because the Cre-recombinase is expressed in multiple nuclei of the subcortical visual shell which send efferent to the IGL. Since the Cre-expression is temporally limited to the first three postnatal weeks, the first injections were performed at postnatal day 7 (P7). This was followed by an injection of GFP expressing, Envelope-A (EnvA) coated, monosynaptically restricted rabies virus into different target regions of the IGL, such as the suprachiasmatic nucleus (SCN), periaqueductal grey matter (PAG) and the contralateral IGL (**Figure 5-3 A**). Seven days after the rabies injection the animals were dissected and tested for

viral labeling. We verified that the starter cells co-labeled by GFP and Tomato were localized in the IGL exclusively (**Figure 5-3 B**). In the retina we found GFP labeled ganglion cells dominantly in the ipsilateral retina (**Figure 5-3 C**). We found at least one ganglion cell in 11 of the 15 injected animals: three SCN, five PAG and four IGL injected animals had positive retina with 13±8, 45±27, 93±35 ganglion cells respectively. This indicates that long projecting inhibitory neurons of the IGL are directly targeted by retinal ganglion cells.

In order to identify the ganglion cells we stained the retinas with antibody against melanopsin and choline acetyltransferase (ChAT), and with the nuclear marker DAPI (**Figure 5-3 D, E**). We found that almost half of the ganglion cells which has been tested from all experiments were ipRGCs (194/425). Surprisingly, a significant number of DS cells were labeled when the rabies was injected into the PAG (64/425) or the contralateral IGL (95/425). In contrary, the SCN injection resulted pure ipRGC population. Regarding the ipRGC subtypes we found that injections into the IGL resulted a mix population of M2, M3, M4 and M5 ipRGCs dominated by M2 and M3 ipRGCs (92%) and no M1 ipRGC was detected. PAG injections led to similar results, but here the M4 and M5 cells showed clear dominance over M2 and M3 cells (87%). Interestingly, the labeled ipRGCs in the SCN injected animals were all M2 cells (**Figure 5-3 G**).

These data indicates that all type of ipRGCs play a role in the subcortical vision and they act on different circadian centers. This allow us to drop the hypothesis about ipRGC subtypes dedicated solely to image forming vision. The massive projection of the M4 and M5 cells to PAG via inhibitory long projecting IGL neurons, indicates their role in silencing the arousal system. The specific labeling of the M2 cells back-traced from the long projecting inhibitory neurons innervating the SCN suggest that M1 and M2 cells work in an antagonistic way, since the M1 cells are the primary retinal input to the SCN(*55*). It is interesting that DS cells showed up in such a great number. It is possible that IGL or the neighboring ventral geniculate nucleus integrates ipRGC and DS cell inputs. Seemingly, optokinetic reflexes guided by DS cells and circadian rhythm modulated by the ipRGCs fall very far from each other but maybe we have just made the first step towards understanding the role of rapid eye movements during sleeping.

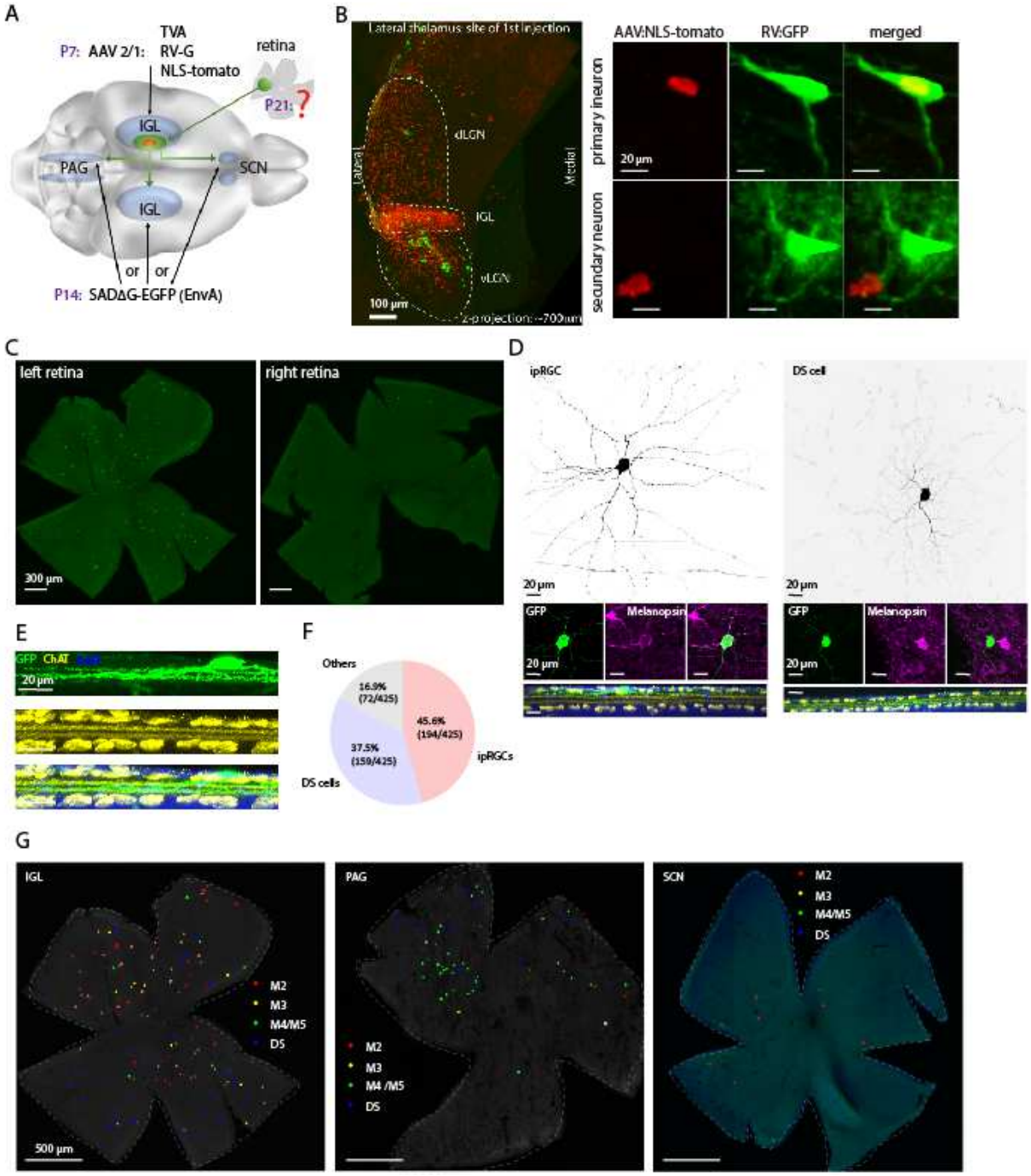

Figure 5-3. Monosynaptic tracing of retinal ganglion cells from long projecting inhibitory neurons in the thalamus. ***(A)*** *Schematic of the tracing experiment: AAVs expressing TVA, rabies G, NLS-tdTomato are injected into the IGL of Sox14 mice at P7. At P14 EnvA coated rabies virus expressing the EGFPis injected into the contralateral IGL or ipsilateral PAG or SCN. At P21 the retinas are tested for GFP expression.* ***(B)*** *Image shows the lateral geniculate nucleus after rabies tracing. Red labeling correspond to the Cre-expressing cells, green cells to the virus labeled cells (right). Starter neurons are labeled by both and they can be found only in the IGL (left upper row) in the dLGN (left bottom row) only singular labeled neurons can be found. (C) Example of a retina back-labeled from Sox14 cells. (D) The two dominant cell type found in the back-traced retina: ipRGCs (left) and DS cells (right). (E) Side view of an ON-OFF DS cell. (F) The proportion of different cell classes from all successful tracing experiments. (G) Example retinas of an IGL, PAG and SCN injected animals. Colored dots show the different*

ganglion cell types.

Summarizing Discussion

In my thesis I presented multiple projects focusing on the study of the anatomy, physiology and development of retinal micro circuits of the non-image forming vision. One of the major technique we have used here is transsynaptic viral tracing. First, we developed a set of retrograde, multisynaptic PRV strains in order to facilitate and extend the use of transsynaptic tracing. We introduced a transsynaptic viral tracer which expresses a genetically encoded calcium indicator and the first time neuronal activity was recorded from trans-synaptically targeted neurons with calcium imaging. Furthermore, a second fluorophore which expressed 7 hours later than the calcium indicator allowed the discrimination between early and late infections. Recording from cells in the early phase of the infection decreases the likelihood of recording neuronal activity from cells affected by the cytotoxic effect of the tracer virus. Still, one of the major problem with transsynaptic tracing is cytotoxicity. Even with the less toxic RV tracers it is difficult to find both the starter cell and the first order neurons at a sufficiently labeled and healthy state at the same time(*19*). The cytotoxic effect is a composition of the direct toxicity of the replicating virus and the adverse reaction of the immune system. To increase performance one can target both contributing factor. The replication of the virus is essential for the transsynaptic spread, but even if the virus has no direct toxic proteins, the continuous reproduction of the viral particles exhaust the resources of the host cell. This could be prevented by stopping the replication of the tracer virus in the starter cell after the transsynaptic jump. One can achieve this with inducible deactivation of the tracer genome, which is than unable to serve as a template for further replication and gene expression. With current technologies this might be more feasible with DNA viruses, since DNA editing tools such as the Cre-recombinase are highly efficient, while RNA viruses could rely on RNA interference. One role of the immune system is to identify and eliminate the infected cells, therefore silencing the anti-viral immunity could elongate the survival time of the infected neurons as well. Other obstacle in viral tracing is, that it is limited to the retrograde direction. While wild type RV can only spread retrogradely, the wild type herpes viruses (HSV, PRV) can spread both anterograde and retrograde direction(*142*). In PRV, the proteins essential for the anterograde

but not necessary for the retrograde spread has been identified and their elimination leads to a retrograde-only virus (*51*, *143*). In contrary, no protein has been found which is required exclusively for the retrograde spread. The HSV-1 strain H129 was reported to spread only anterogradely (*57*), but a recent study showed that it also spread into the retrograde direction (*144*). Others tested the vesicular stomatitis virus (VSV) and found that it spread anterogradely. Despite these reports transsynaptic anterograde studies remained absent in the field. Better understanding of the mechanism directing and transporting the viruses within the neurons would allow us to re-engineer the viral proteins or the cellular components of the transporting machinery in order to force virus into the anterograde direction while preventing the retrograde spread.

In my work I used PRV tracers to identify the presynaptic inhibitory neurons of the M1 and M2 ipRGCs. We found that dopaminergic amacrine cells control the M1, and Arc positive amacrine cells the M2 ipRGCs. Others have shown that dopamine acts through D1 dopamine receptors and causing depolarization and reduced input resistance on M1 ipRGCs (*145*). Dopamine release is facilitated by light exposure and it also follows a circadian rhythmicity with a peak during daytime. Therefore dopaminergic amacrine cells are responsible for desensitization of the M1 cells during the day. Arc positive amacrine cells provide lateral inhibition to M2 cells, turning these ipRGCs into object detector from a simple light meter. This can indicate the role of M2 cells in image forming vision or in reporting contrast information to the non-image forming vision. The first idea is supported by our finding that melanopsin signaling reaches the visual cortex which signaling originates from one or more of the low melanopsin content ipRGCs: M2, M4 and M5. On the other hand the tracing studies from the Sox 14 mouse line revealed that M2 cells can have an antagonistic effect with M1 cells by inhibiting the SCN through the long projecting inhibitory neurons in the IGL. The expression of Arc protein in the amacrine cells raise the possibility of activity dependent modulation of the synaptic strength on M2 ipRGCs, but we could only find minor changes during a 24 four hour cycle (data not shown). However it is possible that the effect of the Arc protein follows seasonal alterations and therefore the changes could be detected on a longer time scale. In the future, one can eliminate the presynaptic neurons by using mice expressing Cre-recombinase selectively in

dopaminergic and Arc positive amacrine cells and perform behavioral tests addressing circadian rhythm and pupillary light reflex to clarify the exact role of those neurons in the non-image forming vision.

Finally, our studies on the INL circuits of the DS cells rejected the former view about the contribution of the excitatory bipolar cells in the formation of direction selectivity on DS cells (*80*, *87*). We also found that the asymmetric inhibitory inputs required for directional selectivity, develops from a previously built symmetric configuration. The molecular mechanism of this restructuring remained unclear. It is very likely that the key molecular components of the asymmetry are expressed specifically in the starburst cells and DS cells. Their genetic expression profile is partially known(*146*), which principally allow us to knock out the specifically expressed genes one by one and testing the knock out animals with various methods addressing optokinetic reflexes. This however due to the high number of candidate genes would require enormous amount of resources and time. Other approach could be to investigate the underlying mechanism of such human conditions when eye movements are altered due to genetic factors. Congenital nystagmus is diseases with genetic origin represented by disturbed horizontal but intact vertical eye movements (*147*). The underlying gene, the frmd7 is a possible candidate for starting the roll up the network of molecules required for the asymmetry required for direction selectivity.

Experimental Procedures

Chapter 1

Cells and viruses. Subconfluent monolayers of a porcine kidney (PK-15) cell line were used for the propagation of PRVs. Cells were grown in Dulbecco's Modified Eagle's medium (DMEM) supplemented with 5% fetal calf serum at 37°C with 5% CO2. PRV strains Kaplan (Ka) and Bartha (Ba) were used as parental viruses to produce each recombinant PRV. Virus stocks used for infections were prepared, aliquoted and stored as described11, 17-19.

Construction of PRV-targeting vectors. Targeting vectors were used to deliver reporter genes and/or mutations to the PRV genome (Supplementary Fig. 3). A typical targeting vector was constructed by the insertion of a reporter gene expression cassette to an internal position of a previously subcloned viral DNA segment, which provided homologous flanking sequences for recombination with the desired integration site in the PRV genome. Reporter genes with references are shown in Supplementary Table 3, summary of the flanking sequences can be found in Supplementary Table 4.

Flanking sequences. PRV DNA segments of interest were subcloned into members of a palindrome-containing positive-selection vector family (pRL479, pRL525, pRL49418, 20). Subsequently, viral DNA sequences were cut with one or two unique restriction endonucleases, followed by Klenow filling-in of 5'-overhangs and insertion of either an EcoRI or a HindIII linker, which served as a cloning site for the incorporation of reporter gene expression cassettes (Supplementary Fig.3 a-c). Supplementary Table 4 shows PRV genomic regions that were utilized as flanking sequences in this study.

ASP (putative antisense promoter) region. The BamHI-8' PRV DNA fragment was isolated and subcloned into the pRL525 vector resulting in p525-B8'. The DraI site of this PRV sequence was converted to EcoRI by linker insertion generating pASP-RI. Alternatively, BamHI-8' fragment was subcloned into pRL479 to give p479-B8', followed by conversion of the DraI site to HindIII

resulting in pASP-HIII. The various reporter gene expression cassettes were inserted either into the EcoRI site of pASP-RI or into the HindIII site of pASP-HIII, resulting in the generation of ASP-based targeting constructs.

gE-gI (glycoprotein E and I gene) region. The BamHI-7 PRV DNA fragment was isolated and subcloned into the pRL525 vector to give p525-B7. The 1855-bp StuI – AgeI DNA fragment of p525-B7 was replaced by an EcoRI linker generating pgEgI-RI. Removal of the StuI – AgeI DNA fragment resulted in the inactivation of both gE and gI genes of the virus.

vhs (virion host shut-off gene) region. The 2526-bp XhoI DNA fragment containing the entire VHS gene was subcloned into the SalI site of pRL494 resulting in p494-Xh. The unique NruI site of this DNA segment was converted to an EcoRI site (generating pVHS-RI) by linker insertion, which resulted in a frameshift mutation in the VHS gene.

ep0 (early protein 0 gene) region. The first step in creating the ep0 deletion-based flanking sequence was to subclone the KpnI-F fragment of PRV to pRL525 (p525-KF), followed by the deletion of a 1388-bp BamHI fragment containing the entire ep0 gene. The BamHI site was replaced by an EcoRI site via Klenow filling and linker insertion, resulting in pEP0-RI.

Reporter genes. The reporter genes used in our work are listed in Supplementary Table 3. For creating membrane targeted FPs, reporter genes were fused with MARCKS2 (myristoylated alanine-rich C-kinase substrate). Each expression cassette was modified to contain either EcoRI or HindIII restriction endonuclease sites at both ends for subcloning into flanking viral sequences. The expression cassettes are available by request.

Generation of recombinant viruses. Recombinant viruses were generated by homologous recombination between parental PRV genomes and the homologous sequences of the targeting vectors. Viral DNA was transfected into actively growing PK-15 cells, along with the linearized targeting vector (Lipofectamine 2000 Reagent, Invitrogen). Supplementary Table 1-2 shows the list of recombinant viruses with their mutations and reporters used in this study. Plaques formed by recombinant viruses were detected on the basis of their fluorescent colour or by blue plaque assay in case of LacZ. Recombinant viruses were isolated by 6-15 cycles of plaque purifications. Deletions in the viral genome without reporter gene insertion were generated by

insertion and subsequently elimination (via empty flanking sequences) of the FP or LacZ expression cassette.

Naming convention. Names for different PRV strains in the text are composed from the names listed in column 1 of Supplementary Table 2 and the genome groups listed in Supplementary Table 1. For example As1-PRV06 refers to an Activity sensor PRV where TN15 is inserted into a genome group 06 PRV.

Characterization of recombinant viruses. Expression level, cytotoxicity and stability were tested in vitro, infectivity were analyzed in vivo. We assumed that expression level, cytotoxicity and infectivity are independent from the FP, therefore we used the EYFP and TN-L15 expressing variants of each of the 9 genetic groups for these tests detailed below, and the results are shown in Supplementary Table 1.

Expression level and cytotoxicity: PK15 cells were plated in 6 well plates at 106 cells/plate. The following day EYFP and TN-L15 expressing strains of each genetic group were added at a MOI of 3. To measure the expression levels 12 hours later citrine (TN-L15) and EYFP emissions were recorded via fluorescence microscopy at 535 ± 30 nm. Citrine emission intensity was compared with EYFP emission intensity by multiplying the citrine emission intensity with the average EYFP/citrine ratio of isogenic strains (EYFP and TN-L15 expressing strains from the same genetic group) resulting a single value for each genetic group. These values were than normalized to the fluorescence emission intensity of an EYFP expressing plasmid 48 hours post-transfection. Cytotoxic effect was measured with Trypan Blue 20 hours after the plated cells were infected. We added 0.4% Trypan Blue (Gibco) for 30 seconds to the plates and counted the dead (blue) cells. The number of dead cells corresponding to the different genetic groups was normalized to the dead cell count of Ti1-PRV07 infected plates.

Infectivity: We injected adult C57BL6/J mice i.p. with viruses from each genetic group, and tested which titer of the viruses results more than 50% lethality of the injected animals. Three animals/virus strain/titer were injected at a titer of 102-108 plaque forming units/ml in a volume of 200µl. Results are shown in Supplementary Table 1.

Stability: We found that a fraction of recombinant PRVs lose their fluorescence during viral replication in vitro. Based on semi-quantitative observations during virus isolation we give an evaluation of each virus strain in terms of stability in Supplementary Table 2. For the stability assay we isolated individual fluorescent plaques and infected another plate of PK-15 cells with them. Next we determined the ratio of non-fluorescent per total plaque number.

PRV injection. PRV strains were harvested from PK-15 cell line as described11. To label the pupillary reflex pathway, the cornea of 8-14 weeks old C57BL/6J mice was punctured with a 27-28-gauge needle under isoflurane anesthesia (2% in oxygen) and 103-105 plaque forming units of PRV in 1 µl DMEM was injected into the AntC of the right eye, using a 10-µl Hamilton syringe fitted with a 33-gauge needle. To infect selected brain regions, 103-104 plaque forming units of PRV in 100 nl DMEM was injected into different locations using stereotaxic surgery. PRV work was performed in a biosafety level 2 laboratory. Animal experiments have been approved by the local Institutional Animal Care and Use Committee at the Friedrich Miescher Institute and conducted according to the guidelines of the US National Institute of Health and the Swiss National Foundation.

Transgenic mice. TN-L15, a gift of O. Griesbeck, was excised from TN-L15/pcDNA3 1 with BamHI (5') and EcoRI (3'). The 1860-bp fragment was subcloned into pBluescriptII KS(+) (Stratagene) using BamHI (5') and EcoRI (3') restriction sites and further subcloned into pULmEB (pcDNA3.1(+) backbone from Invitrogen) using KpnI (5') and NotI (3') sites. An EcoRI fragment was isolated and was blunt-ended using T4 polymerase and inserted into the XhoI cut and blunt-ended pThy1-mEGFP vector2 yielding pTTN. This plasmid was linearized with NotI and PvuI. The linear fragment was used for pronuclear injections to generate transgenic mice.

Immunohistochemistry. The retina was fixed in 4% paraformaldehyde (PFA) in phosphate buffered saline (PBS) at pH 7.4 for 30 minutes at room temperature (RT) and washed in 50 ml PBS for 1-5 days at 4 ºC. Brains were fixed in 4% PFA in PBS for 2 hours and incubated in 200 ml PBS overnight at RT. The brain was embedded in 2% agar in PBS and vibratome sectioned to 100-µm thick sections. The antibody staining procedure for both the retina and the vibratome sections were the same and were carried out at RT. The tissue was blocked for 1 hour in 10%

Normal Goat Serum (NGS) or Normal Donkey Serum (NDS), 1% Bovine Serum Albumin (BSA) and 0.5% Triton X100 in PBS (pH 7.4) followed by incubation with the primary antibodies in 3% NGS (or NDS), 1% BSA, 0.5% Triton X100 in PBS for 3 days. After three rounds of 10-20 minute washes in PBS, the secondary antibodies were applied for two hours in 2-10 µm/ml DAPI, 3% NGS (or NDS), 1% BSA, 0.5% Triton X100 in PBS. For GFP immunohistochemistry after secondary antibody incubation, the tissue was washed three times in PBS as before and incubated overnight with streptavidin conjugated to Alexa 488 (Invitrogen) in 0.5 % Triton X100 in PBS. At the end of the staining procedure the tissue was washed three times in PBS and mounted with ProLong antifade mounting medium (Invitrogen). The following primary antibodies were used: rabbit anti-GFP (1:200 or 1:500, Invitrogen), sheep anti-GFP

(1;200, Biogenesis), rabbit anti-melanopsin (1:5000, kind gift from I. Provencio, Uniform Services University, Bethesda, MD), rabbit anti-RFP (1:200, Invitrogen), chicken anti-RFP. Secondary antibodies were conjugated with Biotin (for GFP staining), Alexa 488 or Alexa 555 (Invitrogen).

Confocal microscopy and analysis. The 405, 488 and 543 nm laser lines of a Zeiss LSM 510 Meta confocal microscope were used to excite DAPI, Alexa 488 and Alexa 555 respectively. A 63X, 1.4 numerical aperture oil immersion Objective (Zeiss) was used. The z steps were 0.2-0.35 microns. The scan started at the ganglion cell layer and continued until the photoreceptor layer.

Wide field fluorescence microscopy. Time-lapse fluorescence imaging of Ti-PRV infected PK15 cells were carried out with a wide field fluorescent microscope (Zeiss Long Run, TILL5, Axiovert 200m). We captured the green and red emission in 20-minute intervals up to 14-24 hours post-infection. Image analysis was performed with ImageJ software.

Two-photon imaging. A tunable 800-1020 nm laser line from a Mai Tai HP two-photon laser (Spectra Physics) was attenuated by polarization optics and a Pockels cell (Conoptics, Model 302), and was scanned using mirrors (Cambridge Technologies) mounted on a modified Olympus BX51 upright microscope. The laser energy at the position of the retina was 5-20 mW. The CFP and citrine TN-L15 signal was detected with two PMTs as described7.

Retina. The retina was isolated in Ringer's medium (in mM: 110 NaCl, 2.5 KCl, 1 CaCl2, 1.6 MgCl2, 10 D-glucose, 22 NaHCO3, bubbled with 5% CO2/95% O2), mounted ganglion cell side up on a filter paper (MF-membrane, Millipore,USA), and superfused in Ringer's medium at 36-36.5°C in the microscope chamber for the duration of the experiment. For time-lapse imaging the retina was superfused (as described above) for one day, and at every hour several regions were optically sliced (z-stacks, 1-µm stepsize, 50-µm thickness) starting from the ganglion cell layer.

Cell Culture. To define the relative intensities of the different As1-PRV strains, we measured the fluorescence intensity of TN-L15 in 50-100 labeled cells/strain 24h post-infection in PK15 cells. The samples were excited with a two-photon laser at 950 nm, the emission intensity was measured at 525/50.

Electrophysiology and light stimulation. The retina was isolated and perfused as described above. Virus- labeled ganglion cells were visualized by two-photon imaging and targeted by glass electrodes under the guidance of an infrared camera. The resistance of the electrodes was 7 -9 MΩ and the electrodes were filled with (in mM): 115 KGluconate, 9.7 KCl,1 Mg Cl2, 0.5 CaCl2, 1.5 EGTA, 10 HEPES, 4 ATP-Na2, 0.5 GTP-Na3 (pH 7.2). Multiclamp 700B patch clamp amplifier (Axon Instruments) was used to stimulate cells. The visual stimulation and data acquisition software was written in LabView (National Instruments) by David Balya and Thomas Münch. Data were analyzed in Mathematica or Matlab. Visual stimuli were applied using a digital light processor (DLP) projector through the lamp port of an Olympus BX51 upright microscope. The image was focused on the photoreceptors through the condenser before the experiment.

Statistical Analysis. p values were obtained using the Student's t-test. Differences were considered statistically significant at the $p < 0.05$ level, indicated with * and highly significant if $p<0.01$, indicated by ** on the figures. $P<0.001$ is indicated by ***.

PRV Labeling. GFP-expressing pseudorabies virus (PRV) 152 (*21*) and RFP-expressing PRV 614 (kindly provided by B.W. Banfield) (*56*) Bartha strains were harvested from the PK-15 cell line as described earlier (*21*). To create the PRV expressing the membrane-targeted green fluorescence protein (memGFP), we used the first 40 amino acids of the myristoylated alanine-rich C kinase substrate (MARCKS) protein fused with GFP (*52*) under control of the cytomegalovirus (CMV) immediate-early promoter. The CMV-memGFP expression cassette was placed into the putative latency-associated transcript promoter (PLAT2) (*148*) of the PRV Bartha strain. All the PRV work was done in a biosafety level 2 laboratory. C57BL/6J mice that were 6–8 weeks old were injected with 103 –105 plaque-forming units of PRV152 in 1 ml Dulbecco's Modified Eagle's Medium (DMEM) into the AntC of the right eye under isoflurane anesthesia (2% in oxygen). Animal experiments have been approved by the local Institutional Animal Care and Use Committee at Harvard and the Friedrich Miescher Institute. Animal experiments have been conducted according to the guidelines of the U.S. National Institutes of Health and the Swiss National Foundation. The cornea was punctured with a 27–28 gauge needle, and PRV152 was injected into the anterior chamber (AntC) with a 10 ml Hamilton syringe fitted with a 33 gauge needle. For labeling ganglion cells that projected to the superior colliculus (SC) or to the lateral geniculate, we performed stereotaxic surgery. We injected 104 plaque-forming units of PRV152 in 100 nanoliter DMEM into either the SC or V1. Animals were kept in the same laboratory for up to 150 hr after injection.

Immunohistochemistry. The retina was fixed in 4% paraformaldehyde in phosphate-buffered saline (PBS) at pH 7.4 for 30 min either after electrophysiological recordings or directly after eye enucleation and incubated at 4C for 1–5 days. For vibratome sectioning, the retina was embedded in 2% agar in PBS and cut into 100–200-mm-thick sections with a Leica VT 1000 S vibratome. For cortical slides, the whole brain was embedded in 2% agar in PBS and vibratome sectioned into 200-mm-thick sections. The antibody-staining procedures for both whole-mount and vibratome sections were the same and were carried out at room temperature. The retina was blocked for 1 hr in 10% normal goat serum (NGS) or normal donkey serum (NDS), 1%

bovine serum albumin (BSA), and 0.5% Triton X-100 in PBS (pH 7.4); incubation with the primary antibodies in 3% NGS (or NDS), 1% BSA, and 0.5% Triton X-100 in PBS for 3 days followed. After three rounds of 10–20 min washes in PBS, the secondary antibodies were applied for 2 hr in 2–10 mg/ml DAPI, 3% NGS (or NDS), 1% BSA, and 0.5% Triton X-100 in PBS. For GFP immunohistochemistry after secondary-antibody incubation, the retina was washed three times in PBS as before and incubated overnight with streptavidin conjugated to Alexa 488 (Invitrogen) in 0.5% Triton X-100 in PBS. At the end of the staining procedure, the retina was washed three times in PBS and mounted with ProLong antifade mounting medium (Invitrogen). The following primary antibodies were used: rabbit anti-GFP (1:200 or 1:500, Invitrogen), sheep anti-GFP (1:200, Biogenesis), rabbit antimelanopsin (1:5000, kind gift from I. Provencio, Uniform Services University, Bethesda, MD), mouse anti-calretinin (1:2000, Chemicon), and mouse anti-glutamine synthetase (1:200, Chemicon). Secondary antibodies were conjugated with Biotin (for GFP staining), Alexa 488, or Alexa 633 (Invitrogen). For double labeling, rabbit anti-GFP was used together with mouse primary antibodies, NGS-containing blocking solution, and goat secondary antibodies. Sheep anti-GFP was used together with rabbit primary antibodies, NDS-containing blocking solution, and donkey secondary antibodies.

Confocal Microscopy and Analysis. The 405, 488, and 633 nm laser lines of a Zeiss LSM 510 Meta confocal microscope were used to excite DAPI, Alexa 488, and Alexa 633, respectively. To determine the dendritic depths of PRV-labeled ganglion cells, we acquired confocal stacks of 170 ganglion cells with an automatic stage controlled by Auto Time Series Macro software (*149*) In each imaging session, 20–30 ganglion cells per retina were marked, and confocal stacks (*149*) were acquired at each location. We used a 633 1.4 numerical-aperture oil-immersion lens (Zeiss). The z steps were 0.2–0.35 mm. The scan started at the ganglion-cell layer and continued until the photoreceptor layer. The depth of dendritic ramification for each labeled ganglion cell was determined from the DAPI and Alexa 488 stacks. In brief, the dendritic depths were automatically determined relative to the GCL border and the INL border with an algorithm written in Matlab (Math Works). The GCL border (0% depth) was defined as the depth at which DAPI fluorescence peaked in the GCL **Figure 2-1 D**, and the INL border (100% depth) was defined as the depth at which the DAPI florescence was 66% of the maximum measured in the

INL (**Figure 2-1 D**). Dendritic depths were calculated locally near each dendritic segment to eliminate artifacts caused by the fact that the retina is not entirely flat. To reconstruct the detailed 3D morphology of PRVlabeled amacrines cells that were further away from the ganglion cell body, we acquired several overlapping image stacks and stitched them together with an algorithm that calculated the correlation between neighboring frames in the ganglion-cell layer of DAPI labeled stacks. The stitching algorithm was implemented in Mathematica (Wolfram Research). 3D visualization for **Figure 2-1 C** and **Figure 2-2 C** was done in Imaris (Bitplane). Colocalization of calretinin and GFP in the INL was quantified by the following algorithm in Mathematica: Confocal scans were acquired at a number of locations in the INL for DAPI, calretinin, and GFP. From the DAPI scan, the location of every cell nucleus was determined. Next, the GFP and calretinin channels were thresholded and for each nucleus the number of GFP- and/or calretinin-positive pixels around the nucleus were counted in a fixed window and plotted in. The horizontal axis shows the number of GFP-positive pixels and the vertical axis shows the number of calretinin-positive pixels for each cell.

Electrophysiology. Three to six days after PRV152 injection into the AntC of the right eye, the left eye was removed and the retina was dissected. The isolated retina was continuously superfused at a rate of 1 ml/min with Ames (pH 7.4) solution at 36C and equilibrated with 95% O2 and 5% CO2. We recorded inhibitory currents from GFP-labeled ganglion cells under a voltage clamp with electrodes (5–8 MU) that were filled with 113 mM CsMeSO4, 1 mM Mg SO4, 7.8 mM 1023 CaCl2, 0.1 mM BABTA, 10 mM HEPES, 4 mM ATP-Na2, 0.5 mM GTP-Na3, 5 mM QX314-Br, and 7.5 mM Neurobiotin-Cl at pH 7.2 with a Multiclamp 700B patch-clamp amplifier (Axon Instruments). GFP-labeled ganglion cells were visualized by two-photon laser confocal imaging. Inhibitory currents were measured by clamping the membrane to 0mV, the reversal potential for ionotropic glutamate receptors. The recorded change of currents in the voltage clamp at 0 mV is proportional to the change of inhibitory conductance. QX314 was used to block sodium currents internally. The visual-stimulation and data-acquisition software, Presentinator, was written in LabView (National Instruments) in the laboratory of F. Werblin at the University of California, Berkeley. Data were analyzed in Mathematica. Visual stimuli were applied with a digital light processor (DLP) projector through the lamp port of a Nikon Eclipse

600 upright microscope. The image was focused on the photoreceptors through the condenser before the experiment.

Two-Photon Imaging. A two-photon laser-scanning confocal microscope was used to visualize GFP-labeled neurons in the retina in order to avoid bleaching of the photoreceptors. A 920 nm laser line from a 5W Millennia Pro pumped Tsunami laser (Spectra Physics) was attenuated by polarization optics and a Pockels cell (Conoptics, Model 302) and was scanned with mirrors (Cambridge Technologies) mounted on a modified Nikon Eclipse 600 upright microscope. The laser energy at the position of the retina was 5–20 mW. The acquisition software, Tango, was written by Florian Engert, Harvard University (Cambridge, MA). For time-lapse imaging, the retina was superfused (as described above) for one day, and at every hour or half hour a Z stack of 80 images was acquired with 1 mm spacings. At the end of the timelapse imaging, the retina was fixed in 4% paraformaldehyde in PBS and stained with antibodies for visualization of the circuit at a higher resolution.

Chapter 3

Animals. ChAT–Cre mice were purchased from Jackson Laboratory (strain: B6;129S6-Chattm1(cre)Lowl/J). In ChAT–Cre mice, Cre recombinase is expressed under the control of the ChAT locus. In SPIG1–GFP mice GFP is expressed under the control of the SPIG1 locus. To obtain neonatal SPIG1–GFP × ChAT–Cre mice we crossed SPIG1–GFP homozygous mice with ChAT–Cre homozygous mice. All animal procedures were performed in accordance with standard ethical guidelines (European Communities Guidelines on the Care and Use of Laboratory Animals, 86/609/EEC) and were approved by the Veterinary Department of the Canton of Basel-Stadt, Switzerland.

AAV plasmids. In the present paper, we refer to the C128T mutant ChR2 as ChR2c. To obtain pAAV-EF1a-double floxed-ChR2c–2A–DsRed2-WPRE-hGHpA we linearized pAAV-EF1a-double floxed-hChR2(H134R)-EYFP-WPRE-hGHpA (provided by K. Deisseroth) using NheI/AscI. ChR2c was PCR-amplified from pGEMHE-ChR2c using a HindIII-2A-covering primer. Forward primer: 5′-GCTAGCGCTAGCCACCATGGATTATGGAGGCGCCCTG-3′. Reverse primer: 5′-TCTCCCGCAAGCTTAAGAAGGTCAAAATTCTTGCCGGTGCCCTTGTTGAC-3′. DsRed2 was PCR-amplified from pDsRed2-N1 (Clontech) using a HindIII-2A-covering primer. Forward primer: 5′-ACCTTCTTAAGCTTGCGGGAGACGTCGAGTCCAACCCTGGGCCCATGGCCTCCTCCGAGAACGTC-3′. Reverse primer: 5′-GGCGCGCCGGCGCGCCCTATCACAGGAACAGGTGGTGGCG-3′. These two PCR products were then digested with NheI, AscI and HindIII and triple ligation was performed.

AAV production. Serotype 7 recombinant AAVs were made by Penn Vector Core. Penn Vector Core performed the genome copy (GC) number titration (titre: 5.78 × 1012 GC per ml) using real-time PCR (TaqMan reagents, Applied Biosystems).

Logic of AAV labelling. We used the viral vector AAV EF1a-double floxed-ChR2c–2A–DsRed2 to target the expression of ChR2c to starburst cells expressing Cre. In AAV EF1a-double floxed-ChR2c–2A–DsRed2, two incompatible loxP variants31, loxP and lox2722, flank an inverted version of ChR2c followed by the red fluorescent marker DsRed2. In the presence of Cre, a stochastic recombination of either loxP variant takes place, resulting in the inversion of ChR2c–2A–DsRed2 into the sense direction, followed by expression of the ChR2c–2A–DsRed2. The 2A element32 codes for a cis-acting hydrolase element26 that creates equimolar amounts of ChR2c and red-fluorescent DsRed2.

AAV injection. We injected the virus at the day of birth. SPIG1–GFP × ChAT–Cre mice were anesthetized with crushed ice. Virus (1.5 µl, 8.68 × 109 GC) was loaded into pulled glass pipettes (tip diameter, 30 µm) and injected into the vitreal space of both eyes using a microinjector (Narishige). After 6 days, DsRed2 expression was brightly detectable; hence all recordings were performed on retinas at P6 or later.

Preparation of retinas. Neonatal mice were killed by decapitation. Eyes were enucleated. The retinas were isolated and the pigment epithelium removed in Ringer's medium (in mM: 110 NaCl, 2.5 KCl, 1 CaCl2, 1.6 MgCl2, 10 D-glucose, 22 NaHCO3, bubbled with 5% CO2/95% O2, pH 7.4) and mounted ganglion-cell-side up on a filter (MF-membrane, Millipore) with a 2-mm rectangular aperture in the centre. Before starting superfusion, DsRed2-positive regions together with GFP-positive cells were located with an epifluorescence stereomicroscope (Olympus) and photographed for later determination of the average DsRed2 fluorescence intensity around recorded ON DS cells for data normalization and orientation of the retina. Only GFP cells surrounded by DsRed2 expression were chosen for the recordings. The orientation of the isolated SPIG1–GFP × ChAT–Cre retina was determined by the pattern of GFP expression. In most retinal regions, GFP is expressed exclusively in one type of ON DS cells during the developmental period. An exception is the dorsal (slightly temporal) region, where GFP is expressed in many different ganglion and amacrine cell types. A thick axon bundle in this region

runs in the dorso-ventral direction towards the optic disk and can be used as a compass in isolated retinas9. The retinas were superfused in Ringer's medium at 35–36 °C in the microscope chamber for the duration of the experiment. In this retinal preparation, ChR2c-mediated light responses could be measured for more than 8 h.

Two-photon imaging, electrophysiology and pharmacology. Fluorescent cells were found with the help of a two-photon microscope equipped with a Mai Tai HP two-photon laser (930 or 1,010 nm) (Spectra Physics) integrated into the electrophysiological setup30. Current recordings were made in whole-cell voltage clamp mode using an Axon Multiclamp 700B amplifier with borosilicate glass electrodes (BF100-50-10, Sutter Instruments) pulled to 7–9 MΩ, and filled with (in mM) 112.5 CsCH3SO3, 1 MgSO4, 7.8 × 10−3 CaCl2, 0.5 BAPTA, 10 HEPES, 4 ATP-Na2, 0.5 GTP-Na3, 5 lidocaine N-ethylbromide (Qx314-Br), 7.75 neurobiotin chloride, pH 7.2. Excitatory and inhibitory synaptic currents ('excitation' and 'inhibition', respectively) were separated by voltage-clamping the cell to the equilibrium potential of chloride (−60 mV) and unselective cation channels (20 mV), respectively29. For recording mEPSCs, cells were voltage-clamped at −60 mV and recorded for 3–5 min. Voltage recordings from DsRed2-positive starburst cells were made in whole-cell current clamp mode with glass electrodes pulled to 7–9 MΩ and filled with (in mM) 115 K-gluconate, 9.7 KCl, 1 MgCl2, 0.5 CaCl2, 1.5 EGTA, 10 HEPES, 4 ATP-Na2,, 0.5 GTP-Na3, pH 7.2. In pharmacological experiments, agents were bath-applied at the following concentrations: 10 µM CPP ((±)-3-(2-carboxypiperazin-4-yl) propyl-1-phosphonic acid, blocking NMDA receptors), 10 µM NBQX (6-nitro-2,3-dioxo-1,4-dihydrobenzo[f]quinoxaline-7-sulfonamide, blocking AMPA and kainate receptors), 10 µM APB (L-(+)-2-amino-4-phosphonobutyric acid, blocking metabotropic glutamate receptors and therefore blocking the ON pathway), 50 µM curare (tubocurarine chloride, blocking nicotinic acetylcholine receptors), 100 µM picrotoxin (blocking GABA A and C receptors). All chemicals were obtained from Sigma, with the exception of APB (Calbiochem). Data were analysed offline with Mathematica (Wolfram Research).

Photostimulation. ChR2c was activated with light generated by a digital light projector (V-332, PLUS Vision). The stimulation was generated via custom-made software (Matlab, Mathworks; Labview, National Instruments). Light intensity was measured using a spectrometer (USB 4000, Ocean Optics) calibrated with a reference source (LS1-Cal, Ocean Optics). Light intensity was modulated by using different grey scales (0–255) combined with different neutral density filters (ND0, ND10, ND20 and ND 30). To correlate the stimulus intensity and the change in membrane potential in ChR2c-expressing starburst cells (Supplementary Fig. 2), we used full-field flash at 24 different intensities (12.08–15.86 in Log intensity photons cm−2 s−1) presented for 2 s with an inter-stimulus interval of 5 s. For the stimulation of the eight sectors (Figs 3, 4), each stimulus was presented for 2 s with an inter-stimulus interval of 10 s. The eight sectors were stimulated in a random order. The light pattern was focused on the GCL. To find a 'weak light intensity' that evoked half the maximum excitatory current input to ON DS cell (Supplementary Fig. 9), full-field flash at 24 different intensities (12.08–15.86 in Log intensity photons cm−2 s−1) was presented sequentially (presentation for 2 s with an inter-stimulus interval of 5 s) initially and next the retinas were then stimulated in eight sectors using the determined light intensity.

Data collection and analysis. Light stimulation of each of the eight sectors (Fig. 3g) around the recorded ON DS cell body was repeated in each recorded ON DS cell 3–10 times for both excitation and inhibition and the mean light responses were determined for all eight directions. To correct for non-uniform viral expressions in the eight sectors, we performed two different types of normalizations. In the first procedure, we normalized the current evoked in each sector by the number of DsRed2-expressing cells in the sector within 200 μm of recorded ON DS cell bodies in the GCL. Here we used an arbitrary fluorescence threshold that was constant between experiments. We choose the particular distance of 200 μm because the radius of the dendrites of ON DS cells plus the radius of the processes of starburst amacrine cells at P6 and P9 were together less than 200 μm (data not shown).

In the second procedure, we normalized each sector to the average fluorescence intensity of the starburst cells in the sector and not just the number. This was reasonable because the fluorescence intensity of the starburst cells correlated well (R = 0.83) with the magnitude of the voltage response of the starburst cell at the stimulation intensity used for the mapping procedure (Supplementary Fig. 2): therefore, the average fluorescence is a measure of the stimulation strength of the starburst cells in the sector.

To yield the eight quantities plotted on polar plots, these normalized (or not normalized) values were further normalized to the largest of the eight numbers (for excitation and inhibition, independently). Note that this normalization is useful for eliminating variations in synaptic currents arising from the patch-clamp technique including series resistance and leak conductance. Note that the largest value (of the eight) to which normalization is performed is a mean of a distribution since each segment was stimulated 3–10 times (see above). The direction of the tuning was determined by multiplying the eight values above with the corresponding unit vectors pointing in eight directions and then forming the vector sum. The direction of the vector sum was interpreted as the direction of tuning. The spatial asymmetry index (SAI) was calculated as: $SAI=(I_{ventral} - I_{dorsal})/(I_{ventral} + I_{dorsal})$ where $I_{ventral}$ and I_{dorsal} are the amplitudes of the normalized or not normalized currents evoked by the stimulation of ventral or dorsal sectors (both normalized and not normalized SAIs are shown in **Figure 3-3**).

Monosynaptic restriction of circuit tracing. To create rabies G-expressing replication-defective herpes simplex virus-1 (HSV1), the GFP open reading frame (ORF) in the HSV1 vector pR19EF1a-GFP-WCm (Biovex) was replaced with that of G. First, the G ORF was amplified by PCR from pHCMV-G33 using primers 5'-GTGTCGTGAGGAATTCGTACCGGATCCTCTAGGCCACC-3' and 5'-CCGCTTTACTTGTACATTACAGTCTGGTCTCACCCCCACT-3'. The GFP ORF was removed from pR19EF1a-GFP-WCm by EcoRI/BsrGI digestion and the PCR fragment of G was recombined into EcoRI–BsrGI site using an in-fusion PCR kit (Takara-Clontech). The viral particles were produced by Biovex. G-deleted rabies virus encoding mCherry (SADΔG-mCherry) was a gift from E.

Callaway. Rabies virus expressing mCherry instead of the G glycoprotein was harvested from BHK-B19G cells (provided by E. Callaway) and centrifuged as described earlier(*46*). We performed stereotaxic surgery to label ganglion cells projecting to the medial terminal nucleus (MTN). A cocktail of 103 plaque-forming units of rabies virus and 6 × 104 plaque-forming units of HSV1 in 20 nl DMEM were loaded into pulled-glass pipettes (tip inner diameter of 20–30 µm) and injected into the MTN using a microinjector (Narishige, IM-9B). For control experiments, we injected 2 × 105 plaque-forming units of rabies virus. Injections were performed with 24 mice at P1. Retinas were isolated at P6. Six well infected retinas at P6 were fixed by PFA and stained with antibodies. Brains were also isolated and the injection sites were localized. All rabies and HSV1 work was carried out under Biosafety level 2 conditions.

The key point of viral tracing was to infect with rabies and herpes viruses an upward-motion sensitive ON DS ganglion cell to initiate the retrograde passage of rabies viruses from this cell type. Because GFP exclusively labelled upward-motion sensitive ON DS cells in the ventral retina of SPIG1–GFP mice it was enough to examine the rabies-labelled cells around a GFP-labelled ganglion cell regardless of the injection site. The reason we performed the viral tracing in the SPIG1–GFP line was to have an internal control for the ganglion cell type for which we examine its local circuit. The fact that rabies did label GFP cells (in red) shows that the injection reached the MTN (because SPIG1–GFP cells exclusively target MTN9, 10, see also Supplementary Fig. 6). Even if by mistake we had injected these viruses also to other retinorecipient brain regions, this would not compromise our tracing results of the GFP-labelled ganglion cells provided, first, that the rabies-labelled circuits in the retina were far away so that the ganglion cell to which an amacrine cell is presynaptic to could be determined and, second, that only one ganglion cell was labelled in that local circuit. The reason we used low rabies titres for the herpes/rabies co-injections was to make sure that the circuits analysed were far away from each other in the retina (see **Figure 3-2 B**). In all circuits we analysed there was only one ganglion cell in it (which was GFP-labelled, see **Figure 3-2 D**). The definition of ‘ganglion cell’ was based on the existence of an axon.

Immunohistochemistry. After the experiments, retinas were fixed for 30 min in 4% (w/v) paraformaldehyde in PBS (137 mM NaCl, 2.7 mM KCl, 4.3 mM Na2HPO4, 1.47 mM KH2PO4, pH 7.4) and washed with PBS for at least 1 day at 4 °C. To aid penetration of the antibodies, retinas were frozen and thawed three times after cryoprotection with 30% (w/v) sucrose. All other procedures were carried out at room temperature. After washing in PBS, retinas were blocked for 1 h in 10% (w/v) normal donkey serum (NDS; Chemicon), 1% (w/v) bovine serum albumin (BSA), and 0.5% (v/v) Triton X-100 in PBS. Primary antibodies were incubated for 7 days in 3% (v/v) NDS, 1% (w/v) BSA, 0.02% (w/v) sodium azide and 0.5% (v/v) Triton X-100 in PBS. Secondary antibodies were incubated for 2 h in 3% (v/v) NDS, 1% (w/v) BSA, and 0.5% (v/v) Triton X-100 in PBS together with streptavidin-Alexa Fluor 633 (Invitrogen, 1:200) and DAPI (4',6-diamidine-2-phenylindole dihydrochloride, Roche Diagnostics, 10 µg ml−1) in some experiments. Streptavidin binds to neurobiotin and thus labels neurobiotin-filled cells; DAPI binds to DNA and therefore labels nuclei. After a final wash in PBS, retinas were embedded in Prolong Gold antifade (Invitrogen).

The following set of primary and secondary antibodies combinations were used in experiments in which we recorded from SPIG1 cells while stimulating ChR2c–2A–DsRed2-expressing starburst cells: (1) Primary: goat anti-ChAT (1:200, AB144P, Chemicon). Secondary: donkey anti-goat IgG conjugated with Alexa Fluor 405 (1:200, Invitrogen). (2) Primary: rabbit anti-red fluorescent protein (RFP; 1:200, AB3216, Chemicon). This primary antibody binds to DsRed2. Secondary: donkey anti-rabbit IgG conjugated with Cy3 (1:200, Jackson). (3) Primary: rat anti-GFP (1:500, 04404-84, Nacalai). Secondary: donkey anti-rat IgG conjugated with Alexa Fluor 488 (1:200, Invitrogen). The following set of primary and secondary antibodies combinations were used for staining rabies virus-infected retinas: (1) Primary: goat anti-ChAT (1:200, AB144P, Chemicon). Secondary: donkey anti-goat IgG conjugated with Alexa Fluor 633 (1:200, Invitrogen). (2) Primary: rabbit anti-red fluorescent protein (RFP; 1:200, AB3216, Chemicon). Secondary: donkey anti-rabbit IgG conjugated with Cy3 (1:200, Jackson). (3) Primary: rat anti-

GFP (1:500, 04404-84, Nacalai). Secondary: donkey anti-rat IgG conjugated with Alexa Fluor 488 (1:200, Invitrogen).

Confocal analysis. Stained retinas were analysed with a Zeiss LSM 700 confocal microscope. The DsRed2-expressing cell number was assessed from z-stack images by using a ×20 lens, numerical aperture (NA) 0.7, ×0.5 digital zoom. All images were recorded at the same laser power and gain control. Overall morphologies of the recorded starburst or ganglion cells were assessed using a ×40 oil immersion lens, NA 1.2, ×0.5 digital zoom or ×63 oil immersion lens, NA 1.3, ×0.5 digital zoom. The mCherry-labelled presynaptic circuits of ON DS cells were assessed from z-stack images using a ×63 oil immersion lens, NA 1.3.

Statistical analysis. The non-parametric Mann–Whitney U test was used to compare data obtained from different cells on different days and the Wilcoxon signed rank test for comparing pairs of data where each pair was obtained from the same cell (excitation and inhibition). Significance is denoted by * for $P < 0.05$ and ** for $P < 0.01$. The error bars and ± values represent standard deviations (s.d.). On each figure, the lack of stars between any pairs of data signifies $P > 0.05$ and, therefore, that the two distributions are not statistically different.

Animals. Wild-type mice (C57BL/6) purchased from Charles River were used for viral tracing experiments. Spig1-GFP mice (Yonehara et al., 2008, 2009) were used for two-photon targeted patch clamp recordings from ON DS cells. All animal procedures were performed in accordance with standard ethical guidelines (European Communities Guidelines on the Care and Use of Laboratory Animals, 86/609/EEC) and were approved by the Veterinary Department of the Canton of Basel-Stadt, Switzerland.

Rabies virus production. We replaced rabies-G with GCaMP3 or iGluSnFR in a DNA plasmid containing the rabies genome. SADΔG-GCaMP3 and SADΔG-iGluSnFR rabies viruses were recovered from this plasmid, amplified, and concentrated by ultracentrifugation, as has been described previously (Ghanem et al., 2012). Plaque-forming unit (pfu) number titration was performed by infecting BHK-wt cells and HEK293T-TVA cells with G-coated virus and EnvAcoated virus, respectively.

Herpes virus production. For the production of the HSV vector co-packaged with hEF1aTVA950 and hEF1a-rabies-G, TVA950 and rabies-G (from rabies strain CVS11) were subcloned separately into pENTR D-TOPO plasmids (Invitrogen). Those inserts were moved into the LT HSV plasmids containing an hEF1a promoter by Gateway Technology (Invitrogen). Viral vectors containing two amplicons were produced and purified on a sucrose gradient, as has been described previously (Lim and Neve, 2001).

AAV production. To obtain production plasmid for serotype-7 recombinant AAV-EF1aTVA950-T2A-RabiesG-WPRE, we linearized AAV-EF1a-XbaI-double-floxed-ChR2b-EYFPEcoRI-WPRE (kindly provided by K. Deisseroth) using XbaI/EcoRI sites. A TVA950-T2ARabiesG (from rabies strain SAD B19) insert with XbaI/EcoRI overhang sites was synthesized (Genewiz) and cut using XbaI/EcoRI. The linearized vector and the insert were ligated to yield AAV-EF1a-TVA950-T2A-RabiesG-WPRE. AAVs were made according to standard protocols. Genome copy (GC) number titration was performed (titer: 4.39×1012 GC/ml) using real-time PCR (Applied Biosystems, TaqMan reagents).

Retrograde viral tracing with rabies. We performed stereotaxic surgery in order to label ON DS cells projecting to the medial terminal nucleus. G-coated, G-deleted rabies virus (1010 pfu/ml) in 100 nl DMEM was loaded into pulled-glass pipettes (tip inner diameter 20-30 µm) and injected into the medial terminal nucleus of adult mice using a microinjector (Narishige, IM- 11-2) combined with a stereotaxic instrument (Narishige, SR-5M).

Monosynaptic viral tracing. For monosynaptic tracing, AAV (4.39×1012 GC/ml in PBS) or HSV (1.2×109 infectious units/ml in HEPES) in 50 nl was injected into the medial terminal nucleus at P3. EnvA-coated rabies virus (1010 pfu/ml) in 1 µl DMEM was injected intravitreously to the eye at P8-9 using pulled-glass pipettes and a microinjector (Narishige, IM- 11-2). Retinas were isolated for imaging and immunohistochemistry at P18-21. The key point of monosynaptic viral tracing was to infect upward or downward motionpreferring ON DS cells with a combination of rabies and herpes viruses, or rabies and AAV viruses, in order to initiate the retrograde passage of rabies viruses from this cell type. Infection of this cell type with AAV or herpes was ensured by injecting these viruses into the medial terminal nucleus, which receives retinal input exclusively from upward- and downward-sensitive ON DS cells. Importantly, we found that serotype-7 AAV is an efficient retrograde tracer for retinal ganglion cell axons. Thus, the ON DS cell types were specifically labeled with TVA and G. Since the TVA receptor binds specifically to EnvA glycoprotein, EnvA-coated rabies virus that was injected to the eye could infect only TVA-labeled ON DS cells. Since the ON DS cells also express G, rabies virus can cross the synapse only once, in a retrograde manner. Since presynaptic amacrine and bipolar cells lack G expression, the retrograde tracing is restricted monosynaptically. Because circuit labeling only occurs when both AAV/herpes and rabies viruses are present in the same cell, and because neither of these viruses infect all cells at the injection site, only 4-5 ON DS cell circuits which had a single ON DS cell were labeled in the retina. These circuits were separated in space and therefore the starburst cell, bipolar cell circuit components, could be assigned to each of these circuits. The direction selective calcium response to motion stimulus, the dendritic stratification of most dendritic segments at the proximal (ON) ChAT layer and an axon that ran laterally, proximal to the cell body were used to confirm that ON DS cells were targeted with the rabies virus. We found that bipolar cell axon terminals become visible under a two-photon microscope 10 days

after rabies injection, and ON DS cells begin to lose their light responses 14 days after rabies injection. Therefore, we performed calcium imaging between 10 and 13 days post-rabies injection (corresponding to P18-21).

Preparation of retinas. Retinas were isolated and the pigment epithelium removed in Ringer's medium (in mM: 110 NaCl, 2.5 KCl, 1 CaCl2, 1.6 MgCl2, 10 D-glucose, 22 NaHCO3, bubbled with 5% CO2/95% O2, pH 7.4) and mounted ganglion cell side up on a filter (MF-membrane, Millipore) with a 2-mm rectangular aperture in the centre. In order to find retinal regions containing rabies-labeled circuits, GCaMP3-positive cells were located using a brief exposure of light in a stereomicroscope equipped with an epi-fluorescence lamp (Leica) before the retina was positioned in the two-photon microscope. The retinas were superfused in Ringer's medium at 35- 36°C in the microscope chamber for the duration of the experiment. In this retinal preparation, stimulus-evoked currents recorded by patch clamp recording, as well as GCaMP3 and iGluSnFR responses recorded by two-photon imaging, could be measured for more than 6 h.

Two-photon targeted patch clamp recording. The two-photon microscope system and light pathways for light stimulation and targeted patch clamp recordings from GFP-expressing cells have been described before (Farrow et al., 2013). We used retinas from P16-21 Spig1-GFP mice for recordings. The current recordings were made in whole-cell voltage clamp mode using an Axon Multiclamp 700B amplifier with borosilicate glass electrodes (BF100-50-10, Sutter Instruments) pulled to 7-9 MΩ, and filled with (in mM) 112.5 CsCH3SO3, 1 MgSO4, 7.8×10-3 CaCl2, 0.5 BAPTA, 10 HEPES, 4 ATP-Na2, 0.5 GTP-Na3, 5 lidocaine N-ethylbromide (Qx314- Br), 7.75 neurobiotin chloride, pH 7.2. Excitatory and inhibitory synaptic currents ("excitation" and "inhibition", respectively) were separated by voltage-clamping the cell to the equilibrium potential of chloride (-60 mV) and unselective cation channels (0 mV), respectively, by an electrode placed at the cell body. Retinas were stimulated with light generated by a digital light projector (V-332, PLUS Vision Corp) with a refresh rate of 75 Hz, through the condenser (Nikon LWD 0.65) of the microscope. The stimulation was generated via custom-made software (Python, Python Software Foundation; Labview, National Instruments) developed by Z. Raics. Light intensity was modulated using a neutral density filter (ND30), and measured using a

spectrometer (USB 4000, Ocean Optics) calibrated with a reference source (LS1-Cal, Ocean Optics). The stimulus was a 500 µm × 100 µm, positive 100% contrast, 1000 R*/s light intensity bar moving along its long axis in eight directions at 300 µm/s. The stimulus was repeated at least three times for excitation and inhibition, and the mean light responses were determined for all eight directions. Data were analyzed offline using Mathematica (Wolfram Research). The null direction was defined as the direction with largest inhibition, and the preferred direction as the opposite direction to the null direction. The direction of the vector sum was interpreted as the direction of tuning. The directionally selective index (DSI) was calculated as: $DSI=(I_{pref} - I_{null})/(I_{pref} + I_{null})$, where I_{pref} and I_{null} are the amplitudes of currents evoked by the stimulation in the preferred and null directions, respectively.

Two-photon calcium and glutamate imaging. The two-photon microscope system was equipped with a Mai Tai HP two-photon laser tuned to 920 nm (Spectra Physics) and a 60× objective (Fluor, 1.0 NA, Nikon). Image data were acquired using custom software developed by Z. Raics, taking images of 300 × 150 pixels (4.5 frames per second) for calcium and glutamate imaging, or stacks of 512 × 512 pixels (0.25 µm/pixel, 3 µm z steps) for morphological reconstructions. A TTL signal generated at the end of each line-scan of the horizontal scanning mirror was used to trigger a UV LED projector (Acer) (Reiff et al., 2010). Stimuli were exclusively presented for between 20 and 100 µs of the fly-back period of the horizontal scanning mirror, which lasted a minimum of 300 µs after the mirror had reached its final position. The time during the scanning when fluorescent data were recorded lasted a maximum of 1.6 ms per line. The temporal switching between fluorescence recording and stimulus presentation was performed at a minimum frequency of 500 Hz, which is well above the flickerfusion frequency of the mouse retina. Visual stimulation was generated via custom-made software (Matlab, Mathworks Inc.; Labview, National Instruments). Light intensity was measured using a spectrometer (USB 4000, Ocean Optics) calibrated with a reference source (LS1-Cal, Ocean Optics). Light intensity was modulated by neutral density filters. Retinas were stimulated with a positive 100% contrast, 120 R*/s light intensity spot of 300 µm diameter moving at a speed of 400 µm/s on the retina in eight different directions.

Analysis of two-photon recordings. We treated the series of images acquired in an experiment trial as a 3D data cube, where the first two dimensions denote the rows and columns of one twophoton image, the third dimension is time. Responses recorded during repetitions of the same stimulus sequence within an experiment were averaged. In this cube, the space-time location of calcium transients can be regarded as continuous 3D objects. To detect the location of the transients we first filtered the 3D data cube, using the Wiener filter, then the result was thresholded at 2× the standard deviation of the filtered data, resulting in a binary 3D data cube that was smoothed by a 3D binary closing operator. In the resulting binary 3D data cube, 3Dcontinuous objects were detected using a connected-feature detection algorithm. To remove small transients, we further filtered the object set by setting a threshold on the spatial projections of the objects (>1.0 μm) and on the temporal projection (decay time >1 s). Next, we projected all objects on the 2D spatial plane, resulting in a connected pixel set for each object. In order to verify the cellular and subcellular identity of the recorded calcium transients we compared live two-photon image stacks with confocal image stacks (0.3 μm z-step) obtained after performing immunohistochemistry. Confocal pictures were taken in the same orientation as the two-photon images in order to simplify matching. The image matching was performed manually using Imaris (Bitplane). In confocal pictures, cell bodies and processes of starburst amacrine cell were identified as double-positive for ChAT and GFP (labeling GCaMP3). The axon terminal of bipolar cells and the dendrites of ON DS cells were both labeled only with GCaMP3, so the following two criteria were used for cellular identification. First, axon terminals of bipolar cells have a unique morphology: they have large buttons connected with thin processes, radiating from the axonal shaft (Figure S3), and stratified narrowly in the inner plexiform layer. Furthermore, in most cases, the axon terminals of bipolar cells were labeled much more brightly than other labeled structures. Second, the dendrites of ON DS cells were defined as those processes that could be traced back to a cell body, which had a direction selective response and a single axon. Dendrites of ON DS cells were thicker than processes of the starburst cells. We grouped the responding cellular compartments into five groups: ON DS cell body, ON DS cell dendrites, starburst cell body, starburst cell processes and type-5 bipolar cell

axon terminals. The directionally selective index (DSI) was calculated for the two-photon GCaMP3 signals as:

DSI=([ΔF/F]pref – [ΔF/F]null)/([ΔF/F]pref + [ΔF/F]null)

Where, in the case of an ON DS cell, [ΔF/F]pref and ΔF/F]null are the amplitudes of [ΔF/F] evoked by the stimulation in the preferred and null directions, respectively. In ON DS cells the direction of the vector sum of [ΔF/F] was interpreted as the preferred direction. The null direction was 180 degree rotated from preferred. In the case of bipolar terminals, [ΔF/F]pref and ΔF/F]null are the amplitudes of [ΔF/F] in the bipolar cell evoked by the stimulation in the preferred and null directions. The preferred and null directions referred to the preferred and null directions of the connected ON DS cell, respectively. Since iGluSnFR signals did not show direction selectivity, we performed the following analysis. For each dendritic segment we calculated the vector sum of the normalized iGluSnFR responses ([ΔF/F]/mean[ΔF/F]). We called these vectors “Dendrite Response Vectors” (DRV). For each ganglion cell we formed the mean vector of all DRVs. This vector is called “Cell Response Vector” (CRV). We then determined the magnitude of CRV for each cell. In Figure 4L we compare the magnitude of CRVs of iGluSnFR responses with the magnitude of CRVs of GCaMP3 responses (calculated in a similar to the CRVs of iGluSnFR responses). The rational of this comparison is that if all dendrites of a given ganglion cell have the largest responses to the same motion direction and all show strong direction selectivity, the magnitude of CRV is large, if the different dendrites have largest responses to different directions and their direction selectivity is low the magnitude of CRV is low.

Immunohistochemistry. After the experiments, retinas were fixed for 30 min in 4% (wt/vol) paraformaldehyde in PBS (137 mM NaCl, 2.7 mM KCl, 4.3 mM Na2HPO4, 1.47 mM KH2PO4, pH 7.4) and washed with PBS for at least 1 day at 4°C. To aid penetration of the antibodies, retinas were frozen and thawed three times after cryoprotection with 30% (wt/vol) sucrose. All other procedures were carried out at room temperature, except for the secondary antibody reaction. After washing in PBS, retinas were blocked for 1 h in 10% (vol/vol) normal donkey serum (NDS; Chemicon), 1% (wt/vol) bovine serum albumin (BSA), and 0.5% (vol/vol) TritonX-100 in PBS.

Primary antibodies were incubated for 6-7 days in 3% (vol/vol) NDS, 1% (wt/vol) BSA, 0.02% (wt/vol) sodium azide, and 0.5% (vol/vol) TritonX-100 in PBS. Secondary antibodies were incubated for one day at 4°C in 3% (vol/vol) NDS, 1% (wt/vol) BSA, and 0.5% (vol/vol) TritonX-100 in PBS together with DAPI (4',6-diamidine-2-phenylindole dihydrochloride, Roche Diagnostics, 10 µg/ml). DAPI binds to DNA and, therefore, labels nuclei. After a final wash in PBS, retinas were embedded in Prolong Gold antifade (Molecular Probes). The following sets of primary and secondary antibody combinations were used for staining rabies virus-infected retinas: (i) Primary: goat anti-ChAT (1:200, AB144P, Chemicon). Secondary: donkey anti-goat IgG conjugated with Alexa Fluor 568 (1:200, Invitrogen). (ii) Primary: rabbit anti-GFP in order to label GCaMP3 and iGluSnFR (1:200, A11122, Invitrogen). Secondary: donkey anti-rabbit IgG conjugated with Alexa Fluor 488 (1:200, Invitrogen).

Confocal analysis. Stained retinas were analyzed using a Zeiss LSM 700 confocal microscope. Morphologies of the GCaMP3-labeled circuits containing ON DS cells, bipolar cells, and starburst cells were assessed from tiling (up to 3×3 tiling) of 1024×1024 pixel images in a zstack with 0.30 µm z-steps using a 63× oil-immersion lens, NA 1.3. The tiling image was stitched using ZEN software (Zeiss). Morphologies of the iGluSnFR-labeled ON DS cells were assessed from 1024×1024 pixel images in a z-stack with 0.30 µm z-steps using a 40× oil immersion lens, NA 1.2. Images were processed using Imaris (Bitplane) or Fiji.

Statistical analysis. The Kruskal-Wallis one-way analysis was used to determine if any one of the responses to all eight directions was different from the mean response (Figure 3J, 4G). The non-parametric Mann-Whitney U test was used to compare data on Figure 3E, 3G and 4L. The Hodges-Ajne test was performed to determine if the directions of the vector sum of bipolar cell terminal activities were drawn from a uniform distribution ($p < 0.05$ rejects this hypothesis, Figure 3I). Significance is denoted by * for $P < 0.05$, ** for $P < 0.01$, and *** for $P < 0.001$. Not significant was denoted as n.s. for $P > 0.05$. The error bars and ± values represent standard deviations (s.d.)

Animals. Wild-type (C57BL/6) and Rd1 (CH3) mice purchased from Charles River were used for viral tracing experiments. Opn4-GFP mice were purchased from Gensat. Sox14-Cre mice were obtained from Alessio Delogu. All animal procedures were performed in accordance with standard ethical guidelines (European Communities Guidelines on the Care and Use of Laboratory Animals, 86/609/EEC) and were approved by the Veterinary Department of the Canton of Basel-Stadt, Switzerland.

Viruses. AAV viruses expressing the GCaMP6s and NLS-tdTomato were produced as described earlier(*19*). EnvA coated SADΔG-GFP rabies virus has been amplified, and concentrated by ultracentrifugation, as described previously(*12*). Viruses were injected by using using a microinjector (Narishige, IM- 11-2) combined with a stereotaxic instrument (Narishige, SR-5M). Virus injection for viral tracing were performed under isoflurane anesthesia, while AAV injections for in vitro imaging were performed during the preparation of chronic window preparation. Mice were anesthetized with fentanyl-medetomidine-midazolam (fentanyl 0.05 mg/kg, medetomidine 0.5 mg/kg, midazolam 5.0 mg/kg). Colliquifilm was applied to the eyes to prevent dehydration during surgery. A thin iron ring and a metal bar were attached to the skull with a mixture of dental cement and Super Glue to allow for subsequent head fixation during calcium imaging. A 3 mm-diameter craniotomy was made above primary visual cortex in the left hemisphere. After removal of the 3 mm diameter skull flap, the cortical surface was kept moist with a cortex buffer, containing: 135 mM NaCl, 5 mM KCl, 10 mM glucose, 10 mM HEPES, 2 mM $MgSO_4$ and 2 mM $CaCl_2$. After single cell electroporation (see below), the exposed cortex was covered with a 3 mm diameter glass coverslip and sealed with Super Glue.

In vivo calcium imaging. During imaging, mice were anesthetized with 0.25% isoflurane and sedated with 2.5 mg/kg chlorprothixene. To shield the objective from the light of the visual stimulation, a metal cone with a magnetic base was placed onto the iron ring attached to the head of the mouse and the gap between the metal cone and the iron ring was filled with 1% low-melting-point agarose mixed with black pigment. Next, the location of GCaMP6s expressing cell

bodies were detected in the reference z-stack by the imaging software. Finally, the detected cells were imaged at 20-100Hz depending on the number of detected cells, using random-access 3D point scanning. Visual stimulation was controlled using Python based software and was performed with a blue LED lamp placed directly front of the eye of the mouse. Five second light pulses were applied in every 30 seconds and it was repeated 10-30 times. Data analisis was performed by Matlab.

Retinal electrophysiology and light stimulation. The retina was isolated and perfused as described above. Virus- labeled ganglion cells were visualized by two-photon imaging and targeted by glass electrodes under the guidance of an infrared camera. The resistance of the electrodes was 7 -9 MΩ and the electrodes were filled with (in mM): 115 KGluconate, 9.7 KCl,1 Mg Cl2, 0.5 CaCl2, 1.5 EGTA, 10 HEPES, 4 ATP-Na2, 0.5 GTP-Na3 (pH 7.2). Multiclamp 700B patch clamp amplifier (Axon Instruments) was used to stimulate cells. The visual stimulation and data acquisition software was written in LabView (National Instruments) by David Balya and Thomas Münch. Data were analyzed in Matlab. Visual stimuli were applied using a digital light processor (DLP) projector through the lamp port of an Olympus BX51 upright microscope. The image was focused on the photoreceptors through the condenser before the experiment. In pharmacological experiments, agents were bath-applied at the following concentrations: 10 µM CPP ((±)-3-(2-carboxypiperazin-4-yl) propyl-1-phosphonic acid, blocking NMDA receptors), 10 µM NBQX (6-nitro-2,3-dioxo-1,4-dihydrobenzo[f]quinoxaline-7-sulfonamide, blocking AMPA and kainate receptors), 10 µM APB (L-(+)-2-amino-4-phosphonobutyric acid, blocking metabotropic glutamate receptors and therefore blocking the ON pathway), 50 µM cobalt-2-cloride (blocking calcium mediated mechanisms.) All chemicals were obtained from Sigma, with the exception of APB (Calbiochem).

Immunohistochemistry. The retina was fixed in 4% paraformaldehyde (PFA) in phosphate buffered saline (PBS) at pH 7.4 for 30 minutes at room temperature (RT) and washed in 50 ml PBS for 1-5 days at 4 ºC. Brains were fixed in 4% PFA in PBS for 2 hours and incubated in 200 ml PBS overnight at RT. The brain was embedded in 2% agar in PBS and vibratome sectioned to 100-µm thick sections. The antibody staining procedure for both the retina and the vibratome sections were the same and were carried out at RT. The tissue was blocked for 1 hour in 10%

Normal Donkey Serum (NDS), 1% Bovine Serum Albumin (BSA) and 0.5% Triton X100 in PBS (pH 7.4) followed by incubation with the primary antibodies in 3% NGS (or NDS), 1% BSA, 0.5% Triton X100 in PBS for 3 days. After three rounds of 10-20 minute washes in PBS, the secondary antibodies were applied for two hours in 2-10 µm/ml DAPI, 3% NGS (or NDS), 1% BSA, 0.5% Triton X100 in PBS. For GFP immunohistochemistry after secondary antibody incubation, the tissue was washed three times in PBS as before and incubated overnight with streptavidin conjugated to Alexa 488 (Invitrogen) in 0.5 % Triton X100 in PBS. At the end of the staining procedure the tissue was washed three times in PBS and mounted with ProLong antifade mounting medium (Invitrogen). The following primary antibodies were used: rabbit anti-GFP (1:200 or 1:500, Invitrogen), sheep anti-GFP (1;200, Biogenesis), rabbit anti-melanopsin (1:5000, kind gift from I. Provencio, Uniform Services University, Bethesda, MD), goat anti-ChAT (1:200, Invitrogen). Secondary antibodies were conjugated with Biotin (for GFP staining), Alexa 488 or Alexa 555 (Invitrogen).

Confocal microscopy and analysis. The 405, 488, 555 and 633 nm laser lines of a Zeiss LSM 700 Meta confocal microscope were used to excite DAPI, Alexa 488, Alexa 555 and Alexa 633 respectively. A 63X, 1.4 numerical aperture oil immersion Objective (Zeiss) was used. The z steps were 0.2-0.35 microns. The scan started at the ganglion cell layer and continued until the photoreceptor layer. The acquired images were analyzed and processed in ImageJ.

Acknowledgment

I would like to thank for my thesis advisor Botond Roska to guide me during my work, to all my colleagues in the Roska group, at the FMI and at the University of Basel who provided help or advice for my research. I thank to my external collaborators Zsolt Boldogkoi and Alessio Delogu for their cooperation. I would like to thank the comments from my thesis committee members Silvia Arber and Karl-Klaus Conzelmann. I thank to the Novartis Research Foundation and to the European Research Council (ERC) for the financing. Finally I thank to my family especially my wife to support me during these years of research.

References

1. F. A. C. Azevedo *et al.*, Equal numbers of neuronal and nonneuronal cells make the human brain an isometrically scaled-up primate brain. *J. Comp. Neurol.* **513**, 532–541 (2009).

2. S. N. Tuncdemir, G. Fishell, Neural circuits look forward. *Proc. Natl. Acad. Sci. U. S. A.* **108**, 16137–16138 (2011).

3. J. J. Nassi, C. L. Cepko, R. T. Born, K. T. Beier, Neuroanatomy goes viral! *Front. Neuroanat.* **9** (2015), doi:10.3389/fnana.2015.00080.

4. C. Grienberger, A. Konnerth, Imaging Calcium in Neurons. *Neuron*. **73**, 862–885 (2012).

5. K. Kristensson, Y. Olsson, Retrograde axonal transport of protein. *Brain Res.* **29**, 363–365 (1971).

6. L. C. Schmued, J. H. Fallon, Fluoro-Gold: a new fluorescent retrograde axonal tracer with numerous unique properties. *Brain Res.* **377**, 147–154 (1986).

7. M. E. Schwab, F. Javoy-Agid, Y. Agid, Labeled wheat germ agglutinin (WGA) as a new, highly sensitive retrograde tracer in the rat brain hippocampal system. *Brain Res.* **152**, 145–150 (1978).

8. C. R. Gerfen, P. E. Sawchenko, An anterograde neuroanatomical tracing method that shows the detailed morphology of neurons, their axons and terminals: immunohistochemical localization of an axonally transported plant lectin, Phaseolus vulgaris leucoagglutinin (PHA-L). *Brain Res.* **290**, 219–238 (1984).

9. J. C. Glover, G. Petursdottir, J. K. Jansen, Fluorescent dextran-amines used as axonal tracers in the nervous system of the chicken embryo. *J. Neurosci. Methods*. **18**, 243–254 (1986).

10. L. C. Katz, A. Burkhalter, W. J. Dreyer, Fluorescent latex microspheres as a retrograde neuronal marker for in vivo and in vitro studies of visual cortex. *Nature*. **310**, 498–500 (1984).

11. G. Ugolini, in *Advances in Virus Research* (Elsevier, 2011; http://linkinghub.elsevier.com/retrieve/pii/B978012387040700010X), vol. 79, pp. 165–202.

12. I. R. Wickersham *et al.*, Monosynaptic Restriction of Transsynaptic Tracing from Single, Genetically Targeted Neurons. *Neuron*. **53**, 639–647 (2007).

13. I. R. Wickersham, S. Finke, K.-K. Conzelmann, E. M. Callaway, Retrograde neuronal tracing with a deletion-mutant rabies virus. *Nat. Methods*. **4**, 47–49 (2007).

14. Z. Boldogköi, F. Erdélyi, A. Sik, T. F. Freund, I. Fodor, Construction of a recombinant herpesvirus expressing the jellyfish green fluorescent protein. *Lumin. J. Biol. Chem. Lumin.* **14**, 69–74 (1999).

15. Z. Boldogkői *et al.*, Genetically timed, activity-sensor and rainbow transsynaptic viral tools. *Nat. Methods*. **6**, 127 (2009).

16. T. J. Viney *et al.*, Local Retinal Circuits of Melanopsin-Containing Ganglion Cells Identified by Transsynaptic Viral Tracing. *Curr. Biol.* **17**, 981–988 (2007).

17. G. E. Pickard *et al.*, Intravitreal injection of the attenuated pseudorabies virus PRV Bartha results in infection of the hamster suprachiasmatic nucleus only by retrograde transsynaptic transport via autonomic circuits. *J. Neurosci. Off. J. Soc. Neurosci.* **22**, 2701–2710 (2002).

18. Y. Sun *et al.*, Cell-type-specific circuit connectivity of hippocampal CA1 revealed through Cre-dependent rabies tracing. *Cell Rep.* **7**, 269–280 (2014).

19. A. Wertz *et al.*, PRESYNAPTIC NETWORKS. Single-cell-initiated monosynaptic tracing reveals layer-specific cortical network modules. *Science*. **349**, 70–74 (2015).

20. K. Yonehara *et al.*, The first stage of cardinal direction selectivity is localized to the dendrites of retinal ganglion cells. *Neuron*. **79**, 1078–1085 (2013).

21. B. N. Smith *et al.*, Pseudorabies virus expressing enhanced green fluorescent protein: A tool for in vitro electrophysiological analysis of transsynaptically labeled neurons in identified central nervous system circuits. *Proc. Natl. Acad. Sci.* **97**, 9264–9269 (2000).

22. J. DeFalco, Virus-Assisted Mapping of Neural Inputs to a Feeding Center in the Hypothalamus. *Science*. **291**, 2608–2613 (2001).

23. P. J. Sollars *et al.*, Melanopsin and non-melanopsin expressing retinal ganglion cells innervate the hypothalamic suprachiasmatic nucleus. *Vis. Neurosci.* **20**, 601–610 (2003).

24. B. W. Banfield, J. D. Kaufman, J. A. Randall, G. E. Pickard, Development of pseudorabies virus strains expressing red fluorescent proteins: new tools for multisynaptic labeling applications. *J. Virol.* **77**, 10106–10112 (2003).

25. A. D. Loewy, Viruses as Transneuronal Tracers for Defining Neural Circuits. *Neurosci. Biobehav. Rev.* **22**, 679–684 (1998).

26. A. M. Strack, A. D. Loewy, Pseudorabies virus: a highly specific transneuronal cell body marker in the sympathetic nervous system. *J. Neurosci. Off. J. Soc. Neurosci.* **10**, 2139–2147 (1990).

27. B. Lomniczi, A. S. Kaplan, T. Ben-Porat, Multiple defects in the genome of pseudorabies virus can affect virulence without detectably affecting replication in cell culture. *Virology*. **161**, 181–189 (1987).

28. M. J. Schnell, J. P. McGettigan, C. Wirblich, A. Papaneri, The cell biology of rabies virus: using stealth to reach the brain. *Nat. Rev. Microbiol.* **8**, 51–61 (2010).

29. B. Roska, Vertical interactions across ten parallel, stacked representations in the mammalian retina. *Nature*. **410**, 583–587 (2001).

30. C. J. Jeon, E. Strettoi, R. H. Masland, The major cell populations of the mouse retina. *J. Neurosci. Off. J. Soc. Neurosci.* **18**, 8936–8946 (1998).

31. J. R. Sanes, R. H. Masland, The Types of Retinal Ganglion Cells: Current Status and Implications for Neuronal Classification. *Annu. Rev. Neurosci.* **38**, 221–246 (2015).

32. R. H. MASLAND, The tasks of amacrine cells. *Vis. Neurosci.* **29**, 3–9 (2012).

33. R. H. Masland, The fundamental plan of the retina. *Nat. Neurosci.* **4**, 877–886 (2001).

34. M. T. Perenin, M. Jeannerod, Subcortical vision in man. *Trends Neurosci.* **2**, 204–207 (1979).

35. A. D. Güler *et al.*, Melanopsin cells are the principal conduits for rod-cone input to non-image-forming vision. *Nature*. **453**, 102–105 (2008).

36. D. I. Vaney, W. R. Taylor, Direction selectivity in the retina. *Curr. Opin. Neurobiol.* **12**, 405–410 (2002).

37. C. W. Oyster, Direction-selective retinal ganglion cells and control of optokinetic nystagmus in the rabbit. *Vis. Res*. **12**, 183–193 (1972).

38. S. Hattar, Melanopsin-containing retinal ganglion cells: architecture, projections, and intrinsic photosensitivity. *Science*. **295**, 1065–1070 (2002).

39. J. L. Ecker *et al.*, Melanopsin-Expressing Retinal Ganglion-Cell Photoreceptors: Cellular Diversity and Role in Pattern Vision. *Neuron*. **67**, 49–60 (2010).

40. X. Zhao, B. K. Stafford, A. L. Godin, W. M. King, K. Y. Wong, Photoresponse diversity among the five types of intrinsically photosensitive retinal ganglion cells. *J. Physiol.* **592**, 1619–1636 (2014).

41. C. A. Procyk *et al.*, Spatial receptive fields in the retina and dorsal lateral geniculate nucleus (dLGN) of mice lacking rods and cones. *J. Neurophysiol.*, jn.00368.2015 (2015).

42. W. Sun, ON direction-selective ganglion cells in the mouse retina. *J Physiol Lond*. **576**, 197–202 (2006).

43. I.-J. Kim, Y. Zhang, M. Yamagata, M. Meister, J. R. Sanes, Molecular identification of a retinal cell type that responds to upward motion. *Nature*. **452**, 478–482 (2008).

44. S. Weng, W. Sun, S. He, Identification of ON-OFF direction-selective ganglion cells in the mouse retina: ON-OFF DSGCs in the mouse retina. *J. Physiol.* **562**, 915–923 (2005).

45. D. I. Vaney, Direction selectivity in the retina. *Curr Opin Neurobiol*. **12**, 405–410 (2002).

46. I. R. Wickersham, Monosynaptic restriction of transsynaptic tracing from single, genetically targeted neurons. *Neuron*. **53**, 639–647 (2007).

47. B. N. Smith *et al.*, Pseudorabies virus expressing enhanced green fluorescent protein: A tool for in vitro electrophysiological analysis of transsynaptically labeled neurons in identified central nervous system circuits. *Proc. Natl. Acad. Sci. U. S. A.* **97**, 9264–9269 (2000).

48. A. Jöns, T. C. Mettenleiter, Green fluorescent protein expressed by recombinant pseudorabies virus as an in vivo marker for viral replication. *J. Virol. Methods*. **66**, 283–292 (1997).

49. N. Heim, O. Griesbeck, Genetically Encoded Indicators of Cellular Calcium Dynamics Based on Troponin C and Green Fluorescent Protein. *J. Biol. Chem.* **279**, 14280–14286 (2004).

50. A. S. Kaplan, A. E. Vatter, A comparison of herpes simplex and pseudorabies viruses. *Virology*. **7**, 394–407 (1959).

51. P. J. Husak, T. Kuo, L. W. Enquist, Pseudorabies Virus Membrane Proteins gI and gE Facilitate Anterograde Spread of Infection in Projection- Specific Neurons in the Rat. *J. Virol.* **74**, 10975–10983 (2000).

52. V. De Paola, S. Arber, P. Caroni, AMPA receptors regulate dynamic equilibrium of presynaptic terminals in mature hippocampal networks. *Nat. Neurosci.* **6**, 491–500 (2003).

53. S. Hattar *et al.*, Central projections of melanopsin-expressing retinal ganglion cells in the mouse. *J. Comp. Neurol.* **497**, 326–349 (2006).

54. I. Provencio, M. D. Rollag, A. M. Castrucci, Photoreceptive net in the mammalian retina. This mesh of cells may explain how some blind mice can still tell day from night. *Nature*. **415**, 493 (2002).

55. S. B. Baver, G. E. Pickard, P. J. Sollars, G. E. Pickard, Two types of melanopsin retinal ganglion cell differentially innervate the hypothalamic suprachiasmatic nucleus and the olivary pretectal nucleus. *Eur. J. Neurosci.* **27**, 1763–1770 (2008).

56. B. W. Banfield, J. D. Kaufman, J. A. Randall, G. E. Pickard, Development of Pseudorabies Virus Strains Expressing Red Fluorescent Proteins: New Tools for Multisynaptic Labeling Applications. *J. Virol.* **77**, 10106–10112 (2003).

57. M. C. Zemanick, P. L. Strick, R. D. Dix, Direction of transneuronal transport of herpes simplex virus 1 in the primate motor system is strain-dependent. *Proc. Natl. Acad. Sci. U. S. A.* **88**, 8048–8051 (1991).

58. M. Mank *et al.*, A genetically encoded calcium indicator for chronic in vivo two-photon imaging. *Nat. Methods*. **5**, 805–811 (2008).

59. L. E. Pomeranz, A. E. Reynolds, C. J. Hengartner, Molecular biology of pseudorabies virus: impact on neurovirology and veterinary medicine. *Microbiol. Mol. Biol. Rev. MMBR*. **69**, 462–500 (2005).

60. Y. Fu, H.-W. Liao, M. T. H. Do, K.-W. Yau, Non-image-forming ocular photoreception in vertebrates. *Curr. Opin. Neurobiol.* **15**, 415–422 (2005).

61. M. A. Belenky, C. A. Smeraski, I. Provencio, P. J. Sollars, G. E. Pickard, Melanopsin retinal ganglion cells receive bipolar and amacrine cell synapses. *J. Comp. Neurol.* **460**, 380–393 (2003).

62. J. P. Card, M. E. Whealy, A. K. Robbins, R. Y. Moore, L. W. Enquist, Two α-herpesvirus strains are transported differentially in the rodent visual system. *Neuron*. **6**, 957–969 (1991).

63. J. DeFalco *et al.*, Virus-assisted mapping of neural inputs to a feeding center in the hypothalamus. *Science*. **291**, 2608–2613 (2001).

64. L. E. Pomeranz, A. E. Reynolds, C. J. Hengartner, Molecular Biology of Pseudorabies Virus: Impact on Neurovirology and Veterinary Medicine. *Microbiol. Mol. Biol. Rev.* **69**, 462–500 (2005).

65. H. Yoon, L. W. Enquist, C. Dulac, Olfactory Inputs to Hypothalamic Neurons Controlling Reproduction and Fertility. *Cell*. **123**, 669–682 (2005).

66. J. Hannibal, P. Hindersson, S. M. Knudsen, B. Georg, J. Fahrenkrug, The photopigment melanopsin is exclusively present in pituitary adenylate cyclase-activating polypeptide-containing retinal ganglion cells of the retinohypothalamic tract. *J. Neurosci. Off. J. Soc. Neurosci.* **22**, RC191 (2002).

67. S. Sekaran, R. G. Foster, R. J. Lucas, M. W. Hankins, Calcium Imaging Reveals a Network of Intrinsically Light-Sensitive Inner-Retinal Neurons. *Curr. Biol.* **13**, 1290–1298 (2003).

68. D. M. Dacey, *Ciba Found. Symp.*, in press.

69. K. K. Ghosh, S. Bujan, S. Haverkamp, A. Feigenspan, H. W�ssle, Types of bipolar cells in the mouse retina. *J. Comp. Neurol.* **469**, 70–82 (2004).

70. V. P. Connaughton, D. Graham, R. Nelson, Identification and morphological classification of horizontal, bipolar, and amacrine cells within the zebrafish retina. *J. Comp. Neurol.* **477**, 371–385 (2004).

71. S. Siegert *et al.*, Genetic address book for retinal cell types. *Nat. Neurosci.* **12**, 1197–1204 (2009).

72. S. Gustincich, A. Feigenspan, D. K. Wu, L. J. Koopman, E. Raviola, Control of Dopamine Release in the Retina: a Transgenic Approach to Neural Networks. *Neuron*. **18**, 723–736 (1997).

73. E. M. Lasater, J. E. Dowling, Dopamine decreases conductance of the electrical junctions between cultured retinal horizontal cells. *Proc. Natl. Acad. Sci. U. S. A.* **82**, 3025–3029 (1985).

74. P. Witkovsky, Dopamine and retinal function. *Doc. Ophthalmol.* **108**, 17–39 (2004).

75. K. Sakamoto, Classical Photoreceptors Regulate Melanopsin mRNA Levels in the Rat Retina. *J. Neurosci.* **24**, 9693–9697 (2004).

76. K. Sakamoto *et al.*, Dopamine regulates melanopsin mRNA expression in intrinsically photosensitive retinal ganglion cells. *Eur. J. Neurosci.* **22**, 3129–3136 (2005).

77. B. M. Steenhard, J. C. Besharse, Phase shifting the retinal circadian clock: xPer2 mRNA induction by light and dopamine. *J. Neurosci. Off. J. Soc. Neurosci.* **20**, 8572–8577 (2000).

78. D. H. Hubel, T. N. Wiesel, Receptive fields, binocular interaction and functional architecture in the cat's visual cortex. *J. Physiol.* **160**, 106–154.2 (1962).

79. H. B. Barlow, R. M. Hill, Selective sensitivity to direction of movement in ganglion cells of the rabbit retina. *Science*. **139**, 412–414 (1963).

80. S. I. Fried, T. A. Mu¨nch, F. S. Werblin, Directional Selectivity Is Formed at Multiple Levels by Laterally Offset Inhibition in the Rabbit Retina. *Neuron*. **46**, 117–127 (2005).

81. T. Euler, Directionally selective calcium signals in dendrites of starburst amacrine cells. *Nature*. **418**, 845–852 (2002).

82. S. Lee, The synaptic mechanism of direction selectivity in distal processes of starburst amacrine cells. *Neuron*. **51**, 787–799 (2006).

83. C. Bamann, Structural guidance of the photocycle of channelrhodopsin-2 by an interhelical hydrogen bond. *Biochemistry (Mosc.)*. **49**, 267–278 (2010).

84. K. Yonehara, Expression of SPIG1 reveals development of a retinal ganglion cell subtype projecting to the medial terminal nucleus in the mouse. *PLoS ONE*. **3**, e1533 (2008).

85. H. B. Barlow, R. Fitzhugh, S. W. Kuffler, Change of organization in the receptive fields of the cat's retina during dark adaptation. *J. Physiol.* **137**, 338–354 (1957).

86. J. B. Demb, Cellular mechanisms for direction selectivity in the retina. *Neuron*. **55**, 179–186 (2007).

87. S. I. Fried, T. A. Münch, F. S. Werblin, Mechanisms and circuitry underlying directional selectivity in the retina. *Nature*. **420**, 411–414 (2002).

88. M. Ariel, N. W. Daw, Pharmacological analysis of directionally sensitive rabbit retinal ganglion cells. *J. Physiol.* **324**, 161–185 (1982).

89. S. I. Fried, Directional selectivity is formed at multiple levels by laterally offset inhibition in the rabbit retina. *Neuron*. **46**, 117–127 (2005).

90. K. Yonehara, Identification of retinal ganglion cells and their projections involved in central transmission of information about upward and downward image motion. *PLoS ONE*. **4**, e4320 (2009).

91. M. Chen, Physiological properties of direction-selective ganglion cells in early postnatal and adult mouse retina. *J Physiol Lond*. **587**, 819–828 (2009).

92. C. W. Oyster, E. Takahashi, H. Collewijn, Direction-selective retinal ganglion cells and control of optokinetic nystagmus in the rabbit. *Vision Res.* **12**, 183–193 (1972).

93. J. I. Simpson, The accessory optic system. *Annu Rev Neurosci*. **7**, 13–41 (1984).

94. I. Radu *et al.*, Conformational changes of channelrhodopsin-2. *J. Am. Chem. Soc.* **131**, 7313–7319 (2009).

95. W. Wei, A. M. Hamby, K. Zhou, M. B. Feller, Development of asymmetric inhibition underlying direction selectivity in the retina. *Nature*. **469**, 402–406 (2011).

96. A. Borst, Direction selectivity in ganglion cells: pre or post? *Nat. Neurosci.* **4**, 119–120 (2001).

97. W. R. Taylor, Dendritic Computation of Direction Selectivity by Retinal Ganglion Cells. *Science*. **289**, 2347–2350 (2000).

98. L. J. Borg-Graham, The computation of directional selectivity in the retina occurs presynaptic to the ganglion cell. *Nat. Neurosci.* **4**, 176–183 (2001).

99. K. Yoshida *et al.*, A Key Role of Starburst Amacrine Cells in Originating Retinal Directional Selectivity and Optokinetic Eye Movement. *Neuron*. **30**, 771–780 (2001).

100. S. E. Hausselt, T. Euler, P. B. Detwiler, W. Denk, A Dendrite-Autonomous Mechanism for Direction Selectivity in Retinal Starburst Amacrine Cells. *PLoS Biol.* **5**, e185 (2007).

101. W. Wei, M. B. Feller, Organization and development of direction-selective circuits in the retina. *Trends Neurosci.* **34**, 638–645 (2011).

102. K. L. Briggman, M. Helmstaedter, W. Denk, Wiring specificity in the direction-selectivity circuit of the retina. *Nature*. **471**, 183–188 (2011).

103. S. Lee, K. Kim, Z. J. Zhou, Role of ACh-GABA Cotransmission in Detecting Image Motion and Motion Direction. *Neuron*. **68**, 1159–1172 (2010).

104. K. Yonehara *et al.*, Spatially asymmetric reorganization of inhibition establishes a motion-sensitive circuit. *Nature*. **469**, 407–410 (2011).

105. N. Oesch, T. Euler, W. R. Taylor, Direction-Selective Dendritic Action Potentials in Rabbit Retina. *Neuron*. **47**, 739–750 (2005).

106. A. Poleg-Polsky, J. S. Diamond, Imperfect space clamp permits electrotonic interactions between inhibitory and excitatory synaptic conductances, distorting voltage clamp recordings. *PloS One*. **6**, e19463 (2011).

107. D. I. Vaney, B. Sivyer, W. R. Taylor, Direction selectivity in the retina: symmetry and asymmetry in structure and function. *Nat. Rev. Neurosci.* (2012), doi:10.1038/nrn3165.

108. H. Asari, M. Meister, Divergence of visual channels in the inner retina. *Nat. Neurosci.* **15**, 1581–1589 (2012).

109. E. M. Callaway, Transneuronal circuit tracing with neurotropic viruses. *Curr. Opin. Neurobiol.* **18**, 617–623 (2008).

110. F. Osakada *et al.*, New Rabies Virus Variants for Monitoring and Manipulating Activity and Gene Expression in Defined Neural Circuits. *Neuron*. **71**, 617–631 (2011).

111. L. Tian *et al.*, Imaging neural activity in worms, flies and mice with improved GCaMP calcium indicators. *Nat. Methods*. **6**, 875–881 (2009).

112. D. F. Reiff, J. Plett, M. Mank, O. Griesbeck, A. Borst, Visualizing retinotopic half-wave rectified input to the motion detection circuitry of Drosophila. *Nat. Neurosci.* **13**, 973–978 (2010).

113. T. Euler, P. B. Detwiler, W. Denk, Directionally selective calcium signals in dendrites of starburst amacrine cells. *Nature*. **418**, 845–852 (2002).

114. J. S. Marvin *et al.*, An optimized fluorescent probe for visualizing glutamate neurotransmission. *Nat. Methods*. **10**, 162–170 (2013).

115. K. Yonehara *et al.*, Spatially asymmetric reorganization of inhibition establishes a motion-sensitive circuit. *Nature*. **469**, 407–410 (2011).

116. B. G. Borghuis, J. S. Marvin, L. L. Looger, J. B. Demb, Two-Photon Imaging of Nonlinear Glutamate Release Dynamics at Bipolar Cell Synapses in the Mouse Retina. *J. Neurosci.* **33**, 10972–10985 (2013).

117. H. B. Barlow, Selective sensitivity to direction of movement in ganglion cells of the rabbit retina. *Science*. **139**, 412–414 (1963).

118. M. J. Schachter, N. Oesch, R. G. Smith, W. R. Taylor, Dendritic spikes amplify the synaptic signal to enhance detection of motion in a simulation of the direction-selective ganglion cell. *PLoS Comput. Biol.* **6** (2010), doi:10.1371/journal.pcbi.1000899.

119. S. Trenholm, K. Johnson, X. Li, R. G. Smith, G. B. Awatramani, Parallel Mechanisms Encode Direction in the Retina. *Neuron*. **71**, 683–694 (2011).

120. S. He, R. H. Masland, ON direction-selective ganglion cells in the rabbit retina: Dendritic morphology and pattern of fasciculation. *Vis. Neurosci.* **15**, 369–375 (1998).

121. S. Chen, J. S. Diamond, Synaptically released glutamate activates extrasynaptic NMDA receptors on cells in the ganglion cell layer of rat retina. *J. Neurosci. Off. J. Soc. Neurosci.* **22**, 2165–2173 (2002).

122. B. T. Sagdullaev, M. A. McCall, P. D. Lukasiewicz, Presynaptic Inhibition Modulates Spillover, Creating Distinct Dynamic Response Ranges of Sensory Output. *Neuron*. **50**, 923–935 (2006).

123. B. Sivyer, D. I. Vaney, Dendritic morphology and tracer-coupling pattern of physiologically identified transient uniformity detector ganglion cells in rabbit retina. *Vis. Neurosci.* **27**, 159–170 (2010).

124. Z. Shi *et al.*, Vsx1 Regulates Terminal Differentiation of Type 7 ON Bipolar Cells. *J. Neurosci.* **31**, 13118–13127 (2011).

125. C.-C. Chiao, R. H. Masland, Contextual tuning of direction-selective retinal ganglion cells. *Nat. Neurosci.* **6**, 1251–1252 (2003).

126. L. L. Wright *et al.*, The DAPI-3 amacrine cells of the rabbit retina. *Vis. Neurosci.* **14**, 473–492 (1997).

127. A. Borst, T. Euler, Seeing Things in Motion: Models, Circuits, and Mechanisms. *Neuron*. **71**, 974–994 (2011).

128. M. Hatori *et al.*, Inducible ablation of melanopsin-expressing retinal ganglion cells reveals their central role in non-image forming visual responses. *PloS One*. **3**, e2451 (2008).

129. S. Hattar, H. W. Liao, M. Takao, D. M. Berson, K. W. Yau, Melanopsin-containing retinal ganglion cells: architecture, projections, and intrinsic photosensitivity. *Science*. **295**, 1065–1070 (2002).

130. M. E. Estevez *et al.*, Form and Function of the M4 Cell, an Intrinsically Photosensitive Retinal Ganglion Cell Type Contributing to Geniculocortical Vision. *J. Neurosci.* **32**, 13608–13620 (2012).

131. T. M. Schmidt, S.-K. Chen, S. Hattar, Intrinsically photosensitive retinal ganglion cells: many subtypes, diverse functions. *Trends Neurosci.* **34**, 572–580 (2011).

132. E. D. Buhr, R. N. Van Gelder, Local photic entrainment of the retinal circadian oscillator in the absence of rods, cones, and melanopsin. *Proc. Natl. Acad. Sci. U. S. A.* **111**, 8625–8630 (2014).

133. S. Nirenberg, C. Pandarinath, Retinal prosthetic strategy with the capacity to restore normal vision. *Proc. Natl. Acad. Sci. U. S. A.* **109**, 15012–15017 (2012).

134. P. S. Lagali *et al.*, Light-activated channels targeted to ON bipolar cells restore visual function in retinal degeneration. *Nat. Neurosci.* **11**, 667–675 (2008).

135. K. Farrow *et al.*, Ambient Illumination Toggles a Neuronal Circuit Switch in the Retina and Visual Perception at Cone Threshold. *Neuron*. **78**, 325–338 (2013).

136. T. A. Münch *et al.*, Approach sensitivity in the retina processed by a multifunctional neural circuit. *Nat. Neurosci.* **12**, 1308–1316 (2009).

137. G. Katona *et al.*, Fast two-photon in vivo imaging with three-dimensional random-access scanning in large tissue volumes. *Nat. Methods*. **9**, 201–208 (2012).

138. M. Koyanagi, E. Takada, T. Nagata, H. Tsukamoto, A. Terakita, Homologs of vertebrate Opn3 potentially serve as a light sensor in nonphotoreceptive tissue. *Proc. Natl. Acad. Sci. U. S. A.* **110**, 4998–5003 (2013).

139. D. M. Berson, F. A. Dunn, M. Takao, Phototransduction by Retinal Ganglion Cells That Set the Circadian Clock. *Science*. **295**, 1070–1073 (2002).

140. M. Neitz, J. Neitz, The uncommon retina of the common house mouse. *Trends Neurosci.* **24**, 248–250 (2001).

141. A. Delogu *et al.*, Subcortical visual shell nuclei targeted by ipRGCs develop from a Sox14+-GABAergic progenitor and require Sox14 to regulate daily activity rhythms. *Neuron*. **75**, 648–662 (2012).

142. L. W. Enquist, P. J. Husak, B. W. Banfield, G. A. Smith, Infection and spread of alphaherpesviruses in the nervous system. *Adv. Virus Res.* **51**, 237–347 (1998).

143. A. D. Brideau, J. P. Card, L. W. Enquist, Role of pseudorabies virus Us9, a type II membrane protein, in infection of tissue culture cells and the rat nervous system. *J. Virol.* **74**, 834–845 (2000).

144. G. J. Wojaczynski, E. A. Engel, K. E. Steren, L. W. Enquist, J. Patrick Card, The neuroinvasive profiles of H129 (herpes simplex virus type 1) recombinants with putative anterograde-only transneuronal spread properties. *Brain Struct. Funct.* **220**, 1395–1420 (2015).

145. M. J. Van Hook, K. Y. Wong, D. M. Berson, Dopaminergic modulation of ganglion-cell photoreceptors in rat. *Eur. J. Neurosci.* **35**, 507–518 (2012).

146. S. Siegert *et al.*, Transcriptional code and disease map for adult retinal cell types. *Nat. Neurosci.* **15**, 487–495 (2012).

147. E. Papageorgiou, R. J. McLean, I. Gottlob, Nystagmus in childhood. *Pediatr. Neonatol.* **55**, 341–351 (2014).

148. Z. Boldogköi *et al.*, Construction of recombinant pseudorabies viruses optimized for labeling and neurochemical characterization of neural circuitry. *Mol. Brain Res.* **109**, 105–118 (2002).

149. G. Rabut, J. Ellenberg, Automatic real-time three-dimensional cell tracking by fluorescence microscopy. *J. Microsc.* **216**, 131–137 (2004).